



UNIVERSIDADE FEDERAL DO RIO GRANDE DO NORTE  
CENTRO DE CIÊNCIAS EXATAS E DA TERRA  
PROGRAMA DE PÓS-GRADUAÇÃO EM GEODINÂMICA E GEOFÍSICA

# **Otimização global para resolver problemas inversos em eletrorresistividade com flexibilidade na escolha dos vínculos**

**Francisco Márcio Barboza**

Orientador: Prof. Dr. Walter Eugênio de Medeiros

**Tese de Doutorado** apresentada ao Programa de Pós-Graduação em Geodinâmica e Geofísica da UFRN, como parte dos requisitos para obtenção do título de Doutor em Ciências.

Tese nº 50/ PPGG

Natal, RN, novembro de 2017

Universidade Federal do Rio Grande do Norte - UFRN  
Sistema de Bibliotecas - SISBI  
Catalogação de Publicação na Fonte. UFRN - Biblioteca Setorial Prof. Ronaldo Xavier de Arruda - CCET

Barboza, Francisco Márcio.

Otimização global para resolver problemas inversos em eletrorresistividade com flexibilidade na escolha dos vínculos / Francisco Márcio Barboza. - 2017.

152f.: il.

Tese (doutorado) - Universidade Federal do Rio Grande do Norte. Centro de Ciências Exatas e da Terra. Programa de Pós-Graduação em Geodinâmica e Geofísica. Natal, RN, 2017.

Orientador: Walter Eugênio de Medeiros.

1. Geofísica - Tese. 2. Otimização global - Tese. 3. Problemas inversos - Tese. 4. Eletrorresistividade - Tese. I. Medeiros, Walter Eugênio de. II. Título.

RN/UF/CCET

CDU 550.3

# **Otimização global para resolver problemas inversos em Eletroresistividade com flexibilidade na escolha dos vínculos**

**Francisco Márcio Barboza**

Tese de Doutorado aprovada em 28 de novembro de 2017 pela banca examinadora composta pelos seguintes membros:

---

Prof. Dr. Walter Eugênio de Medeiros (Orientador) ..... DGEF/UFRN

---

Prof. Dr. Aderson Farias do Nascimento ..... DGEF/UFRN

---

Prof. Dr. José Antônio de Moraes Moreira ..... DGEF/UFRN

---

Prof. Dr. Jessé Carvalho Costa ..... CPGf/ UFPA

---

Profª. Dra Valéria Cristina Ferreira Barbosa ..... ON/MCT

*À minha família, pela paciência  
durante a realização deste trabalho.*

---

# Agradecimentos

---

A Deus.

Ao meu orientador, professor Walter Medeiros, sou grato pela orientação, amizade e punções de orelha que sempre vi como conselhos de um pai (que nunca tive) para com seu filho.

Aos amigos do PPGG Renato Ramos e Jerbeson Santana pelas inúmeras ajudas, sugestões e discussões que sem elas nunca teria conseguido terminar este trabalho.

Aos demais colegas de pós-graduação, pelas amizades.

Aos funcionários do Departamento de Geofísica pelas amizades.

Aos membros da banca pelas sugestões de correções.

À minha família pelo apoio durante esta jornada.

À Universidade Federal do Acre pela liberação para cursar este doutorado.

Ao INCT-GP, pela compra de computadores de alta performance.

Ao CNPQ, pelo apoio financeiro.

---

# Resumo

---

Inversão em eletrorresistividade é um problema inverso mal posto, porque diferentes realizações de um mesmo modelo podem satisfazer aproximadamente o mesmo critério de ajuste. Se faz necessário portanto o uso de vínculos para obter soluções únicas e/ou estáveis à pequenas perturbações nas medidas. Contudo, em geral, a introdução de vínculos tem ficado restrita aos casos de vínculos diferenciáveis e que podem ser tratados com algoritmos de otimização local. A modelagem direta 1D e 2D em resistividade DC é computacionalmente barata, permitindo o uso de métodos de otimização global (GOMs) para resolver problemas inversos 1.5D e 2D com flexibilidade na incorporação de vínculos. As modificações da função de custo, seja na mudança de vínculos ou no critério de ajuste de dados, podem ser realizadas com facilidade, já que cada termo da função de custo é devidamente normalizado para permitir a invariância aproximada dos multiplicadores Lagrange. Os GOMs têm potencial para suportar um ambiente computacional adequado para interpretação quantitativa em que a comparação de soluções que incorporam diferentes restrições é uma maneira de inferir características da distribuição real da resistividade subterrânea. Neste trabalho foram desenvolvidas: (i) Comparação das performances dos métodos Simulated Annealing (SA), Algoritmo Genético (GA) e Particle Swarm Optimization (PSO) para resolver o problema inverso 1.5D na resistividade DC usando dados sintéticos e de campo; (ii) Apresentação de uma abordagem de inversão baseada no Particle Swarm Optimization (PSO) para os dados 2D de resistividade de corrente contínua (DC); (iii) Exploração de vários vínculos na variação de log da resistividade: continuidade espacial tanto nas normas  $L_1$  quanto  $L_2$ , incluindo o caso de restrição de variação apenas na direção horizontal, variação total e vínculos de esparsidade usando transformada discreta do cosseno e bases de Daubechies. Além disso, exploramos o vínculo de mínimo momento de inércia, incluindo o caso de usar a superfície da Terra como eixo alvo, para impor a concentração de materiais resistivos ou condutores ao longo dos eixos alvo. Os principais resultados da comparação para o case 1.5D são: a) todos os métodos reproduzem bastante a distribuição de resistividade de modelos sintéticos, b) PSO e GA são muito robustos para mudanças na função de custo e SA é comparativamente muito mais sensível, c) primeiro PSO e GA segundo apresentam o melhores desempenhos computacionais, exigindo um menor número de modelos de encaminhamento do que SA, e d) GA mostra o melhor desempenho em relação ao valor final alcançado da função de custo e seu desvio padrão, enquanto a SA tem o pior desempenho neste aspecto. Igualmente importante para ambos os casos 1.5D e 2D, a partir dos critérios de parada do algoritmo PSO resulta não apenas a melhor solução, mas também um conjunto de quase-soluções sub-ótimas a partir dos quais as análises de incerteza podem ser realizadas. Como resultado, o intérprete tem liberdade para realizar um processo de interpretação quantitativa

com base em uma abordagem de inversão de julgamento e erro, de forma semelhante, ele tem ao usar um software de modelagem avançado amigável, sendo capaz de conduzir a solução para incorporar suas concepções sobre o ambiente geológico, além de avaliar o ajuste de dados e a estabilidade das soluções obtidas. Apresentamos exemplos de dados sintéticos e de campo para ambos os casos de inversão.

**Palavras-chave:** Otimização global, Algoritmo genético, Eletroresistividade, Problemas inversos.

---

# Abstract

---

Inversion in DC-resistivity is an ill-posed inverse problem because different realizations of the same model might satisfy approximately the same data fitting criterium. It is therefore necessary to use constraints to obtain unique and / or stable solutions to small perturbations in the measurements. However, in general, the introduction of constraints has been restricted to cases of differentiable constraints, which can be treated with local optimization algorithms. 1D and 2D modeling in DC-resistivity is computationally inexpensive, allowing the use of global optimization methods (GOMs) to solve 1.5D and 2D inverse problems with flexibility in constraint incorporation. Changes in the cost function, either in the constraints or data fitting criteria, can be easily performed, since each term of the cost function is properly normalized to allow the approximate invariance of the Lagrange multipliers. GOMs have the potential to support a computational environment suitable for quantitative interpretation in which the comparison of solutions incorporating different constraints is one way of inferring characteristics of the actual distribution of the underground resistivity. In this work, we developed: (i) comparison of the performances of the Simulated Annealing (SA), Genetic Algorithm (GA) and Particle Swarm Optimization (PSO) methods to solve the 1.5D inverse problem in DC resistivity using synthetic and field data; (ii) an inversion approach based on particle swarm optimization (PSO) to solve the 2D DC-resistivity inverse problem; (iii) exploration of several constraints in the variation of log-resistivity, including spatial continuity in both  $L_1$  and  $L_2$  norms, total variation and sparsity constraints using discrete cosine and Daubechies bases. In addition, we explore the minimum inertia constraint, including the case of using the Earth's surface as the target axis, to impose the concentration of resistive or conductive materials along target axes. The main results of the comparison for the 1.5D case are: a) all methods reproduce quite well the resistivity distribution of synthetic models, b) PSO and GA are very robust to changes in the cost function and SA is comparatively much more sensitive, c) PSO first and GA second present the best computational performances, requiring smaller number of forwarding modeling than SA, and d) GA shows the best performance with respect to the final attained value of the cost function and its standard deviation, whilst SA has the worst performance in this aspect. Equally important for both 1.5 and 2D cases, from the stopping criteria of the PSO algorithm results not only the best solution but also a cluster of suboptimal quasi-solutions from which uncertainty analyses can be performed. As a result, the interpreter has freedom to perform a quantitative interpretation process based on a feedback trial-and-error inversion approach, in a similar manner he/she has when using a friendly forward modeling software, being capable of driving the solution to incorporate his/her conceptions about the geologic environment, besides appraising data fitting and stability of the obtained solutions. We present both synthetic

and field data examples for all inversion cases.

**Keywords:** Global Optimization, Simulated Annealing, Genetic Algorithms, Particle Swarm Optimization, Resistivity.

---

# Sumário

---

<b>Resumo</b>	<b>2</b>
<b>Abstract</b>	<b>4</b>
<b>Sumário</b>	<b>i</b>
<b>1 Contextualização do problema</b>	<b>1</b>
1.1 Objetivos . . . . .	2
1.1.1 Objetivo Geral . . . . .	2
1.1.2 Objetivos Específicos . . . . .	2
1.2 Organização do texto . . . . .	2
<b>2 Manuscrito submetido: "Customizing constraint incorporation in DC-resistivity inverse problems: a comparison among three global optimization methods."</b>	<b>3</b>
<b>3 Manuscrito submetido: "Freedom to change constraints in a feedback inversion approach of 2D resistivity data using PSO"</b>	<b>60</b>
<b>4 Considerações Finais</b>	<b>132</b>
<b>Referências bibliográficas adicionais</b>	<b>134</b>
<b>Apêndice A - Modelagem em eletrorresistividade</b>	<b>135</b>
<b>Apêndice B - Pseudo-códigos do SA, GA e PSO</b>	<b>140</b>

---

# Capítulo 1

## Contextualização do problema

---

Problemas inversos em geofísica usualmente resultam na necessidade de encontrar um vetor de parâmetros  $X \in \mathbb{R}^m$  (parâmetros de um modelo de Terra) que explique um vetor de dados experimentais  $\mathbf{d}^{obs} \in \mathbb{R}^n$  (as medidas ou observações geofísicas) através do funcional  $\mathbf{d}^{calc}$ . O cálculo do funcional  $\mathbf{d}^{calc}(\mathbf{X})$  corresponde ao problema da modelagem geofísica ou problema geofísico direto. Dada a necessidade de explicar as observações geofísicas, os problemas geofísicos inversos em geral resultam em problemas de ajuste de dados – em alguma norma  $\ell_p$  – da seguinte forma:

$$\min \Phi_a[\mathbf{d}^{calc}(\mathbf{X}), \mathbf{d}^{obs}, p] = \frac{1}{N} \left\| \mathbf{d}^{calc} - \mathbf{d}^{obs} \right\|_{\ell_p}^p \quad (1.1)$$

onde  $N$  é número de observações e designaremos solução por  $X^*$ . Estes problemas são geralmente mal postos no sentido de Hadamard (Tikhonov and Arsenin, 1977), o termo mal posto podendo aqui significar a existência de muitas soluções, mas sobretudo a presença de instabilidade; ou seja, o fato de que pequenas perturbações em  $\mathbf{d}^{obs}$ , a exemplo de ruídos presentes nas observações geofísicas, podem resultar em grandes variações na solução.

A saída clássica para esta deficiência está na regularização da solução (Tikhonov and Arsenin, 1977), isto é, na introdução de restrições ou vínculos em  $X^*$ . Na prática geofísica, isto comumente significa trocar o problema descrito na Eq. 1.1 por

$$\min F(X) = \Phi_a[\mathbf{d}^{calc}(\mathbf{X}), \mathbf{d}^{obs}, p] + \mathcal{R}(\mathbf{X}, \alpha) \quad (1.2)$$

em que  $\mathcal{R}(\mathbf{X}, \alpha)$  – designado de funcional regularizador – é alguma função que introduz uma melhora significativa no condicionamento do problema original, quando  $\alpha \neq 0$ , mas que, ao mesmo tempo, conduza à solução do problema original, à medida que  $\alpha \rightarrow 0$ .

O uso do funcional regularizador  $\mathcal{R}(\mathbf{X}, \alpha)$  no problema estendido (Eq. 1.2) implica a incorporação de um vínculo na solução e tem como contrapartida inevitável a introdução de um viés nesta solução.

Nesta tese trataremos de problemas não lineares que admitem a possibilidades de múltiplas soluções. Além disso, admitem um grande número de diferentes vínculos. Daremos ênfase especial ao estudo da incorporação dos vínculos de suavidade e desigualdade (e.g. Barbosa et al., 1997, Constable et al., 1987), mínimo momento de inércia (e.g. Ajo-

Franklin et al., 2007, Guillen and Menichetti, 1984, Last and Kubik, 1983 ) e esparsidade (e.g. Jafarpour et al., 2009, Rudin et al., 1992 ). O vínculo de esparsidade é particularmente importante porque possibilita a obtenção de soluções que apresentam nitidez na definição das bordas dos corpos anômalos (e.g. Youzwishen and Sacchi, 2006 ).

Para facilitar a implementação e flexibilidade na escolha destes diversos vínculos será utilizado algoritmos de otimização global Simulated Annealing (SA), Algoritmo Genético (GA) e Particle Swarm Optimization (PSO).

## 1.1 Objetivos

### 1.1.1 Objetivo Geral

O objetivo principal desta tese é contribuir para solução e interpretação de problemas inversos em eletrorresistividade com uso e flexibilidade de diversos vínculos usando algoritmos de otimização global.

### 1.1.2 Objetivos Específicos

Entre os objetivos específicos buscados no estudo podem ser citados:

- Desenvolvimento e implementação algoritmos para solução dos problemas inversos em eletrorresistividade 1.5D e 2D.
- Utilização de critérios de parada para cada termo do funcional.
- Obtenção de quase-soluções obtidas pelo critério de parada.
- Aplicação dos algoritmo de inversão em diferentes testes sintéticos visando diagnosticar qual método (SA, GA ou PSO) é relativamente mais robusto, computacionalmente eficiente e flexível para a incorporação de diferentes vínculos.
- Adaptação da inicialização do PSO utilizando distribuição triangular para a inversão 2D.
- Aplicação de feedback interpretativo na escolha e uso de vínculos em partições na malha do modelo interpretativo em dados sintéticos e reais.
- Realização de análise de incerteza dos conjunto de quase-soluções subótimas obtidas pelo critério de parada.

## 1.2 Organização do texto

Os capítulos a seguir tratam dos dois artigos submetidos, exigidos para a apresentação do referido trabalho. Nos artigos mostram-se os resultados finais, já submetidos, e em seguida a conclusão de todo o trabalho. Nos apêndices A e B apresentam-se brevemente o embasamento teórico referente as modelagens utilizadas, bem como os pseudo códigos dos algoritmos implementados.

---

## Capítulo 2

# **Manuscrito submetido: "Customizing constraint incorporation in DC-resistivity inverse problems: a comparison among three global optimization methods."**

---

Manuscrito submetido e realizado a primeira revisão à Geophysics, de Qualis CAPES A1. Corresponde aos resultados obtidos com inversão em eletrorresistividade 1.5D usando vínculos de suavidade na norma  $\ell_1$  e  $\ell_2$  em ambientes geológicos simples e complexos. Uma comparação foi realizada usando algoritmos de otimização global SA, AG e PSO.

Nas próximas páginas segue o manuscrito completo do artigo.

**Customizing constraint incorporation in DC-resistivity  
inverse problems: a comparison among three global  
optimization methods.**

**Francisco M. Barboza<sup>\*§</sup>, Walter E. Medeiros<sup>\*†</sup>, and Jerbeson M. Santana<sup>\*</sup>**

*\*Programa de Pós-graduação em Geodinâmica e Geofísica.*

*†Departamento de Geofísica*

*Centro de Ciências Exatas e da Terra*

*Universidade Federal do Rio Grande do Norte – UFRN*

*59.072-970, Natal/RN, Brazil.*

*E-mail: walter.ufrn@gmail.com*

*§ On leave from Universidade Federal do Acre – UFAC*

(August 30, 2017)

Running head: *Customizing constraint incorporation*

**ABSTRACT**

1D forward modeling in 1DC-resistivity is actually computationally inexpensive, allowing global optimization methods (GOMs) usage to solve 1.5D inverse problems with flexibility in constraint incorporation. GOMs have potential to support a suitable computational environment for quantitative interpretation in which the comparison of solutions incorporating different constraints is a way to infer characteristics of the actual subsurface resistivity distribution. To achieve this potential, the chosen GOM must be robust to changes in the cost function and also be computationally efficient. The performances of the Simulated Annealing (SA), Genetic Algorithm (GA) and Particle Swarm Optimization (PSO) methods for

solving the 1.5D inverse problem in DC-resistivity are then compared using synthetic and field data. The main results are: a) all methods reproduce quite well the resistivity distribution of synthetic models, b) PSO and GA are very robust to changes in the cost function and SA is comparatively much more sensitive, c) PSO first and GA second present the best computational performances, requiring smaller number of forwarding modeling than SA, and d) GA shows the best performance with respect to the final attained value of the cost function and its standard deviation, whilst SA has the worst performance in this aspect. To put into effective operation, the methods can be classified from easy to difficult in the order PSO, GA and SA. This is a consequence of robustness to changes in the cost function and of the underlying simplicity of the associated equations. To exemplify a suitable environment for quantitative interpretation using GOMs, we compare solutions with norms 2 and 1 in the lateral continuity constraints of both resistivity and layer depth as a manner of detecting faults. GOMs provide additionally the important benefit of furnishing not only the best solution but also a set of suboptimal quasi-solutions from which uncertainty analysis can be performed.

**Keywords:** Global optimization, Simulated annealing, Genetic algorithm, Particle swarm optimization, Resistivity method.

## INTRODUCTION

The quantitative interpretation of geophysical data using computers has been done by basically two manners. The first one is to use a trial-and-error approach based on flexible modeling codes, whilst the second manner is based on using inversion codes incorporating constraints on the model parameters. Usually, when the interpreter changes from the first to the second interpretation manner, he/she loses a lot of flexibility in facing geologic complexities because in the available inversion codes the set of constraints is in general too limited. We present a quantitative inversion approach where ultimately we are trying to give back to the interpreter the lost flexibility. We use as example the simple 1.5D inversion problem in DC-resistivity. The proposed quantitative interpretation approach is based on using global optimization methods to support a computational environment offering high flexibility and easiness in customizing constraint incorporation in the inverse problem.

Solving a geophysical inverse problem consists in estimating the parameters of an Earth model honoring the known geological information. This problem is frequently formulated as an optimization problem where the solution is the minimum of a cost function involving two parcels: one demanding that observed and modeled data are fitted and the other imposing constraints on the model parameters (Tikhonov and Arsenin, 1977). Ideally the imposed constraints would incorporate the known (or admitted valid) geological information in order to stabilize the solution under the presence of small variations in the observed data (Silva et al., 2001b). However, as far as the imposed constraints do not match the actual geology the two parcels in the cost function might be in conflict so that the solution is a point to be chosen in a Pareto front (Miettinen, 2012; Kozlovskaya et al., 2007; Schwarzbach et al., 2005).

The methods to solve nonlinear inverse problems might be classified in two major groups: local and global (GOM) optimization methods. A local method tries to obtain a local minimum of the cost function based on an iterative process, where a given starting model is updated with a sequence of steps, each step taking into account the local gradient of the cost function in order to continuously decrease it (Gill et al., 1981). On the other hand, a GOM tries to obtain the global minimum of the cost function using often metaheuristics mimicking an adaptation strategy found in Nature. The strategy allows to implement an iterative evolution to the models that, although do not necessarily follows a monotonous decreasing path for the cost function, might eventually converge to its global minimum (e.g. Van Laarhoven and Aarts, 1987; Haupt and Haupt, 2004). Local methods are the most commonly used optimization methods in geophysics. However, Simulated Annealing (SA) (e.g. Kirkpatrick et al., 1983; Sen and Stoffa, 1991, 1995; Rucker and Ferré, 2005; Santos et al., 2006; Pei et al., 2007; Wang et al., 2012; Biswas and Sharma, 2014), Genetic Algorithm (GA) (e.g. Goldberg, 1989; Stoffa and Sen, 1991; Sen and Stoffa, 1995; Başokur et al., 2007; Jha et al., 2008; Morgan et al., 2012; Attwa et al., 2014), and Particle Swarm Optimization (PSO)(e.g. Eberhart and Kennedy, 1995; Shaw and Srivastava, 2007; Martínez et al., 2010; Fernández-Martínez et al., 2012; Tronicke et al., 2012) are GOMs increasingly in use in geophysics.

Compared to local methods, GOMs offer higher flexibility in cost function design but require much higher computational cost because huge numbers of cost function evaluation might be necessary (Sen and Stoffa, 1995). The ratio of cost function evaluations of a GOM to a local method may easily attain  $10^4$ . Given that in geophysical inverse problems each cost function evaluation requires a forward modeling, the use of GOMs is possible only when the forward modeling is computationally inexpensive, a fact that remains the major obstacle in

using GOMs. However, 1D or even 2D computationally inexpensive forward modeling is now a reality in many important cases in geophysics, like in many electromagnetic methods (e.g. Abubakar et al., 2008) and particularly in direct current (DC) resistivity (e.g. Swarzenski et al., 2016; Woodbury et al., 2016). But computational cost is not the only obstacle to GOMs usage; another one is the fact that the interpreter must be convinced of some of their advantages over local methods that might compensate their higher computational cost. Keeping in mind the purpose of restoring to the interpreter the flexibility of interpretation present just in trial-and-error modeling approaches, we present below a context where the use of a GOM was shown to be advantageous in DC-resistivity method. Similar contexts might be found in other methods where computationally inexpensive forward modeling is also available.

The use of a GOM might be advantageous when the interpreter requires high flexibility in choosing and changing both the constraints on the model parameters and/or the fitting criteria between observed and modeled data, including the use of nondifferentiable constraints and/or fitting criteria. In this context, once a GOM is implemented, changes in the cost function are potentially easy to be performed. In this way the higher computational cost of a GOM would be compensated by the lower investment in human work because, in comparison, adapting new constraints or fitting criteria in local methods are usually very time consuming in manhours particularly when the new terms are nondifferentiable. In fact, according to two classic references in optimization distant in time for 28 years, Gill et al. (1981) and Conn et al. (2009), computing derivatives is the single most common source of user error in applying optimization softwares. In other words, the use of a GOM might be advantageous in a quantitative interpretation context where the interpreter is trying to infer properties of the actual subsurface distribution of resistivity, by comparing

different estimates obtained with different constraints on the model parameters and/or different fitting criteria between observed and modeled data. In this context, he/she makes the advantageous exchange of manhours by computer time.

In this work we compare SA, GA, and PSO performances to solve the 1.5D inversion problem in DC-resistivity, that is inversion imposing lateral continuity constraints on the model parameters but using 1D layer cake forward modeling (e.g. Gyulai and Ormos, 1999; Auken et al., 2005). We stress that we do not simply compare computational performances but we are particularly interested in evaluating robustness to changes in the cost function. In this context, using both synthetic and field data, we compare log-resistivity and depth to the layer bottom estimates obtained with lateral continuity constraints using both the  $\ell_1$  and  $\ell_2$  norms as an example of a flexible way to infer characteristics of the actual subsurface resistivity distribution, in this case the possible presence of vertical faults (Loke et al., 2003). For the sake of completeness, we firstly present the 1.5D DC-resistivity inversion problem and the adopted versions of SA, GA, and PSO algorithms.

## 1.5D DC-RESISTIVITY INVERSION PROBLEM

Let us consider the quantitative interpretation of a set of  $J$  DC-resistivity soundings using a common layer cake model specified by  $L$  layers. For the sake of simplicity, we assume that all soundings are aligned forming a traverse. There are thus  $N_{par} = J(2L - 1)$  model parameters, among these there are  $JL$  parameters of resistivity (arranged in the vector  $\boldsymbol{\rho}$ ) and  $J(L - 1)$  parameters of depth to the bottom of each layer (arranged in the vector  $\boldsymbol{h}$ ). From now on we refer to the latter parameters just as layer depths. Let us compose the  $N_{par}$ -size vector  $\mathbf{X}$  with all model parameters ( $\mathbf{X}^T = (\boldsymbol{\rho}^T \ \boldsymbol{h}^T)$ ). In addition, let  $\mathbf{d}^{obs}$  be the  $N_{obs}$ -size vector composed by the apparent resistivity measurements of all soundings

(observations).

Assuming that the effects caused by lateral heterogeneities on the resistivity soundings can be neglected,  $\mathbf{d}^{obs}$  can be described by the equation

$$\mathbf{d}^{obs} = \mathbf{d}^{cal}(\mathbf{X}) + \boldsymbol{\eta}, \quad (1)$$

where  $\mathbf{d}^{cal}(\mathbf{X})$  is the vector composed by the modeled apparent resistivities using the local 1D layer cake model below each sounding (Koefoed, 1979) and  $\boldsymbol{\eta}$  is the vector of associated discrepancies. Estimating  $\mathbf{X}$  based just on the criterion of minimizing a norm of  $\boldsymbol{\eta}$  is an ill-posed problem because this solution is unstable to small perturbations in  $\mathbf{d}^{obs}$  (Parker, 1984). To obtain stable estimates of  $\mathbf{X}$ , we solve the constrained inverse problem of minimizing (in relation to  $\mathbf{X}$ ) the cost function:

$$F[\mathbf{d}^{cal}(\mathbf{X}), \mathbf{d}^{obs}; \mu_\rho, \mu_h; p, q, r] = \Phi[\mathbf{d}^{cal}(\mathbf{X}), \mathbf{d}^{obs}; p] + \mu_\rho \Psi_\rho(\boldsymbol{\rho}; q) + \mu_h \Psi_h(\mathbf{h}; r), \quad (2)$$

where

$$\Phi = \frac{1}{N_{obs} |\sigma_\eta^2|^{p/2}} \left\| [\log(\mathbf{d}^{obs}) - \log(\mathbf{d}^{cal})] \right\|_{\ell_p}^p, \quad (3)$$

$$\Psi_\rho = \frac{1}{[(J-1) \cdot L] |\sigma_\rho^2|^{q/2}} \|D_\rho [\log(\boldsymbol{\rho})]\|_{\ell_q}^q, \quad (4)$$

$$\Psi_h = \frac{1}{[(J-1) \cdot (L-1)] |\sigma_h^2|^{r/2}} \|D_h \mathbf{h}\|_{\ell_r}^r, \quad (5)$$

for  $\mathbf{X} \in \Omega$ , a search-space imposing box constraints on each model parameter. In equation 2, the functional  $\Phi$  demands that logarithms (logs) of modeled apparent resistivities,  $\log(\mathbf{d}^{cal})$ , fit logarithms of measured apparent resistivities,  $\log(\mathbf{d}^{obs})$ , according to the norm  $\ell_p$  (equation 3). On the other hand, the functionals  $\Psi_\rho$  and  $\Psi_h$  impose lateral continuity constraints on log-resistivities and layer depths of the same layer, below adjacent pairs of soundings, according to the norms  $\ell_q$  (equation 4) and  $\ell_r$  (equation 5), respectively. The

first-order finite-difference matrix operators  $D_\rho$  (equation 4) and  $D_h$  (equation 5) express mathematically these constraints (e.g. Constable et al., 1987; Medeiros and Silva, 1996); symbolically  $D_\rho$  and  $D_h$  have sizes  $(J - 1)L \times JL$  and  $(J - 1)(L - 1) \times J(L - 1)$ , respectively. Also in equation 2,  $\mu_\rho$  and  $\mu_h$  are the associated Lagrange multipliers that must be chosen so that a trade-off between fitting the observations and incorporating both constraints is satisfied (e.g. Hansen, 1992). Finally,  $\sigma_\eta^2$  (equation 3),  $\sigma_\rho^2$  (equation 4) and  $\sigma_h^2$  (equation 5) are the variances of the discrepancies between measured and modeled apparent log-resistivities, pairs of laterally adjacent layer log-resistivities, and pairs of laterally adjacent layer depths, respectively.

Note that depending on  $p$ ,  $q$ , and  $r$  (equations 3 to 5), that specify the norms  $\ell_p$ ,  $\ell_q$ , and  $\ell_r$ , respectively, the functionals  $\Phi$ ,  $\Psi_\rho$  and  $\Psi_h$  might be differentiable or not. According to the chosen norm, the net effect of  $\Psi_h$  (and analogously of  $\Psi_\rho$ ) is to penalize larger discrepancies between all pairs of adjacent layer depths, as in the case  $p = 2$ , or to allow localized jumps, as in the case  $p = 1$ .

Denominators in the ratios of equations 3 to 5 were chosen in order to normalize the functionals. These normalizations are of great importance because, after them, the task of assigning values to the Lagrange multipliers  $\mu_\rho$  and  $\mu_h$  is facilitated because we may now consider these values as percentages. More importantly, these normalizations promote robustness to the GOMs. We verified with preliminary tests that values of  $\mu_\rho$  and  $\mu_h$  in the range 0.01 to 0.1 are sufficient to stabilize the solutions (usually  $\mu_\rho$  requires higher values). The variances  $\sigma_\eta^2$ ,  $\sigma_\rho^2$ , and  $\sigma_h^2$  might be specified by the interpreter based on his/her experience or they can be estimated using preliminary inversion tests, as we did in the examples that are later presented. In the case of  $\sigma_\eta^2$ , it can alternatively be estimated using information about data quality.

If GOMs are used to solve equation 2, minor code modifications are done in the algorithms in order to introduce changes in the search space  $\Omega$ , or in the fitting criterium  $\Phi$ , or in the constraints  $\Psi_\rho$  and  $\Psi_h$ . This is the reason why using GOMs in inversion problems might give back to the interpreter the lost flexibility he/she has when using modeling codes to perform a trial-and-error interpretation approach. However, to allow flexibility in changing the cost function and/or the search space, the chosen GOM must be sufficiently robust to these changes. The normalization imposed to the terms composing equation 2 is a key step in this direction; without normalization, even a simple change in the number of apparent resistivity measurements, for example, would require that the Lagrange multipliers be updated. Similar care with normalization must be taken when introducing any other constraint term in equation 2.

## GLOBAL OPTIMIZATION ALGORITHMS

We summarize the adopted versions of SA, GA, and PSO which are all of probabilistic nature. We describe also common stopping criteria.

### Simulated Annealing (SA)

SA was proposed by Kirkpatrick et al. (1983) to solve multivariate combinatorial optimization problems. SA simulates a cooling process where a material, starting at a high temperature liquid phase, is cooled to a low temperature solid phase. The key point is that the temperature is lowered so slowly that all the constituents can organize into a perfect crystalline state associated to a global minimum of energy. We implement the classic version of SA (Kirkpatrick et al., 1983) which is very well described in Park and Kim (1998).

We use the geometric cooling schedule (Kirkpatrick et al., 1983)

$$T_k = \alpha^k T_0, \tag{6}$$

where  $T_k$  is the temperature in the epoch  $k$  (a stage where the temperature is maintained constant),  $T_0$  is a given initial temperature, and  $\alpha$  is the cooling factor. Typically  $0.80 < \alpha < 0.99$  because values lower than 0.80 may result in excessively rapid cooling schedules (Yang, 2010). We use  $\alpha = 0.95$ .

The search for the global minimum is initialized with a point randomly chosen in the search space  $\Omega$ . Let  $\mathbf{X}^*$  represent this initial point and also any of its later modifications, named current solutions, until the process is finished and the resulting  $\mathbf{X}^*$  becomes an estimate of the global minimum. For each  $T_k$ , SA should perform  $N_T$  perturbations  $\mathbf{X}_u$  in a neighborhood of  $\mathbf{X}^*$  until the thermal equilibrium would be reached. In principle, the epoch length  $N_T$  would depend on  $T_k$ . However, ascertaining for each  $T_k$  whether the thermal equilibrium has been reached is a difficult task (Persson, 2003). We find out that good results can be obtained using the simpler approach of making  $N_T$  equal to a fixed proportion of the number of parameters  $N_{par}$ , regardless of  $T_k$ . We use  $N_T$  in the range 3.5 to 5  $N_{par}$ .

Perturbations  $\mathbf{X}_u$  are calculated with the equation (Van Laarhoven and Aarts, 1987)

$$\mathbf{X}_u = \mathbf{X}^* + \sqrt{T_k} \cdot \frac{\mathbf{r}}{\|\mathbf{r}\|}, \tag{7}$$

where  $\mathbf{r}$  is a vector whose inputs are Gaussian pseudorandom numbers with zero mean and standard deviation equal to 1. For each trial  $\mathbf{X}_u$ , the variation  $\Delta F$  of the cost function  $F(\mathbf{X})$  (equation 2)

$$\Delta F = F(\mathbf{X}_u) - F(\mathbf{X}^*) \tag{8}$$

is calculated. If  $\Delta F \leq 0$ ,  $\mathbf{X}_u$  is accepted and replaces  $\mathbf{X}^*$ . On the other hand, if  $\Delta F > 0$ ,  $\mathbf{X}_u$  might be accepted with acceptance-probability (Metropolis et al., 1953)

$$P(\Delta F) = \exp(-\Delta F/T_k) . \quad (9)$$

Eventual acceptances of  $\mathbf{X}_u$ , even when  $\Delta F > 0$ , allow that SA may possibly escape from local minima. This is the key difference between SA and local methods, analog conditions also are present in GA and PSO. The cooling process is continued until stopping criteria are attained.

Preliminary statistics on the variations  $\Delta F$  can be obtained by doing a series of random visits in the search space  $\Omega$ . Then  $T_0$  can be calculated using the equation (Johnson et al., 1989)

$$T_0 \approx -\frac{\max(|\Delta F|)}{\ln(P_0)} , \quad (10)$$

where  $P_0$  ( $\approx 0.95$ ) is a given initial acceptance-probability.

## **Genetic Algorithm (GA)**

GA is an evolutionary probabilistic GOM that simulates the process of Darwinian evolution (e.g. Mitchell, 1995). The key idea of GA is that, after many generations of a given population, subjected to crossovers following the Darwinian rule that the most adapted individuals are most likely to reproduce, a very well-adapted individual (the global solution) will appear in the offspring. We use the classic version of Goldberg (1989), which is easily programmable. This version of GA is based on standard binary encoding, wheel type selection, uniform crossover, and mutation on a population of fixed number individuals. No elitism criteria is used.

Each individual  $\mathbf{X}_i$  of a population of size  $N_P$  (even number) represents a trial solution of the cost function  $F(\mathbf{X})$  (equation 2).  $\mathbf{X}_i$  is encoded as a chromosome, which is composed by concatenated chains of sets of bits (sequences of 1 and 0), each chain encoding a model parameter value (Mitchell, 1995). The fitness of  $\mathbf{X}_i$  is measured with the function

$$f_i = \exp[-F(\mathbf{X}_i)], \quad (11)$$

so that high fitness values are associated with low values of the cost function.

The initial population is randomly chosen in the search space  $\Omega$ . Analogously to the epoch size in SA, we use  $N_P$  in the range 3.5 to 5  $N_{par}$ . For the current population, the operations of selection to mate, crossover, and mutation are performed. In the selection, pairs of individuals  $\mathbf{X}_i$  and  $\mathbf{X}_j$  are randomly chosen using a wheel that associates to each individual  $\mathbf{X}_i$  the probability  $p_i$  of reproducing given by (Goldberg, 1989)

$$p_i = \frac{f(\mathbf{X}_i)}{\sum_{j=1}^{N_P} f(\mathbf{X}_j)}. \quad (12)$$

We use a crossover rate (probability of actually performing a crossover) equal to 0.80. To form a new generation,  $N_P/2$  crossovers are performed, where each individual may participate in more than one (or even none) crossovers, accordingly to its probability. The uniform crossover (Goldberg, 1989) mimetizes a sexual reproduction process where a pair of parent chromosomes exchange genetic material to form a pair of offspring chromosomes. The new individuals are unconditionally accepted.

The mutation may change randomly a bit in an offspring chromosome. This operation promotes diversity in the population but can also cause slow convergence when the mutation acceptance probability is high. A good trade-off is to use an acceptance probability around 0.001 (Back, 1993; Jha et al., 2008). The joint operations of crossover and mutation may result (or not) individuals with higher fitness (Goldberg, 1989).

Once the operations of selection, crossover, and mutation are concluded, the offspring population substitutes fully the parent population. The generation process is continued until stopping criteria are attained.

## Particle Swarm Optimization (PSO)

PSO simulates the social behavior of a swarm of individuals of the same species, like birds, in the search for food (Kennedy et al., 2001). The key idea is that while searching for food, the particles (birds) are either scattered or go together, but always sharing all information; eventually when a very good place is found by any of the particles, the entire swarm flocks to this place. We use the classic version of PSO described by Suganthan (1999).

The swarm is formed by  $N_S$  particles. We use  $N_S$  in the range 3.5 to 5  $N_{par}$  in an analogous manner to SA and GA. Each particle  $i$  of the swarm may occupy different positions  $\mathbf{X}_i^k$  of the search space  $\Omega$  at the time (iteration)  $k$ .  $\mathbf{X}_i^k$  are then trial solutions to the cost function  $F(\mathbf{X})$  (equation 2), being the initial positions randomly chosen in the search space  $\Omega$ . At iteration  $k$  the positions  $\mathbf{X}_i^k$  of all particles  $i$  ( $i = 1, \dots, N_S$ ) are updated using the equation

$$\mathbf{X}_i^k = \mathbf{X}_i^{k-1} + v_i^k, \quad (13)$$

where the step  $v_i^k$  results from a compromise of three trends: the previous step  $v_i^{k-1}$  ( $v_i^0 = 0$ ), the best position already occupied by the particle itself  $\mathbf{X}_i^B$ , and the best position already occupied by a particle of the swarm  $\mathbf{X}^{BB}$ , accordingly to the equation

$$v_i^k = \omega.v_i^{k-1} + c_1.r_1(\mathbf{X}_i^B - \mathbf{X}_i^{k-1}) + c_2.r_2(\mathbf{X}^{BB} - \mathbf{X}_i^{k-1}). \quad (14)$$

In the above equation,  $\omega$ ,  $c_1$  and  $c_2$  are the control parameters named as inertia weight, cognitive parameter, and social parameter, respectively. Good convergence of the solutions

were obtained by using  $\omega = 0.72$  and  $c_1 = c_2 = 2$ , which are values compatible with those ones reported in the literature (e.g. Clerc and Kennedy, 2002; Trelea, 2003; Fernández-Martínez and García-Gonzalo, 2008). On the other hand,  $r_1$  and  $r_2$  (equation 14) are pseudorandom numbers uniformly distributed in the range 0 to 1 (Haupt and Haupt, 2004). The iterations continue until stopping criteria are attained, when the global minimum is associated with the resulting best position  $\mathbf{X}^{BB}$  (Kennedy et al., 2001).

### Common stopping criteria

To compare SA, GA, and PSO we use the common nomenclature of stage to refer to an epoch size in SA, a generation in GA, and a sweep of the swarm in PSO, because the number of cost function evaluations at each stage are approximately the same in all cases (at least  $N_T$ ,  $N_P$ , and  $N_S$ , respectively).

To establish common stopping criteria we use a Cauchy type convergence criterion (e.g. Bartle, 1964) to each parcel  $\Phi$ ,  $\Psi_\rho$ , and  $\Psi_h$  of the cost function  $F(\mathbf{X})$  (equation 2). Testing individually the convergence of each term of  $F(\mathbf{X})$  ensures not only that the observations were fitted but also that each constraint was effectively incorporated (Silva et al., 2001a). Designating  $\Phi$ ,  $\Psi_\rho$ , or  $\Psi_h$  generically by  $G$ , convergence is assumed when, for  $N_C$  consecutive times, the relative variation of  $G$  in two successive stages ( $k - 1$  and  $k$ ) is stagnated below a threshold  $\delta_G$ , that is:

$$\chi_k^G = \left\| \frac{G(\mathbf{X}_k) - G(\mathbf{X}_{k-1})}{G(\mathbf{X}_k)} \right\| \leq \delta_G, \text{ for } N_C \text{ consecutive times,} \quad (15)$$

where  $\mathbf{X}_k$  and  $\mathbf{X}_{k-1}$  are the best solutions in stages  $k$  and  $k - 1$ , respectively. We use  $N_C = 200$  and a stagnation threshold equal to  $10^{-6}$  for all cost function terms  $\Phi$ ,  $\Psi_\rho$ , and  $\Psi_h$ . Note that using a single threshold for all terms is only possible because of the

normalizations imposed in equations 3 to 5.

An extra benefit of using GOMs is the fact that, at the end of the convergence process, the interpreter has not only the best solution but also a set of suboptimal quasi-solutions, which can be used to perform uncertainty analysis (e.g. Alvarez et al., 2008; Fernández-Martínez et al., 2014; Pallero et al., 2015). Jointly, the best solution and the set of quasi-solutions, compose a cluster from which the variability of the solution can be estimated using, for example, simple statistics as mean and standard deviation of the model parameters, as we do here. Due to the convergence criteria (equation 15), we obtain clusters with  $N_C = 200$  points.

## COMPARISON AMONG SA, GA, AND PSO

### Synthetic models

To compare SA, GA, and PSO performances we use the synthetic models A and B presented in Figures 1a and 1b, respectively. Both models represent idealized sedimentary media where intermediary-depth layers, representing an aquifer, is the target for the DC-resistivity investigation. In comparison with Model B, in Model A the horizontal dimension is larger than the target depth. Synthetic apparent resistivity data for the Schlumberger array were generated for models A (21 soundings) and B (14 soundings) using respectively the 1-D layer cake (Koefoed, 1979) and 2D finite-difference (Dey and Morrison, 1979) modeling. To verify the stability of the inversion estimates in relation to small discrepancies in the synthetic data, we add to these data one realization of pseudorandom Gaussian noise with zero mean and standard deviation equal to 5% of the modeled value. These noisy data were not altered and we refer to them as observations. The resulting observations are shown in

Figures 1c and 1d as soundings, and in Figures 1e and 1f as sections, for models A and B, respectively.

Model A is simpler than Model B for two reasons. First in Model B there is a strong lateral discontinuity (a vertical offset) in the target layer around position 1 km; on the other hand there is no localized discontinuity in Model A. Second, in Model B there are strong lateral variations in the resistivity of the shallower layer (soil), a fact not present in Model A. As a result, the observations show more regular appearance in Model A (Figures 1c and 1e) than in Model B (Figures 1d and 1f). In particular, in Figure 1f it is difficult to distinguish static shift (due to variations in the soil resistivity) from vertical offsets in the target level (due to vertical faults).

For models A and B we use interpretation models with 3 and 4 layers, resulting in 105 and 98 model parameters, respectively. Although coinciding with the true values, these number of layers are consistent with the sounding curve types in both cases (Figures 1c and 1d). For both models, we perform 1.5D inversions using different constraints but keeping fixed the  $\ell_2$  norm in the data fitting criterion (functional  $\Phi$  in equation 3); the reason for this choice is the absence of outliers in the observations that, when present, demand the use of the  $\ell_1$  norm (Claerbout and Muir, 1973; Farquharson and Oldenburg, 1998; Menke, 2012). On the other hand, for functionals  $\Psi_\rho$  (equation 4) and  $\Psi_h$  (equation 5), we obtain two inversion estimates using the  $\ell_1$  and  $\ell_2$  norms. In each case, the same norm was applied to both functionals  $\Psi_\rho$  and  $\Psi_h$ . In Model B, because of the large variation in the soil resistivity, we relax the lateral continuity constraint on the resistivity of this layer. For the sake of simplicity, from now on we refer as A- $\ell_1$  case/estimates to the inversion results of Model A using the  $\ell_1$  norm, similar conventions being adopted to the A- $\ell_2$ , B- $\ell_1$ , and B- $\ell_2$  cases.

The solutions of equation 2 compose a surface - the Pareto front - immersed in the space  $(\Phi, \Psi_\rho, \Psi_h)$ . To each point of this surface is associated a pair of values of the Lagrange multipliers  $(\mu_\rho, \mu_h)$ . To ensure stability to the inversion estimates, a very good choice for these parameters is the pair of values associated to the point of the Pareto front closest to the origin. A practical approach to locate approximately this point is to implement a sequence of line searches (Rawlinson et al., 2006), as shown in Figure 2 for the B- $\ell_1$  case using PSO: starting with the trial value  $\mu_\rho = 1$ , the closest point to the origin is found to be around  $\mu_h = 0.01$  (Figure 2a); now keeping fixed this value,  $\mu_\rho$  is updated to 0.05 (Figure 2b); finally, using this latter estimate,  $\mu_h$  is confirmed to be around 0.01 (Figure 2c). As a result of similar searches, we obtain the following values for the Lagrange multipliers:  $\mu_\rho=0.1$  and  $\mu_h=0.06$  both for A- $\ell_1$  and A- $\ell_2$  cases, and  $\mu_\rho=0.1$  and  $\mu_h=0.03$  for B- $\ell_2$  case. However, as a consequence of the normalization introduced in equations 3 to 5, the estimates of  $\mu_\rho$  and  $\mu_h$  are not sensitive to variations around these values so that it would be possible to use  $\mu_\rho=0.1$  and  $\mu_h=0.05$  for all cases. This is a consequence of the fact that, in all cases, the Pareto front has a relatively large curvature around the corner closer to the origin, as illustrated in Figure 2 for the B- $\ell_1$  case.

We use  $N_T = N_P = N_S = 500$  for both models. For each case, we perform around 30 inversion runs varying the input parameters (search space  $\Omega$  and initial model/population) but keeping fixed the control parameters. Table 1 presents an statistics of the boxes delimiting the search spaces. To summarize the information each lower or upper bound is expressed as a ratio to the respective true value and the ratios are grouped into the two classes of ratios of layer depth and ratios of resistivity. Then, for each group, the minimum, mean and maximum ratios are given. The inversion results are presented in Figures 3 to 10. When an individual estimate is presented, its choice is based on the criterion that a

relatively low value of the cost function was attained. In addition, the shown percentage discrepancies are calculated as  $\delta_j = 100(E_j - T_j)/T_j$ , where  $E_j$  and  $T_j$  are the estimated and true values of a quantity  $j$ , respectively. Sometimes, for convenience we use  $|\delta_j|$  instead of  $\delta_j$ .

In the following, we compare the performances of SA, GA, and PSO with respect to the quality of the estimates, robustness of the control parameters, and computational cost. When comparing the quality of the estimates, we discuss the implications for the interpretation of using the  $\ell_1$  or  $\ell_2$  norms in functionals  $\Psi_\rho$  and  $\Psi_h$ .

### Quality of the estimates

Typical inversion results obtained for models A and B are shown in Figures 3 and 4, respectively. For Model A comparing estimates obtained with SA, GA, and PSO (Figure 3) with the true model (Figure 1a), we evaluate that all estimates are good approximations of the true model. The associated statistics of the discrepancies between true and estimated model parameter values, presented in Figures 5a and 5b for log-resistivity and layer depth, reveal that these estimates differ from the respective true values by at most 5% and 8%, respectively, independently of the used algorithm or norm. In addition, all inversion estimates honor the observations, as shown in Figures 6a and 6b.

From an interpretative point of view, the most important point to note is that, for all cases of Model A, there are practically no differences among the inversion estimates using either the  $\ell_1$  or the  $\ell_2$  norm. The  $\ell_1$  norm favours more blockly structures (e.g. Loke et al., 2003; Sun and Li, 2014) allowing that a possible localized discrepancy of resistivity and/or layer depth might appear in the inversion results. Because the A- $\ell_1$  and A- $\ell_2$  estimates

are very similar, the interpreter can infer that there are no important vertical offsets in the subsurface layers. This result is a consequence of the statistics implicitly associated with each norm and ultimately reflects the different behaviors of median and mean, associated with the  $\ell_1$ /Laplacian and  $\ell_2$ /Gaussian norm/probability density function, respectively (Menke, 2012). To exemplify, it are shown in Figures 7a and 7b the histograms resulting from PSO inversion in the A- $\ell_1$  and A- $\ell_2$  cases, respectively, for the estimated difference  $\Delta h_{j,j+1} = h_{j+1} - h_j$  of layer depths to the top interface of the second layer (the blue layer in Figure 1a) between two adjacent points  $j$  and  $j + 1$ . Note that there are no outliers in both histograms (a different result is below found when comparing the B- $\ell_1$  and B- $\ell_2$  cases). Thus, comparing estimates obtained with the  $\ell_1$  and  $\ell_2$  norms on the functionals  $\Psi_\rho$  and  $\Psi_h$  allow one to infer characteristics of the true resistivity distribution. In addition, note that the quantitative interpretation of the conductive intermediary-depth layer would be subject to the equivalence phenomenon in relation to the longitudinal conductance (Orellana, 1972) if each resistivity sounding were individually interpreted. However, when jointly interpreted with the lateral continuity constraint both on resistivity and layer depth, the equivalence is resolved because the same pair of resistivity and layer thickness has to honor the observations of different soundings where the ratio depth to layer thickness is not constant.

On the other hand, for Model B, comparing estimates obtained with SA, GA, and PSO (Figure 4) with the true model (Figure 1b), we evaluate that good approximations are obtained just in the B- $\ell_1$  cases. In fact, all the three estimates reproduce quite well the discontinuity around position 1 km. On the other hand, as expected, in the B- $\ell_2$  estimates the referred discontinuity is smoothed to such an extent that its presence would hardly be inferred from the isolated analysis of these estimates. Thus, the fact that estimates obtained

with  $\ell_1$  and  $\ell_2$  norms be different is a clue to infer the presence of discontinuities in the subsurface resistivity distribution. The fault presence can be alternatively inferred from the histograms of the estimated differences of layer depths between two adjacent points (Figures 7c and 7d) because one outlier is detected just in the B- $\ell_1$  case. We stress that both B- $\ell_1$  and B- $\ell_2$  estimates honor quite well the observations (Figures 6c and 6d, respectively) so that the non-incorporation of the discontinuity in the B- $\ell_2$  estimates can not be inferred from data fitting analysis only. In addition, even global statistics of the discrepancies between true and estimated model parameter for the B- $\ell_1$  and B- $\ell_2$  estimates (Figures 5c and 5d) are quite similar. That is, because the discontinuity is spatially very localized, its absence is not detected in global statistics.

The statistics on the model parameter estimates for both models performed with all inversion runs are shown in Figure 8. To obtain this figure, each estimate is expressed as a ratio to the respective true value and the ratios are grouped into the two classes of ratios of layer depth and ratios of log-resistivity. The statistics of the two classes show means centered at the true values with standard deviations of about 3% for the log-resistivity (Figure 8a) and 7% for the layer depth (Figure 8b), thus providing evidence for stability of the solutions. We stress that it is not necessary to run several inversions to obtain a reliable statistics of model parameter estimates because one can use the cluster of quasi-solutions obtained in just one run: as shown in Figures 8c and 8d, a similar conclusion about the stability of the solutions can be obtained from one solution cluster taking as reference the best solution of the cluster itself.

We conclude then that SA, GA, and PSO present similar performances in relation to the quality of the estimates when compared to the true models.

## Robustness of the control parameters

The values of SA, GA, and PSO control parameters greatly influence their performance. When well adjusted to a specific problem, they perform a good trade-off between exploring new regions of the search space  $\Omega$  and intensifying the search in promising subregions (Srinivas and Patnaik, 1994).

The number of parameters ( $N_{par}$ ) in the interpretation model of the inverse problem has a strong impact on the computational cost because  $N_P$  (or  $N_S$  or  $N_T$ ) is in the range 3.5 to 5  $N_{par}$ . However, from our experience,  $N_{par}$  has minor influence on the other control parameters because they depend mostly on the cost function geometry.

PSO and GA presented higher robustness of the control parameters in relation to different version of the cost function. In fact, for both methods, we simply found in sensibility tests that the values suggested in the literature (e.g. Srinivas and Patnaik, 1994; Sen and Stoffa, 1995; Schutte and Groenwold, 2005; Kirkpatrick and Sorkin, 1998) worked very well. For example, perturbing each PSO control parameter individually by up to  $\pm 15\%$  of its value produces virtually the same inversion results. For both methods, the only control parameter for which more exhaustive tests were required was swarm/population size. On the other hand, in the same situation SA presented lower robustness. The parameters controlling the cooling process ( $T_0$  and  $\alpha$  in equation 6), and the choice of the epoch size (the amount of iterations to ensure that thermal equilibrium is reached) required a relatively large number of tests. In addition,  $T_0$  requires often adaptation to particular observation data sets.

In a more qualitative fashion, the methods can be ranked from easy to difficult to put into effective operation in the order PSO, GA, and SA. This rank is a consequence not only

of the above described robustness of the control parameters but also of the fact that (for us) PSO has more simple underlying equations/operations than GA, the same occurring with GA in relation to SA.

### **Computational cost**

All numerical calculations were done in Matlab using serial processing. Figure 9 presents the statistics of computational performance of SA, GA, and PSO obtained from several inversions runs (around 30 runs for each combination model/norm). PSO first and GA second present the best performances, usually requiring smaller number of stages to converge than SA (Figure 9a). As a consequence, PSO and GA demand smaller number of forwarding modeling (Figure 9b) and CPU time (Figure 9c) than SA. Note that because the number of forward modeling for each stage is usually higher for SA (at least  $N_T$ ), the graphs of number of forwarding modeling and CPU time are not exact proportions of the graph of number of stages to converge.

Regarding the final obtained values of the cost function, usually GA presents the best performance in relation to both to the final attained value and its standard deviation (Figure 9d). In this item, SA usually presents the worst performance. As an example, Figure 10 shows that SA required more stages to converge than PSO and GA for a typical run of the Model A. An interesting feature of this figure is that the evolution of the current (or momentarily best) solution along the stages for the three GOMs show almost coinciding curves after approximately 500 stages. That is, a good quasi-solution is rapidly found by all three methods. However, the stopping criteria are attained at very different stages because of the different performances of the three GOMs in clustering the set of quasi-solutions

around a very good (or best) solution.

## FIELD DATA

We use a set of Schlumberger array soundings from a survey carried out in 1983 by the US Geological Survey (Zohdy and Bisdorf, 1989). All the apparent resistivity measurements and the quantitative interpretation of each resistivity sounding using a layer cake model are fully described in Zohdy and Bisdorf (1989). From this survey, we select 8 resistivity soundings (Figures 11a and 11b) which are approximately aligned composing a traverse. In most soundings, the maximum current electrode distance ( $AB/2$ ) varies from 2 to 5 km. According to Zohdy and Bisdorf (1989), the survey was done as part of a geothermal source research program in the region near the Lassen Volcanic National Park in USA. However, it is not our objective to discuss the geological implications of the inversion results but just to show that, once the control parameters are adjusted for an interpretation model using synthetic data, the three GOMs can be directly applied to field data, in particular GA and PSO because of their higher robustness. In this sense we use the results of Zohdy and Bisdorf (1989) as a high quality benchmark to compare our results.

The interpretation results of Zohdy and Bisdorf (1989) to the traverse of resistivity soundings are shown in Figure 12a. This figure is not an exact copy of the Figure 2 presented in page 8 of Zohdy and Bisdorf (1989). In fact we obtain Figure 12a using the estimates of resistivity and layer thickness described by Zohdy and Bisdorf (1989) and trying to reproduce, as closely as possible, the correspondence of resistivity intervals with colors in the original figure. Our inversion results are presented using the same color pattern.

We use an interpretation model with 18 layers because this is the mean number of layers

used by Zohdy and Bisdorf (1989) to interpret individually the resistivity soundings using the method of Zohdy (1989). So there are 280 parameters in the interpretation model. We use  $N_T = N_P = N_S = 1000$ . Table 1 presents an statistics of the used bounds for the search space taking as reference preliminary fast-track estimates for the model parameters obtained with 1D inversion. We use  $\mu_\rho=0.1$  and  $\mu_h=0.03$  for both  $\ell_1$  and  $\ell_2$  cases, which are shown in Figures 12 and 13, respectively. To make comparison easy in both norm cases, Figure 12a is reproduced in Figure 13a. The modeled soundings obtained with the PSO- $\ell_1$  estimates are superposed to the apparent resistivity measurements in Figures 11a and 11b and the statistics of data fitting for  $\ell_1$  and  $\ell_2$  estimates are shown in Figures 11c and 11d, respectively. In addition, the statistics on the model parameter estimates obtained with the cluster of quasi-solutions are shown in Figure 14. Finally, the evolution of the cost function and its individual parcels along the stages are shown in Figure 15.

Figures 12 and 13 show that inversion estimates obtained with the three methods reproduce quite well the solution of Zohdy and Bisdorf (1989) with minor differences. The major discrepancy, present in all inversion results, is the fact that the high conductive anomaly below the sounding number 5, present in the solution of Zohdy and Bisdorf (1989) (Figure 12a or Figure 13a), is not reproduced in any of the inversion results. Note that Zohdy and Bisdorf (1989) interpreted each sounding individually but certainly seeking to incorporate, in a qualitative way, a good lateral continuity. However, given the small lateral extension of this anomaly in their interpretation, it possibly resulted just from sounding number 5. Note that, as in synthetic Model A, the conductive intermediary-depth layers are subjected to the equivalence phenomenon in relation to the longitudinal conductance (Orellana, 1972) if each resistivity sounding is individually interpreted. Possibly the joint 1.5D inversion imposing lateral continuity constraint both on log-resistivity and layer depth resolved the

equivalence (as in synthetic Model A), resulting in the absence of the conductive anomaly in our inversion results.

Regarding the stability of the inversion estimates, the statistics on the model parameter estimates obtained with the cluster of quasi-solutions (Figure 14) reveals that both log-resistivity and layer depth estimates are stable. It is quite important to note that in all cases the solution of Zohdy and Bisdorf (1989) (shown as squares in Figure 14) is contained in the confidence region delimited by the cluster of quasi-solutions. As expected, all solutions, including the solution of Zohdy and Bisdorf (1989), honor the observations (Figures 11c and 11d). The fact that solutions imposing constraints do not negatively impact data fitting might be a clue that the constraints have geological adherence at least in most points of the subsurface (Santana et al., 2012). As in Model A, because  $\ell_1$  and  $\ell_2$  estimates are very similar, the interpreter can infer that there are no important vertical offsets in the subsurface layers, in accordance with the solution of Zohdy and Bisdorf (1989). Finally, observe in Figure 15 that the number of stages to converge and the final achieved value for the cost function are very similar to the synthetic examples, as a consequence of the normalizing factors in equations 3 to 5.

## DISCUSSION

The key point to highlight is the fact that, once a GOM is computationally implemented for an interpretative model, cost function modifications can be performed very easily. This provides a suitable computer environment for quantitative interpretation, in which the comparison of solutions with different constraints become a flexible way to evidence possible characteristics of the subsurface resistivity distribution. In this work, we explore the changing of the used norm in the lateral continuity constraints on the model parameters as a

manner of ascertaining the possible presence of localized discontinuities, such as vertical faults. However, other changes can be easily introduced in the cost function or in the search space. Just to mention a few cases: a) relaxing the constraint on a particular parameter of a certain layer (as we relax the continuity constraint on the soil resistivity in Model B because this parameter is varying in such a way that it makes no sense in constraining it); b) honoring information about some parameters which are known from outcrops or boreholes (see Medeiros and Silva (1996) on how to include these type of constraints); c) incorporating information about the dip of a given interface (that is, imposing that the depths to an interface locate around a straight line whose dip is the given one); d) for a target sandstone layer, imposing continuity constraints directly on porosity and groundwater salinity by using the Archie's law to relate formation resistivity with these quantities, and e) employing more sophisticated search spaces by imposing extra constraints on some parameters (for example, if the interpreter knows that a fault cutting a certain layer is post-tectonic, he/she might impose that the layer thickness does not change around the fault; on the other hand, if the fault is syntectonic, he/she might impose that the layer thickness obeys an inequality constraint from one side to the other of the fault). We stress that the normalizations introduced in equations 3 to 5 have a strong role in the robustness of the methods to changes in the cost function. In this sense, whenever a new constraint is introduced in the cost function, adequate normalization must be sought.

A good by-product of the GOMs is the cluster of quasi-solutions that allows to estimate the confidence region around the best solution. The size of this confidence region depends heavily on the employed constraints. In this sense, it is important to emphasize the need of requiring convergence on each isolated term of the cost function, otherwise it would be possible to obtain premature solutions in which the constraints are not properly incorporated

(Silva et al., 2001a). The interpreter can even evaluate the role played by the constraints in decreasing the confidence region, by doing comparative analyses of statistics obtained from the cluster of models that produce just satisfactory fittings of the observations (term  $\Phi$  in the equation 3), regardless of constraint incorporation, with statistics obtained from the cluster of quasi-solution, which incorporates the constraints.

## CONCLUSIONS

To use GOMs to solve inverse problems with flexibility in constraint incorporation, the chosen method must be robust to changes in the cost function and be relatively computationally efficient. We compare the performances of the most used GOMs in applied geophysics (SA, GA, and PSO) for solving the 1.5D DC-resistivity inverse problem using both synthetic and field data. As a general conclusion, PSO and GA are very robust to changes in the cost function and more computationally efficient in comparison with SA. In a more qualitative fashion, the methods can be ranked from easy to difficult to implement in the sequence PSO, GA, and SA, as consequence of both robustness to changes in the cost function and of the underlying simplicity of the associated equations. Using normalized functionals is of key importance to promote robustness. In addition, demanding convergence not only of the data fitting but also of each constraint term of the cost function is of fundamental importance to stabilize the solutions.

As an example of flexibility in cost function design allowed by a GOM, we compare the solutions incorporating different lateral continuity constraints (norms 1 and 2) as a manner of detecting faults.

An important by-product of GOMs is the cluster of quasi-solutions from which the

confidence region around the best solution can be estimated, thus allowing the interpreter to evaluate the effectiveness of the used constraints in stabilizing the solutions.

Finally we stress that, using a simple case of DC-resistivity inversion as example, we are ultimately trying to give a step forward in the direction of furnishing to practitioners in geophysics an inversion environment allowing a high flexibility in testing different constraints on model parameters as a way of facing complex geologic cases, in a similar manner he/she has in using the trial-and-error interpretation approach based on flexible modeling codes.

### **ACKNOWLEDGMENTS**

The brazilian agency CNPq is thanked for the PhD scholarship to FMB, the research fellowship and associated grant (Proc. 304301/2011-6) to WEM, and the financial support to purchase the computational infrastructure used in this study. We are very grateful to R. Mittet (associate editor), and three anonymous reviewers for the careful and constructive reviews. We thank also A. do Nascimento for the help with the English text.

## REFERENCES

- Abubakar, A., T. Habashy, V. Druskin, L. Knizhnerman, and D. Alumbaugh, 2008, 2.5 D forward and inverse modeling for interpreting low-frequency electromagnetic measurements: *Geophysics*, **73**, no. 4, F165–F177.
- Alvarez, J. F., J. F. Martínez, and C. M. Pérez, 2008, Feasibility analysis of the use of binary genetic algorithms as importance samplers application to a 1-d dc resistivity inverse problem: *Mathematical Geosciences*, **40**, no. 4, 375–408.
- Attwa, M., I. Akca, A. T. Basokur, and T. Günther, 2014, Structure-based geoelectrical models derived from genetic algorithms: a case study for hydrogeological investigations along Elbe River coastal area, Germany: *Journal of Applied Geophysics*, **103**, 57–70.
- Auken, E., A. V. Christiansen, B. H. Jacobsen, N. Foged, and K. I. Sørensen, 2005, Piecewise 1D laterally constrained inversion of resistivity data: *Geophysical Prospecting*, **53**, no. 4, 497–506.
- Back, T., 1993, Optimal mutation rates in genetic search: *Proceedings of the Fifth International Conference on Genetic Algorithms*, Morgan Kaufmann, San Mateo, CA, 2–8.
- Bartle, R. G., 1964, *The elements of real analysis*: Wiley New York.
- Başokur, A. T., I. Akca, and N. W. Siyam, 2007, Hybrid genetic algorithms in view of the evolution theories with application for the electrical sounding method: *Geophysical Prospecting*, **55**, no. 3, 393–406.
- Biswas, A., and S. Sharma, 2014, Optimization of self-potential interpretation of 2-D inclined sheet-type structures based on very fast simulated annealing and analysis of ambiguity: *Journal of Applied Geophysics*, **105**, 235–247.
- Claerbout, J. F., and F. Muir, 1973, Robust modeling with erratic data: *Geophysics*, **38**, no. 5, 826–844.

- Clerc, M., and J. Kennedy, 2002, The particle swarm-explosion, stability, and convergence in a multidimensional complex space: *IEEE transactions on Evolutionary Computation*, **6**, no. 1, 58–73.
- Conn, A. R., K. Scheinberg, and L. N. Vicente, 2009, *Introduction to derivative-free optimization*: SIAM.
- Constable, S. C., R. L. Parker, and C. G. Constable, 1987, Occam’s inversion: A practical algorithm for generating smooth models from electromagnetic sounding data: *Geophysics*, **52**, no. 3, 289–300.
- Dey, A., and H. Morrison, 1979, Resistivity modelling for arbitrarily shaped two-dimensional structures: *Geophysical Prospecting*, **27**, no. 1, 106–136.
- Eberhart, R., and J. Kennedy, 1995, A new optimizer using particle swarm theory: *IEEE, Proceedings of the Sixth International Symposium on Micro Machine and Human Science*, 39–43.
- Farquharson, C. G., and D. W. Oldenburg, 1998, Non-linear inversion using general measures of data misfit and model structure: *Geophysical Journal International*, **134**, no. 1, 213–227.
- Fernández-Martínez, J., and E. García-Gonzalo, 2008, The generalized PSO: a new door to PSO evolution: *Journal of Artificial Evolution and Applications*, **2008**, 1–15.
- Fernández-Martínez, J. L., T. Mukerji, E. García-Gonzalo, and A. Suman, 2012, Reservoir characterization and inversion uncertainty via a family of particle swarm optimizers: *Geophysics*, **77**, no. 1, M1–M16.
- Fernández-Martínez, J. L., J. Pallero, Z. Fernández-Muñiz, and L. M. Pedruelo-González, 2014, The effect of noise and tikhonov’s regularization in inverse problems. part ii: The nonlinear case: *Journal of Applied Geophysics*, **108**, 186–193.

- Gill, P. E., W. Murray, and M. H. Wright, 1981, Practical optimization: Academic press.
- Goldberg, D., 1989, Genetic algorithms in search, optimization and machine learning reading: Addison-Wisley.
- Gyulai, Á., and T. Ormos, 1999, A new procedure for the interpretation of VES data: 1.5-D simultaneous inversion method: *Journal of Applied Geophysics*, **41**, no. 1, 1–17.
- Hansen, P. C., 1992, Analysis of discrete ill-posed problems by means of the L-curve: *SIAM Review*, **34**, no. 4, 561–580.
- Haupt, R. L., and S. E. Haupt, 2004, Practical genetic algorithms: John Wiley & Sons.
- Jha, M. K., S. Kumar, and A. Chowdhury, 2008, Vertical electrical sounding survey and resistivity inversion using genetic algorithm optimization technique: *Journal of Hydrology*, **359**, no. 1, 71–87.
- Johnson, D. S., C. R. Aragon, L. A. McGeoch, and C. Schevon, 1989, Optimization by simulated annealing: an experimental evaluation. Part I, Graph partitioning: *Operations Research*, **37**, no. 6, 865–892.
- Kennedy, J. F., J. Kennedy, R. C. Eberhart, and Y. Shi, 2001, Swarm intelligence: Morgan Kaufmann Publishers.
- Kirkpatrick, S., C. D. Gelatt, M. P. Vecchi, et al., 1983, Optimization by simulated annealing: *Science*, **220**, no. 4598, 671–680.
- Kirkpatrick, S., and G. B. Sorkin, 1998, Simulated annealing: The handbook of brain theory and neural networks, MIT Press, 876–879.
- Koefoed, O., 1979, Geosounding principle-1: Elsevier Science Publications.
- Kozlovskaya, E., L. Vecsey, J. Plomerová, and T. Raita, 2007, Joint inversion of multiple data types with the use of multiobjective optimization: Problem formulation and application to the seismic anisotropy investigations: *Geophysical Journal International*, **171**,

- no. 2, 761–779.
- Loke, M. H., I. Acworth, and T. Dahlin, 2003, A comparison of smooth and blocky inversion methods in 2D electrical imaging surveys: *Exploration Geophysics*, **34**, no. 3, 182–187.
- Martínez, J. L. F., E. G. Gonzalo, J. P. F. Álvarez, H. A. Kuzma, and C. O. M. Pérez, 2010, PSO: A powerful algorithm to solve geophysical inverse problems: application to a 1D-DC resistivity case: *Journal of Applied Geophysics*, **71**, no. 1, 13–25.
- Medeiros, W. E., and J. B. Silva, 1996, Geophysical inversion using approximate equality constraints: *Geophysics*, **61**, no. 6, 1678–1688.
- Menke, W., 2012, *Geophysical data analysis: Discrete inverse theory*: Academic press.
- Metropolis, N., A. W. Rosenbluth, M. N. Rosenbluth, A. H. Teller, and E. Teller, 1953, Equation of state calculations by fast computing machines: *The journal of Chemical Physics*, **21**, no. 6, 1087–1092.
- Miettinen, K., 2012, *Nonlinear multiobjective optimization*: Springer Science & Business Media, **vol. 12**.
- Mitchell, M., 1995, Genetic algorithms: An overview: *Complexity*, **1**, no. 1, 31–39.
- Morgan, E. C., M. Vanneste, I. Lecomte, L. G. Baise, O. Longva, and B. McAdoo, 2012, Estimation of free gas saturation from seismic reflection surveys by the genetic algorithm inversion of a P-wave attenuation model: *Geophysics*, **77**, no. 4, R175–R187.
- Orellana, E., 1972, *Prospección geoelectrica en corriente continua*: Paraninfo.
- Pallero, J., J. L. Fernández-Martínez, S. Bonvalot, and O. Fudym, 2015, Gravity inversion and uncertainty assessment of basement relief via particle swarm optimization: *Journal of Applied Geophysics*, **116**, 180–191.
- Park, M.-W., and Y.-D. Kim, 1998, A systematic procedure for setting parameters in simulated annealing algorithms: *Computers & Operations Research*, **25**, no. 3, 207–217.

- Parker, R. L., 1984, The inverse problem of resistivity sounding: *Geophysics*, **49**, 2143–2158.
- Pei, D., J. N. Louie, and S. K. Pullammanappallil, 2007, Application of simulated annealing inversion on high-frequency fundamental-mode rayleigh wave dispersion curves: *Geophysics*, **72**, no. 5, R77–R85.
- Persson, P., 2003, Annealing based optimization methods for signal processing applications: PhD thesis, Blekinge Institute of Technology, Ronneby, Sweden.
- Rawlinson, N., A. M. Reading, and B. L. N. Kennett, 2006, Lithospheric structure of tasmania from a novel form of teleseismic tomography: *Journal of Geophysical Research: Solid Earth*, **111**, B02301.
- Rucker, D. F., and T. P. Ferré, 2005, Automated water content reconstruction of zero-offset borehole ground penetrating radar data using simulated annealing: *Journal of Hydrology*, **309**, no. 1, 1–16.
- Santana, F. L., W. E. Medeiros, A. F. do Nascimento, and F. H. Bezerra, 2012, Hypocentral relocation using clustering-along-planes constraints: implications for fault geometry: *Geophysical Journal International*, **190**, no. 2, 1077–1090.
- Santos, F. M., S. Sultan, P. Represas, and A. El Sorady, 2006, Joint inversion of gravity and geoelectrical data for groundwater and structural investigation: application to the northwestern part of Sinai, Egypt: *Geophysical Journal International*, **165**, no. 3, 705–718.
- Schutte, J. F., and A. A. Groenwold, 2005, A study of global optimization using particle swarms: *Journal of Global Optimization*, **31**, no. 1, 93–108.
- Schwarzbach, C., R.-U. Börner, and K. Spitzer, 2005, Two-dimensional inversion of direct current resistivity data using a parallel, multi-objective genetic algorithm: *Geophysical Journal International*, **162**, no. 3, 685–695.

- Sen, M. K., and P. L. Stoffa, 1991, Nonlinear one-dimensional seismic waveform inversion using simulated annealing: *Geophysics*, **56**, no. 10, 1624–1638.
- , 1995, *Global optimization methods in geophysical inversion*: Elsevier.
- Shaw, R., and S. Srivastava, 2007, Particle swarm optimization: A new tool to invert geophysical data: *Geophysics*, **72**, no. 2, F75–F83.
- Silva, J. B., W. E. Medeiros, and V. C. Barbosa, 2001a, Pitfalls in nonlinear inversion: *Pure and Applied Geophysics*, **158**, no. 5-6, 945–964.
- , 2001b, Potential-field inversion: Choosing the appropriate technique to solve a geologic problem: *Geophysics*, **66**, no. 2, 511–520.
- Srinivas, M., and L. M. Patnaik, 1994, Genetic algorithms: A survey: *Computer*, **27**, no. 6, 17–26.
- Stoffa, P. L., and M. K. Sen, 1991, Nonlinear multiparameter optimization using genetic algorithms: Inversion of plane-wave seismograms: *Geophysics*, **56**, no. 11, 1794–1810.
- Suganthan, P. N., 1999, Particle swarm optimiser with neighbourhood operator: *Evolutionary Computation*, **3**, 1958–1962.
- Sun, J., and Y. Li, 2014, Adaptive Lp inversion for simultaneous recovery of both blocky and smooth features in a geophysical model: *Geophysical Journal International*, **197**, no. 2, 882–899.
- Swarzenski, P. W., C. D. Johnson, T. D. Lorenson, C. H. Conaway, A. E. Gibbs, L. H. Erikson, B. M. Richmond, and M. P. Waldrop, 2016, Seasonal electrical resistivity surveys of a coastal bluff, Barter Island, North Slope Alaska: *Journal of Environmental and Engineering Geophysics*, **21**, no. 1, 37–42.
- Tikhonov, A. N., and V. Y. Arsenin, 1977, *Solutions of ill-posed problems*: V. H. Winston & Sons.

- Trelea, I. C., 2003, The particle swarm optimization algorithm: convergence analysis and parameter selection: *Information Processing Letters*, **85**, no. 6, 317–325.
- Tronicke, J., H. Paasche, and U. Böniger, 2012, Crosshole travelttime tomography using particle swarm optimization: A near-surface field example: *Geophysics*, **77**, no. 1, R19–R32.
- Van Laarhoven, P. J., and E. H. Aarts, 1987, *Simulated annealing: Theory and applications*: Springer.
- Wang, R., C. Yin, M. Wang, and G. Wang, 2012, Simulated annealing for controlled-source audio-frequency magnetotelluric data inversion: *Geophysics*, **77**, no. 2, E127–E133.
- Woodbury, B. L., R. A. Eigenberg, and T. E. Franz, 2016, Development of non-collinear arrays for use near wastewater holding ponds: *Journal of Environmental and Engineering Geophysics*, **21**, no. 4, 231–236.
- Yang, X.-S., 2010, *Engineering optimization: an introduction with metaheuristic applications*: John Wiley & Sons.
- Zohdy, A. A., 1989, A new method for the automatic interpretation of Schlumberger and Wenner sounding curves: *Geophysics*, **54**, no. 2, 245–253.
- Zohdy, A. A., and R. J. Bisdorf, 1989, *Schlumberger soundings near Lassen Volcanic National Park, California*: US Department of the Interior, Geological Survey. Open file rep. 89-670.

## LIST OF FIGURES

**Figure 1.** Synthetic models A (a) and B (b), and the respective sets of Schlumberger array DC-resistivity soundings in (c) and (d), and apparent resistivity sections in (e) and (f). For models A and B, 21 and 14 soundings are equally spaced distributed on the surface, respectively.

**Figure 2.** Projections of the Pareto front on the plane  $\Psi_\rho \times \Psi_h$  resulting from the sequence of three line searches trying to locate the values of the Lagrange multipliers  $(\mu_\rho, \mu_h)$  associated with the point of the Pareto front closest to the origin of the space  $(\Psi_\rho, \Psi_h, \Phi)$ . In a), starting with the trial value  $\mu_\rho = 1$ , the closest point to the origin is found to be around  $\mu_h = 0.01$ ; in b) now keeping fixed this value,  $\mu_\rho$  is updated to 0.05; finally, in c) using this latter estimate,  $\mu_h$  is confirmed to be around 0.01.

**Figure 3.** Model A. Typical inversion estimates using SA in (a) and (b), GA in (c) and (d), and PSO in (e) and (f). Left and right pannels show inversion results using  $\ell_1$  and  $\ell_2$  norms, respectively, in the lateral continuity constraints.

**Figure 4.** Model B. Typical inversion estimates using SA in (a) and (b), GA in (c) and (d), and PSO in (e) and (f). Left and right pannels show inversion results using  $\ell_1$  and  $\ell_2$  norms, respectively, in the lateral continuity constraints.

**Figure 5.** Cumulative distribution for the percentage discrepancy between estimated and true model parameter values for Model A in (a) and (b) and for Model B in (c) and (d), obtained with SA, GA, and PSO. For each model, left and right figures show results for log-resistivity and depth to the layer bottom, respectively. These statistics were calculated with the inversion estimates shown in Figures 3 and 4 for models A and B, respectively.

**Figure 6.** Cumulative distribution for the percentage discrepancy between modeled and observed apparent resistivity data for Model A in (a) and (b), and for Model B in (c)

and (d), obtained with SA, GA, and PSO. For each model, left and right figures are associated with the inversion results using  $\ell_1$  and  $\ell_2$  norms, respectively, in the lateral continuity constraints. These statistics were calculated with the inversion estimates shown in Figures 3 and 4 for models A and B, respectively.

**Figure 7.** Histograms resulting from PSO inversion in the A- $\ell_1$  (a), A- $\ell_2$  (b), B- $\ell_1$  (c), and B- $\ell_2$  (d) cases for the estimated difference  $\Delta h_{j,j+1} = h_{j+1} - h_j$  of layer depths to an interface between two adjacent points  $j$  and  $j + 1$ . For both models we use the top interface of the second layer. For Model A, there are no outliers both in A- $\ell_1$  and A- $\ell_2$  cases, whilst for Model B there is an outlier only in the B- $\ell_1$  case, thus evidencing the absence and presence of a fault in models A and B, respectively.

**Figure 8.** Statistics (mean  $\pm$  one standard deviation) of the percentage discrepancy between estimated and true values of the model parameter for models A and B using SA, GA, and PSO. To obtain this figure, each estimate is expressed as a ratio to the respective true value and the ratios are grouped into the two classes of ratios of layer depth and ratios of log-resistivity. (a) and (b) show results calculated with the (best) solutions for (log) resistivity and layer depth, respectively, obtained from several different inversion runs (around 30 runs for each combination model/norm). On the other hand, (c) and (d) show similar results calculated with the cluster of quasi-solutions of the particular inversion runs, whose estimates are shown in Figures 3 and 4 for models A and B, respectively.

**Figure 9.** Statistics (mean  $\pm$  one standard deviation) of quantities used to evaluate the computational performances obtained with SA, GA, and PSO in several different inversion runs of models A and B. (a) shows the statistics for the number of stages necessary to attain convergence criteria; (b), (c), and (d) show similar results for the number of forwarding modeling, normalized CPU time, and final attained value of the cost function, respectively.

In (b) the reference value to normalize all CPU times is the lower mean CPU time, which was obtained in the PSO-B- $\ell_1$  case.

**Figure 10.** Model A. Evolution of the current (or momentarily best) solution along stages of SA, GA, and PSO method associated with the respective inversion estimates shown in Figure 3. It is shown the evolutions for the cost function value (a) and its parcels  $\Phi$  (b),  $\Psi_\rho$  (c), and  $\Psi_h$  (d). Each figure shows also a zoom inset around the graph origin for better visualization. In addition, the arrows in (a) mark the stages where stopping criteria were attained in the A- $\ell_1$  cases.

**Figure 11.** Field data. (a) and (b) show the Schlumberger array DC-resistivity soundings and the respective modeled soundings for the PSO- $\ell_1$  case. (b) and (c) show the cumulative distributions for the percentage discrepancy between modeled and observed apparent resistivity data associated with the inversion results with the three methods using  $\ell_1$  and  $\ell_2$  norms, respectively, in the lateral continuity constraints. In (a) and (b), it is also shown the discrepancy results (ZB) obtained with the solution of Zohdy and Bisdorf (1989).

**Figure 12.** Field data. (a) Solution of Zohdy and Bisdorf (1989). (b), (c), and (d) show the inversion estimates obtained with SA, GA, and PSO, respectively, using the  $\ell_1$  norm in the lateral continuity constraints. In all figures, the colors represent the resistivity values according to the same color bar.

**Figure 13.** Field data. (a) Solution of Zohdy and Bisdorf (1989) (the same as in Figure 12a here repeated for ease of comparison). (b), (c), and (d) show the inversion estimates obtained with SA, GA, and PSO, respectively, using the  $\ell_2$  norm in the lateral continuity constraints. In all figures, the colors represent the resistivity values according to the same color bar.

**Figure 14.** Field data. Statistics (mean  $\pm$  one standard deviation) of the percentage

discrepancy between estimated and reference values of the model parameters obtained with SA, GA, and PSO methods. To obtain this figure, each estimate is expressed as a ratio to a respective reference value and the ratios are grouped into the two classes of ratios of log-resistivity and ratios of layer depth. The results were calculated using the cluster of quasi-solutions obtained in each inversion case taking, as reference in each case, the (best) solution of the case. Both in (a) and (b), it is superposed (as squares) in each case the mean discrepancy calculated with the solution of Zohdy and Bisdorf (1989), using the reference value of the case. Note that in all cases, the solution of Zohdy and Bisdorf (1989) is contained in the confidence region associated to the mean  $\pm$  one standard deviation.

**Figure 15.** Field data. Evolution of the current (or momentarily best) solution along stages of SA, GA, and PSO methods. These results are associated with the respective inversion estimates shown in Figures 12 and 13. It is shown the evolutions for the cost function value (a) and its parcels  $\Phi$  (b),  $\Psi_\rho$  (c), and  $\Psi_h$  (d). Each figure shows also a zoom inset around the graph origin for better visualization. In addition, the arrows in (a) mark the stages where stopping criteria were attained in the  $\ell_1$  case.

## LIST OF TABLES

**Table 1.** Statistics of the boxes delimiting the search space  $\Omega$  for the synthetic and field data cases. To summarize the information each lower or upper bound is expressed as a ratio to a reference value and the ratios are grouped into the two classes of ratios of layer depth and ratios of resistivity. Then, for each group, the minimum, mean and maximum ratios are given. The reference value is the true value, in the case of a synthetic model, or preliminary fast-track estimates with 1D inversion, in the field data case. From this table, one can obtain, for example, that the lower bounds used for the layer depths in Model B are in the range 12% - 43% with mean equal to 30%, all percentages relative to the true values.

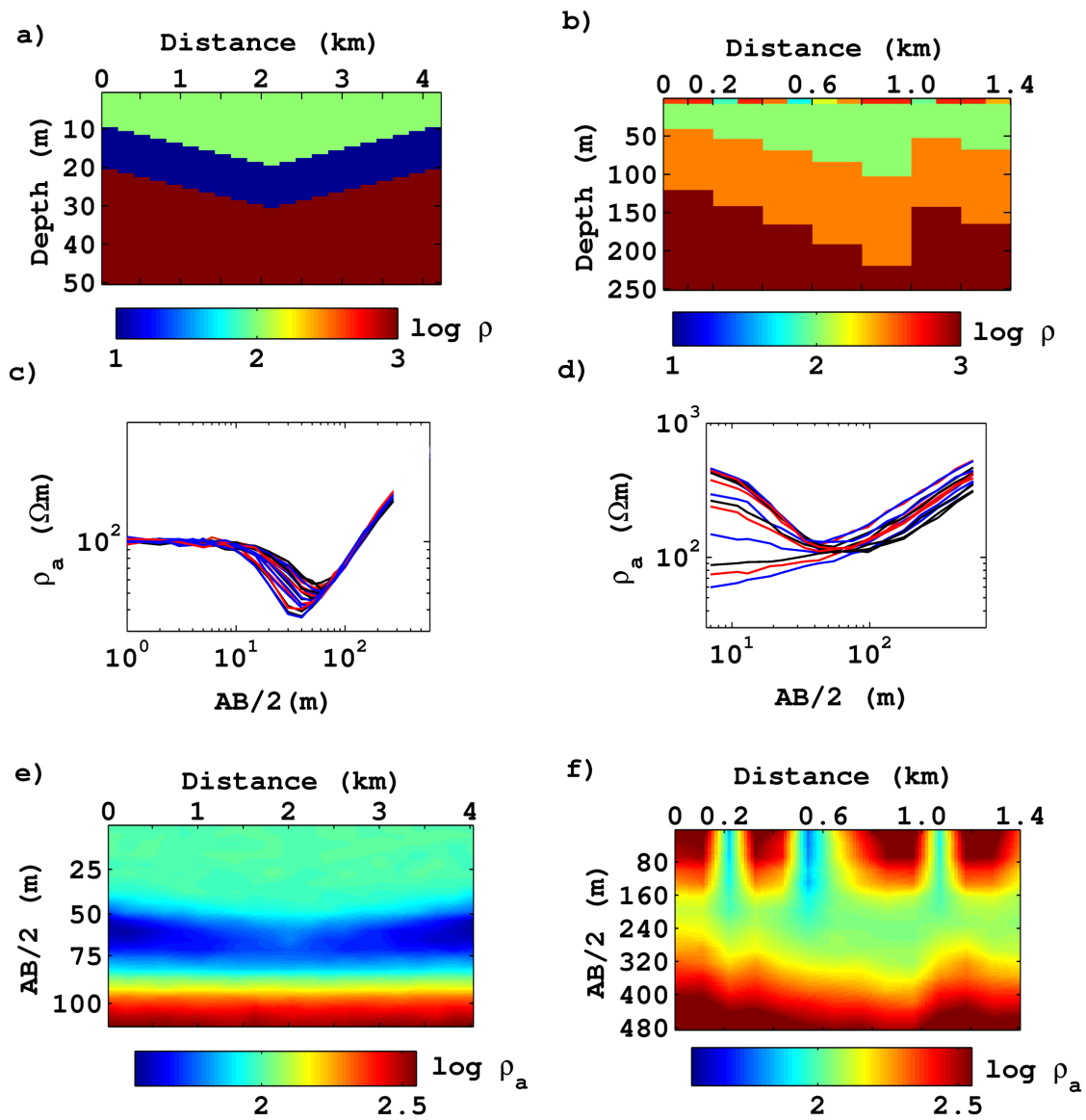


Figure 1

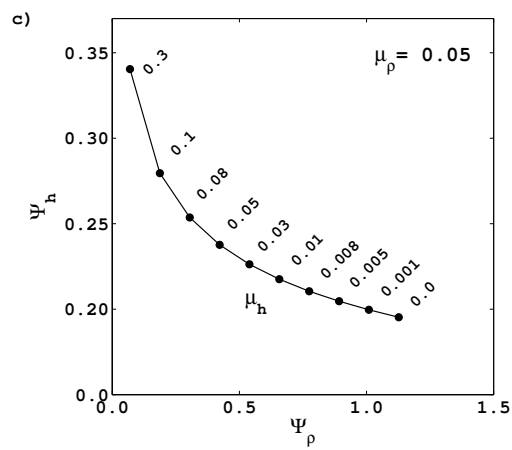
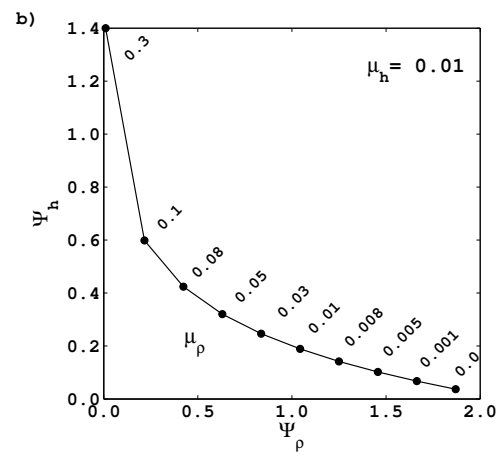
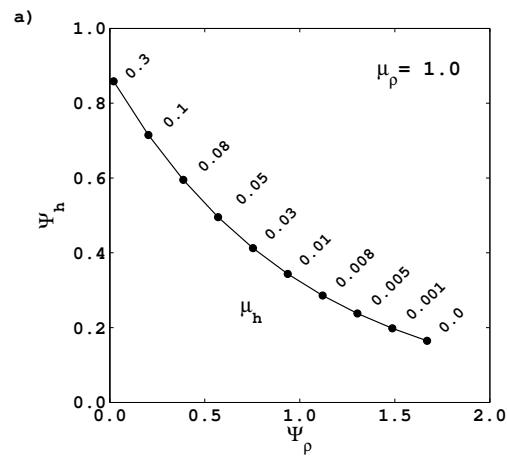


Figure 2

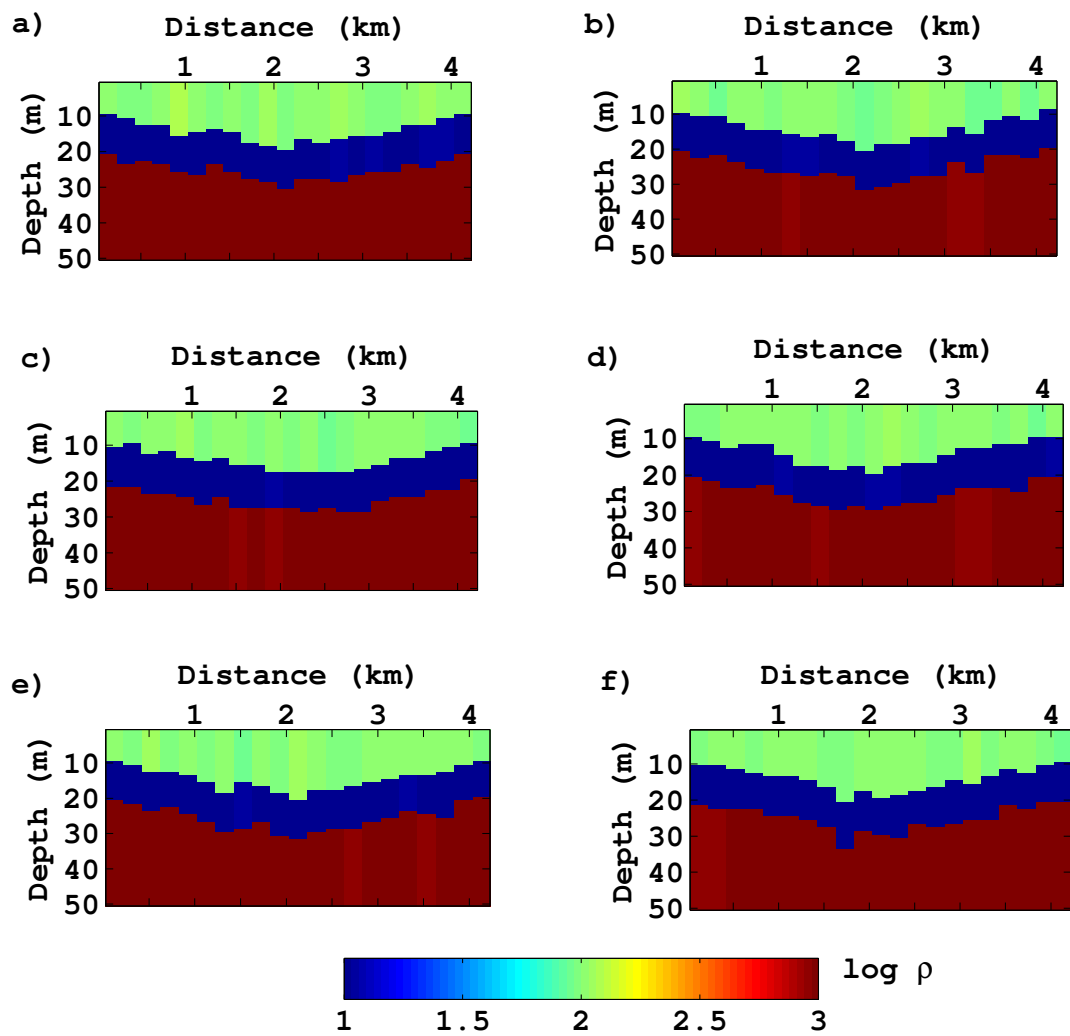


Figure 3

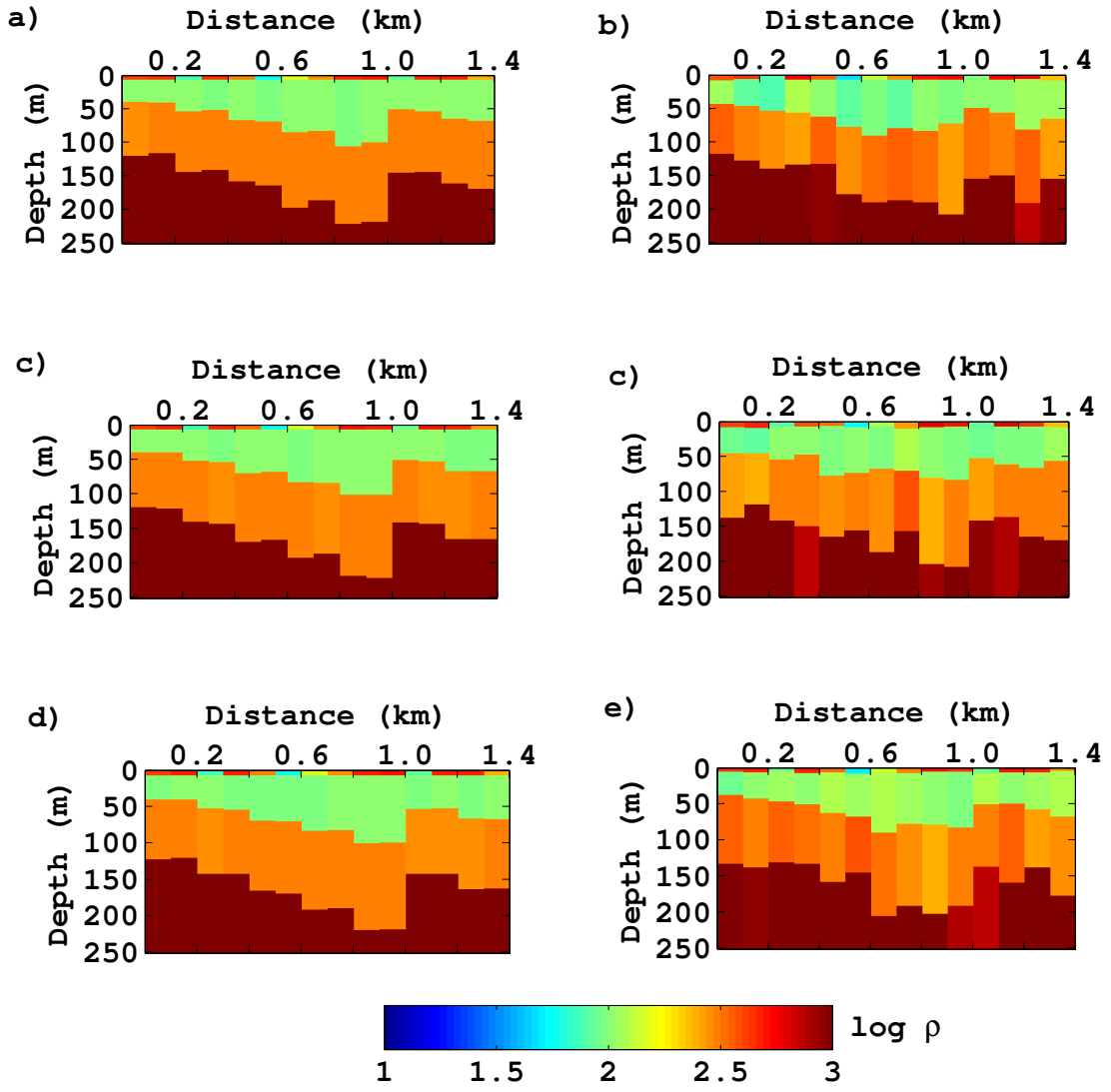


Figure 4

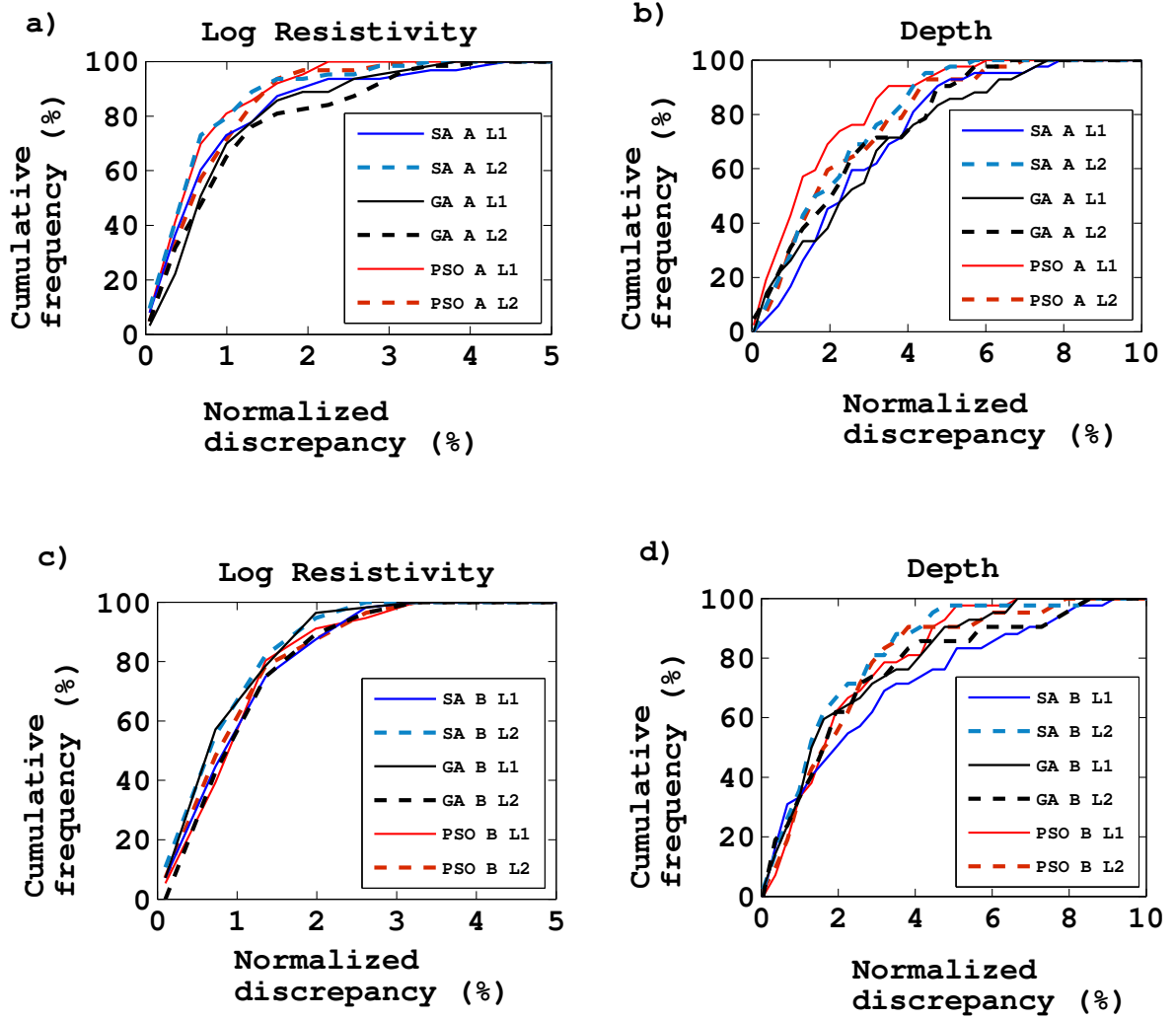


Figure 5

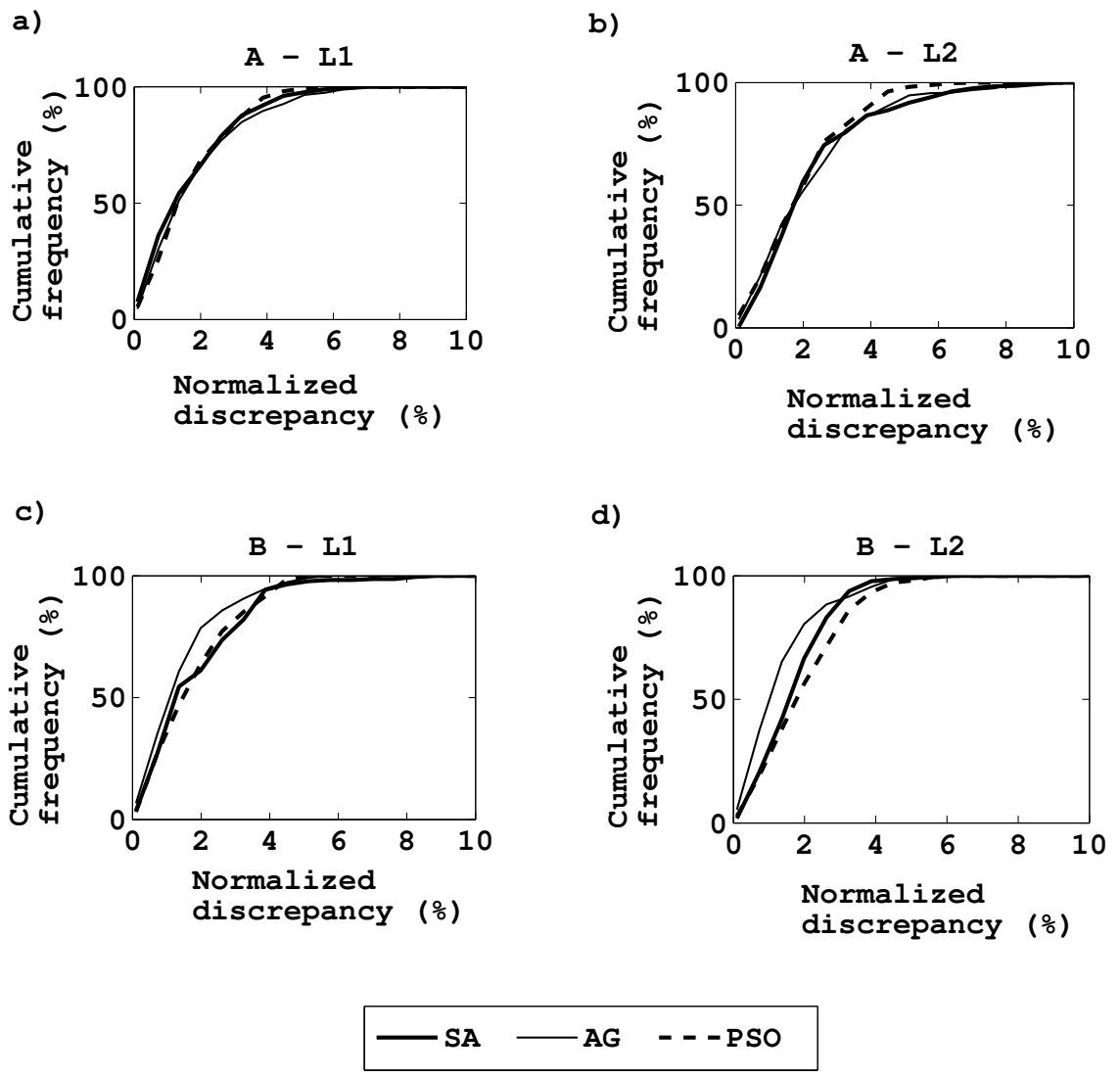


Figure 6

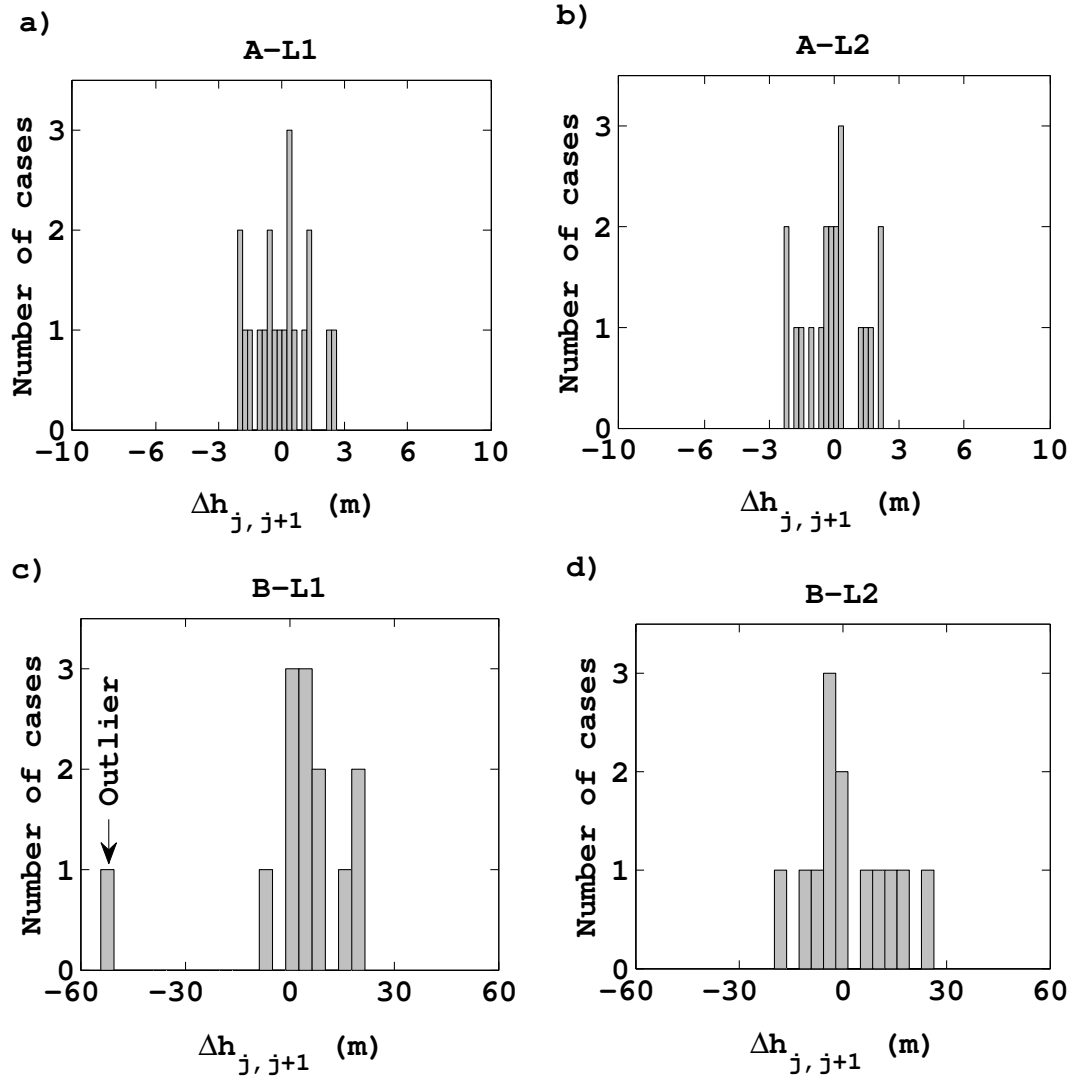


Figure 7

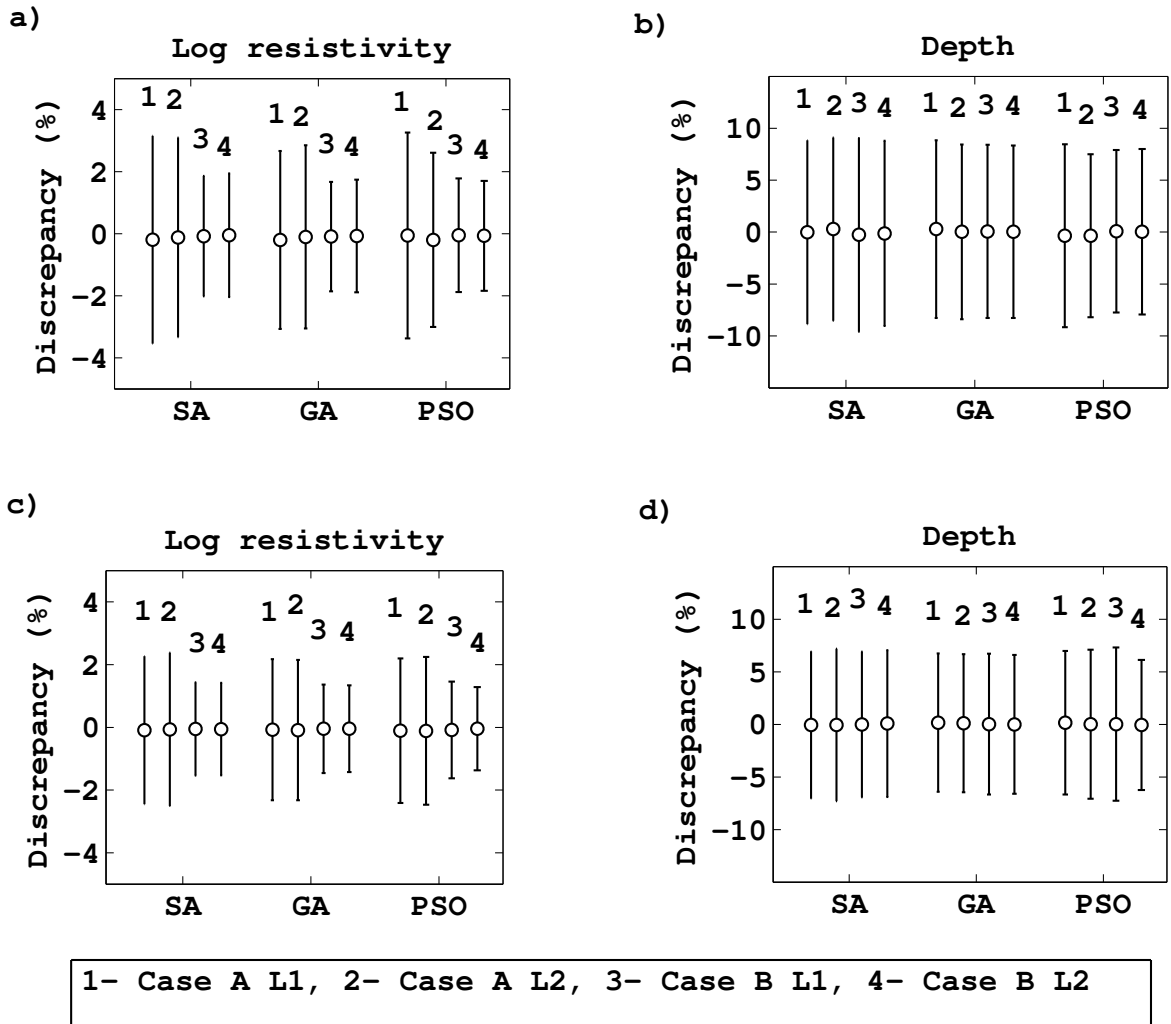
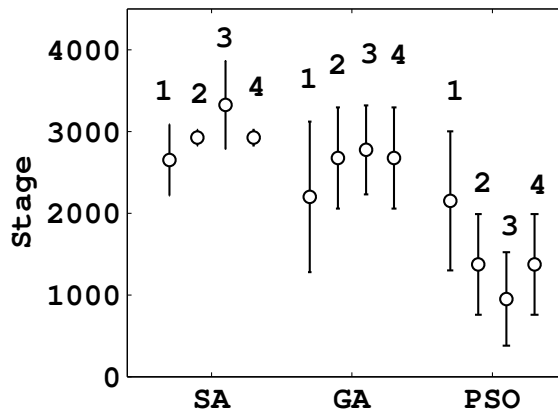
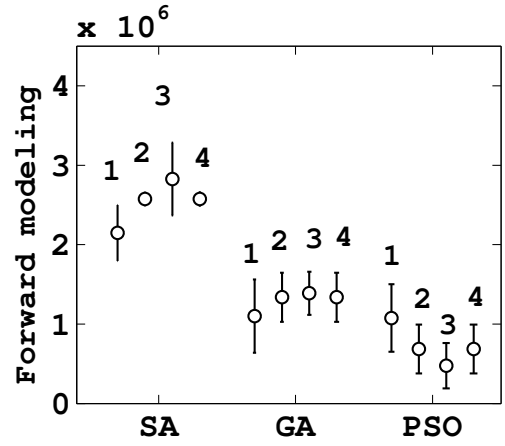


Figure 8

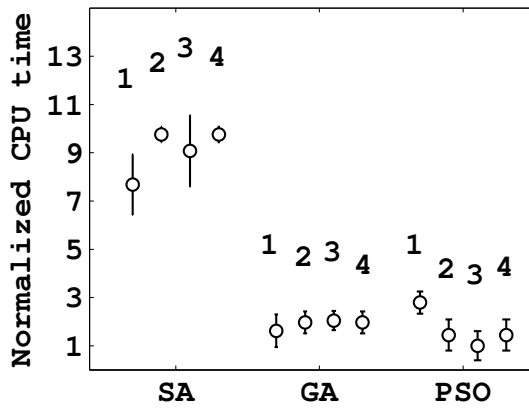
a)



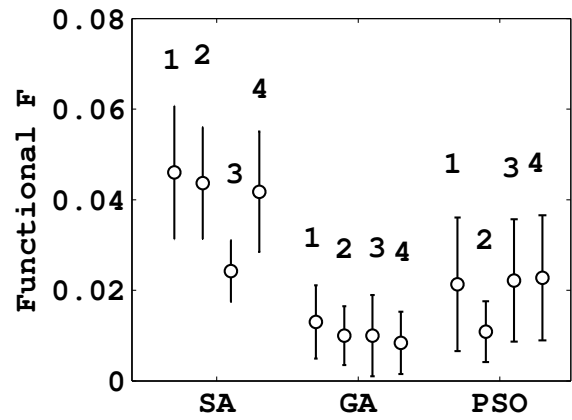
b)



c)



d)



1- Case A L1, 2- Case A L2, 3- Case B L1, 4- Case B L2

Figure 9

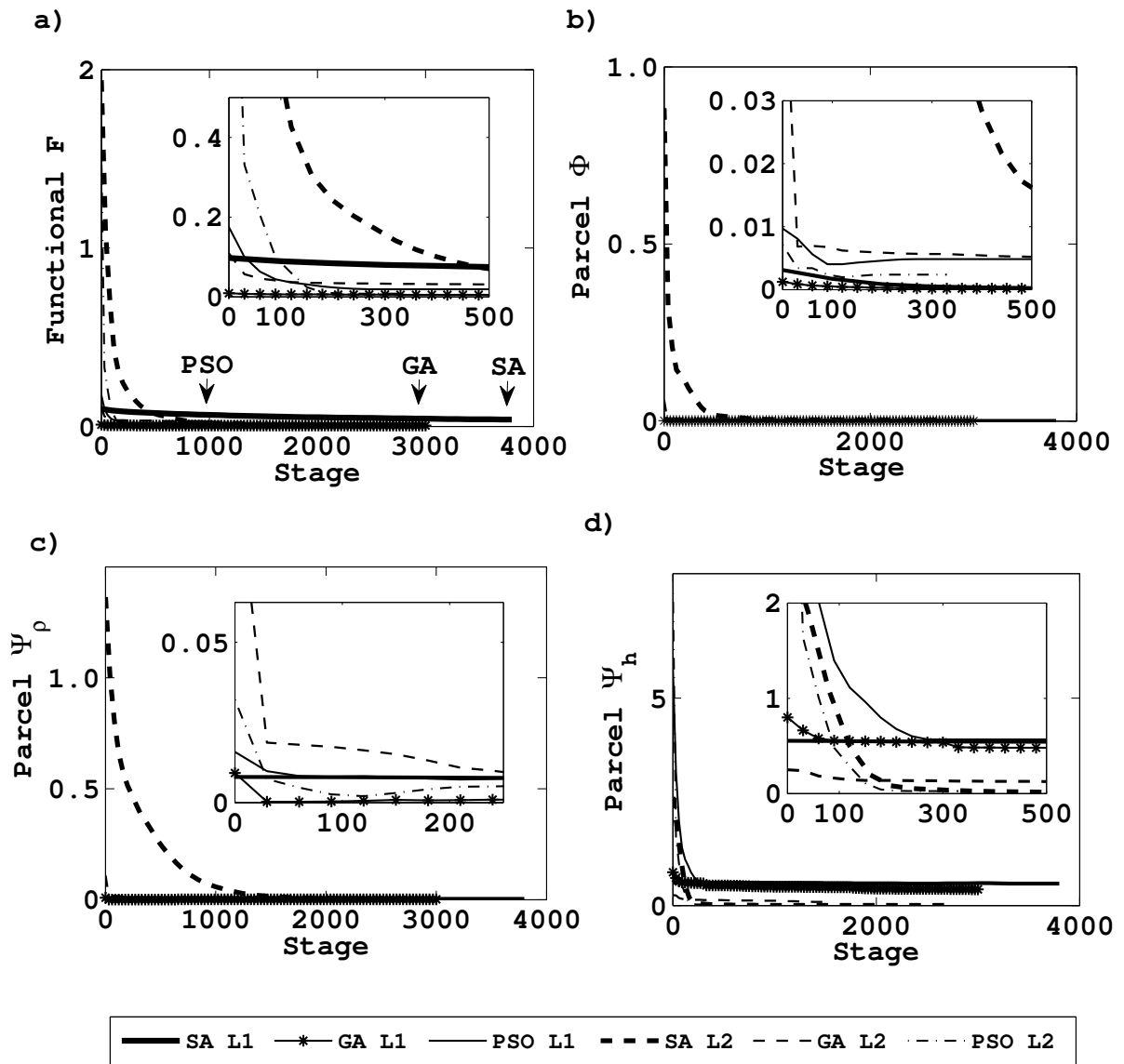


Figure 10

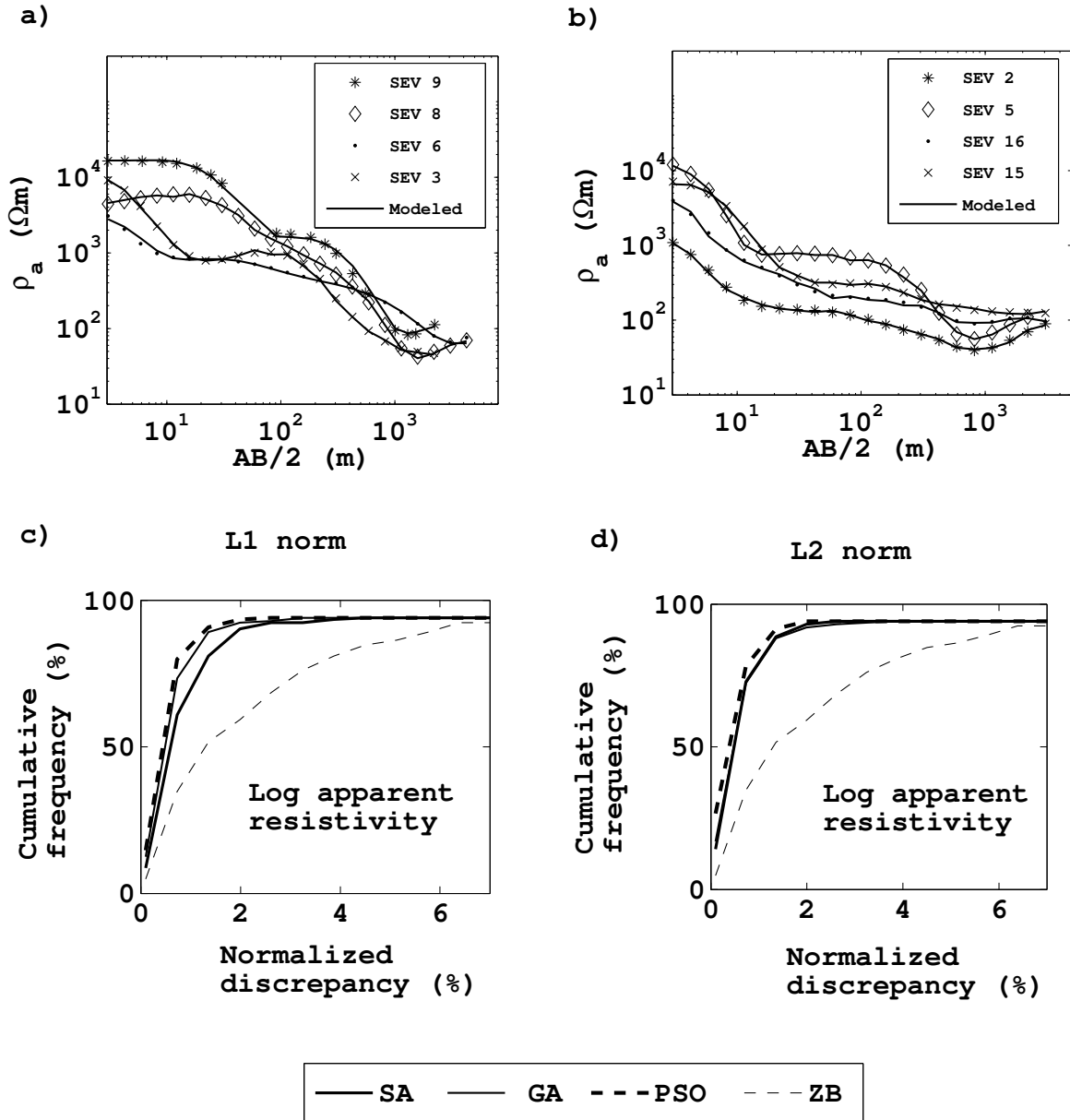


Figure 11

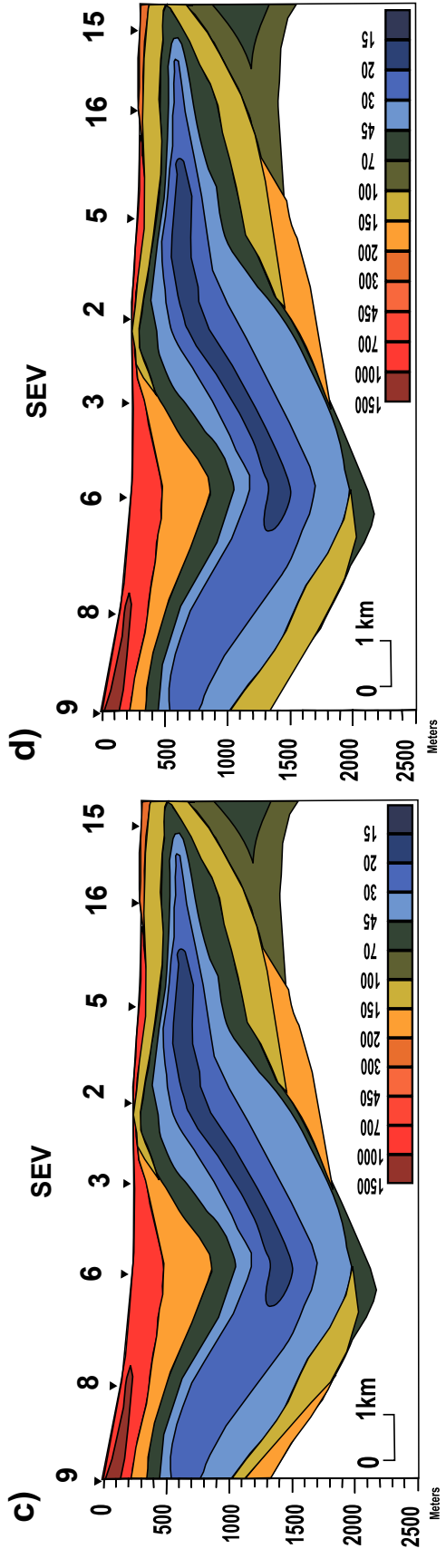
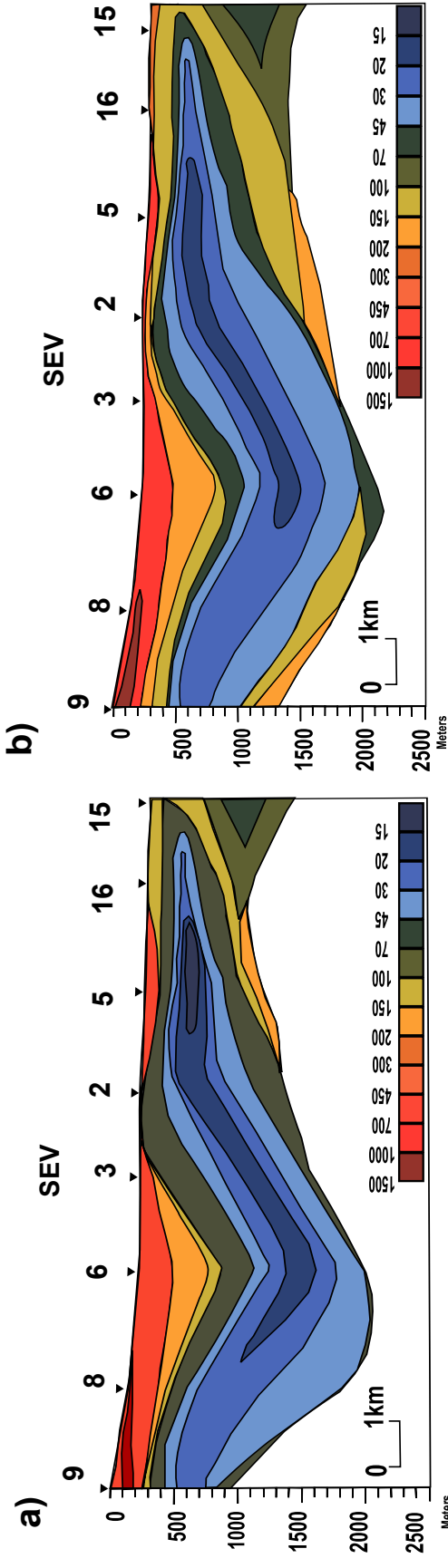


Figure 12

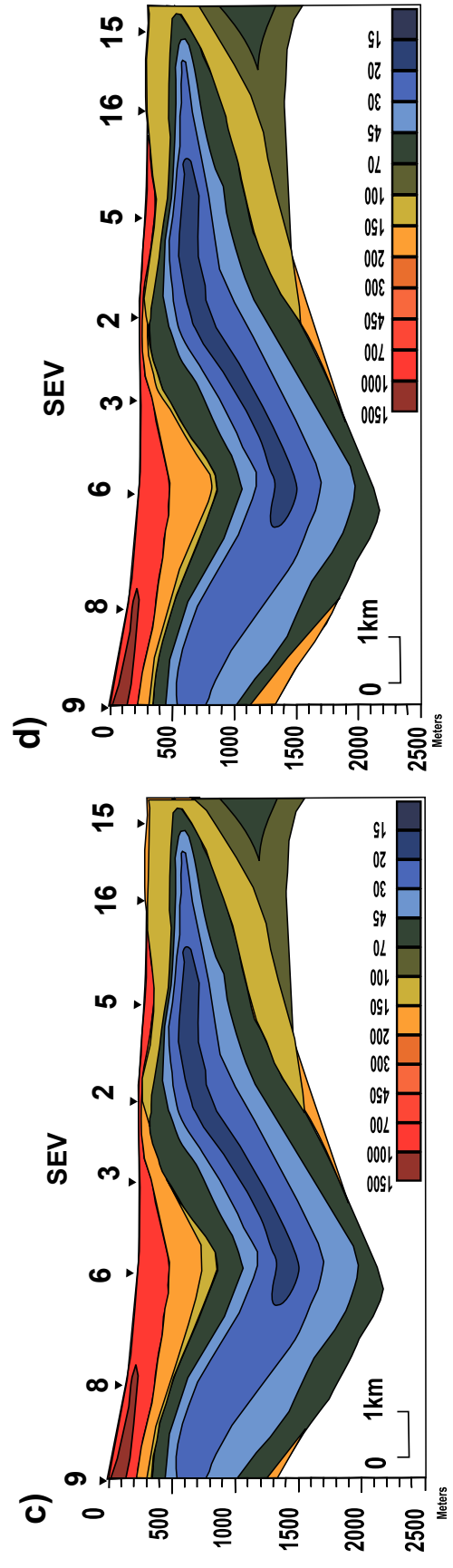
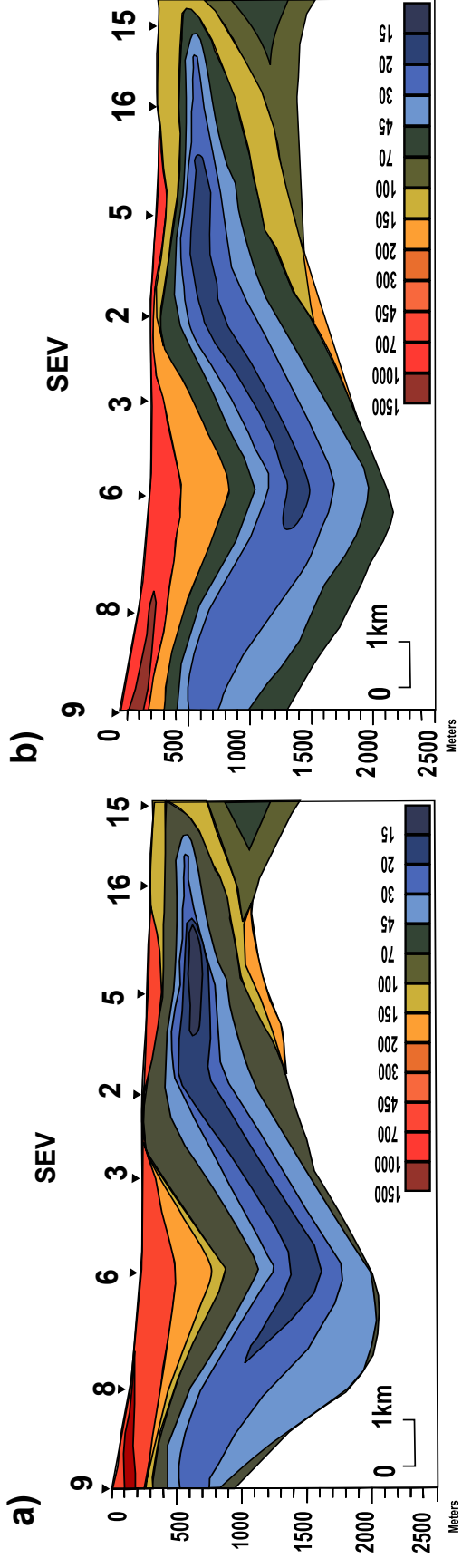


Figure 13

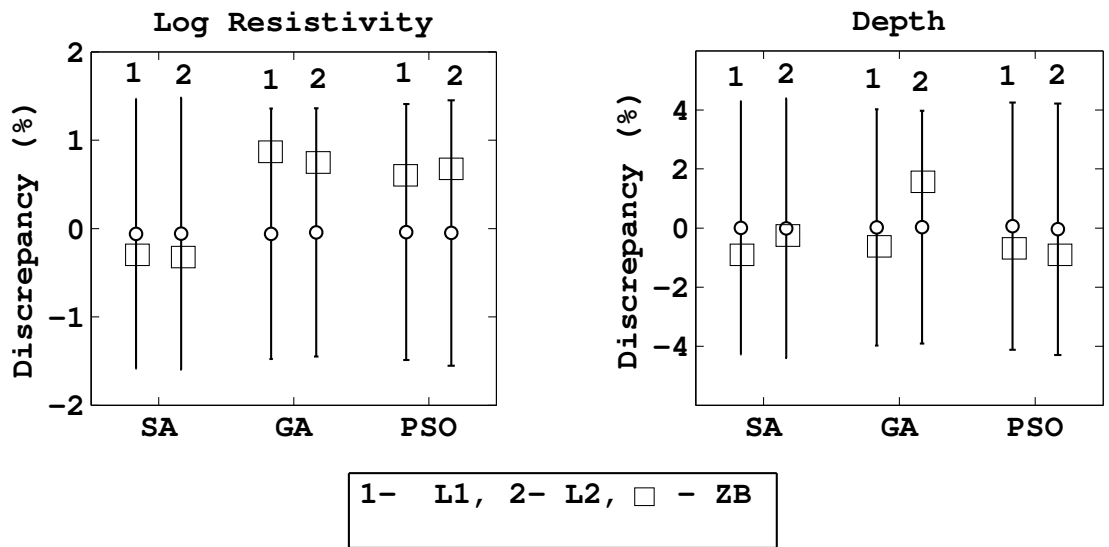


Figure 14

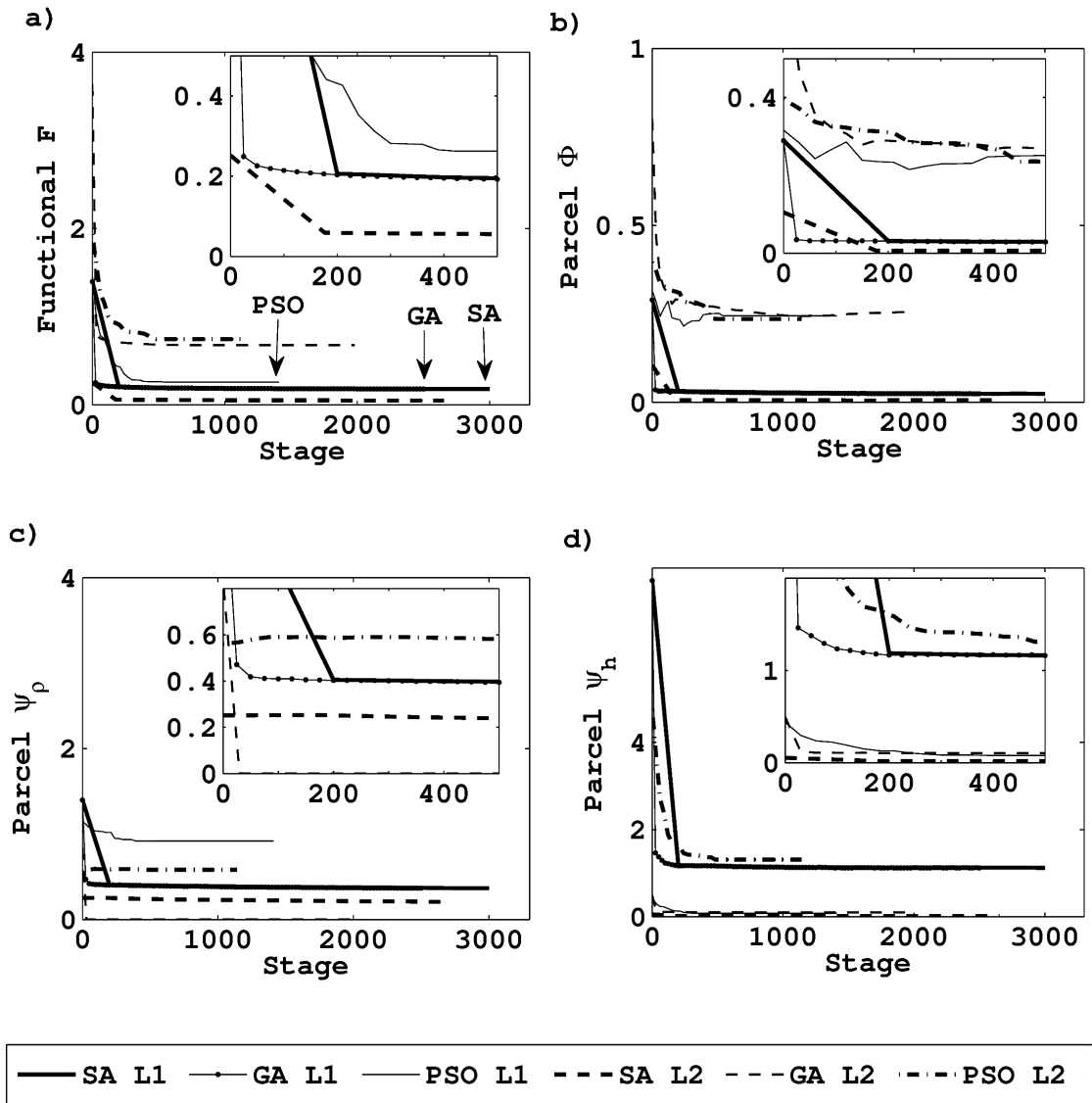


Figure 15

Model		Ratio to true <sup>(1)</sup> or preliminary estimates <sup>(2)</sup>					
		Lower bound			Upper bound		
		min	mean	max	min	mean	max
A <sup>(1)</sup>	resistivity	0.50	0.50	0.50	3.00	3.60	5.00
	layer depth	0.25	0.37	0.50	2.50	3.70	5.00
B <sup>(1)</sup>	resistivity	0.33	0.45	0.50	2.00	2.90	3.50
	layer depth	0.12	0.30	0.43	1.16	2.14	2.92
Field case <sup>(2)</sup>	resistivity	0.45	0.63	0.79	2.50	2.98	3.47
	layer depth	0.46	0.63	0.75	2.72	3.00	3.40

Table 1

---

## Capítulo 3

# **Manuscrito submetido: "Freedom to change constraints in a feedback inversion approach of 2D resistivity data using PSO"**

---

Manuscrito submetido Geophysics, de Qualis CAPES A1. Corresponde aos resultados obtidos com inversão em eletrorresistividade *2D* realizadas utilizando o algoritmo de otimização Global PSO. Uma abordagem interpretativa com uso e flexibilidade de diversos vínculos foi realizada em dados sintéticos e dados reais.

Nas próximas páginas segue o uma versão do manuscrito do artigo.

# Freedom to change constraints in a feedback inversion

## approach of 2D DC-resistivity data using PSO

Francisco M. Barboza<sup>\*‡</sup>, Walter E. Medeiros<sup>\*†</sup>, and Jerbeson M. Santana<sup>\*</sup>

*\*Programa de Pós-graduação em Geodinâmica e Geofísica.*

*†Departamento de Geofísica*

*Centro de Ciências Exatas e da Terra*

*Universidade Federal do Rio Grande do Norte – UFRN*

*59.072-970, Natal/RN, Brazil.*

*Phone: 55 84 3215 3794*

*‡ On leave from Universidade Federal do Acre – UFAC*

(December 5, 2017)

Running head: ***Feedback inversion using PSO***

### ABSTRACT

An inversion approach based on particle swarm optimization (PSO) is presented for the 2D direct current (DC)-resistivity data. Once the PSO algorithm is implemented, cost function modifications, either on changing constraints or data fitting criteria, can be easily performed, since that each term of the cost function is properly normalized in order to allow approximate invariance of the Lagrange multipliers. We explore several constraints on the log-resistivity variation: spatial continuity both in the  $\ell_1$  and  $\ell_2$  norms, including the case of constraining variation just in the horizontal direction, total variation, and sparsity constraints using both discrete cosine transform and Daubechies bases. In addition, we explore the minimum moment of inertia constraint, including the case of using the Earth surface as the target

axis, to impose concentration of either resistive or conductive materials along target axes. Equally important, from the stopping criteria of the PSO algorithm results not only the best solution but also a cluster of suboptimal quasi-solutions from which uncertainty analyses can be performed. As a result, the interpreter has freedom to perform a quantitative interpretation process based on a feedback trial-and-error inversion approach, in a similar manner he/she has when using a friendly forward modeling software, being capable of driving the solution to incorporate his/her conceptions about the geologic environment, besides appraising data fitting and stability of the obtained solutions. We present both synthetic and field data examples. In the first case we show that the interpreter might drive the interpretation process in a karst environment to image dissolution structures both above and beneath the water table. In the second case, we show how the interpreter might drive an interpretation process to optimize borehole location in fracture zones in crystalline rocks, aiming to estimate the fresh-rock depth and discriminate fractured/weathered rock from shallow conductive materials, like clay-soil.

**Keywords:** apparent resistivity, electrical/resistivity, inversion, nonlinear, optimization.

## INTRODUCTION

There are basically two manners of performing quantitative interpretation of geophysical data: using a trial-and-error modeling approach, based on flexible forward modeling softwares, or using inversion algorithms. The geophysical inverse problem is frequently formulated as an optimization problem where the solution is the minimum of a cost function involving two parcels: one demanding that observed and modeled data are fitted and the other imposing constraints on the Earth model parameters (Tikhonov and Arsenin, 1977).

When the interpreter changes from the first to the second interpretation manner, a lot of flexibility is lost when facing geological complexities because most of the available inversion algorithms offer a too limited set of constraints to test different solutions. In Barboza et al. (2017) we presented a quantitative inversion approach where ultimately we are trying to give back to the interpreter the lost flexibility. This inversion approach is based on the use of global optimization methods (GOMs), instead of the most commonly used local optimization methods, to solve the geophysical inverse problems.

In a local method, given a starting model, one tries to obtain a local minimum of the cost function based on an iterative process, where in each step the cost function is decreased until a stationary point - a local minimum - is attained (Gill et al., 1981). On the other hand, GOMs are based on optimization approaches usually mimicking an adaptation strategy found in Nature, which ultimately might converge to the global minimum, as simulated annealing (SA) (Kirkpatrick et al., 1983), genetic algorithms (GA) (Goldberg, 1989), and particle swarm optimization (PSO) (Kennedy et al., 2001). SA (e.g. Sen and Stoffa, 1995; Rucker and Ferré, 2005; Santos et al., 2006; Pei et al., 2007; Wang et al., 2012; Biswas and Sharma, 2014), GA (e.g. Sen and Stoffa, 1995; Başokur et al., 2007; Jha et al., 2008; Morgan et al.,

2012; Attwa et al., 2014), and PSO (e.g. Shaw and Srivastava, 2007; Martínez et al., 2010; Fernández Martínez et al., 2012; Tronicke et al., 2012) are GOMs increasingly in use in geophysics.

Compared to local methods, GOMs require much higher computational cost because huge numbers of cost function evaluation might be necessary (Sen and Stoffa, 1995), each evaluation requiring a forward modeling. However, for geophysical inverse problems where forward modeling is inexpensive it may be worth it because GOMs offer high flexibility in changing the cost function. That was the point we started to explore in Barboza et al. (2017). In that study our main objective was to realize a comparison of performance among SA, GA, and PSO algorithms, including robustness to changes in the cost function. Because a comparison of this nature requires a huge amount of forward modeling, we choose a very inexpensive inverse problem: the 1.5 D direct current (DC)-resistivity inverse problem, where the forward modeling is done using the 1D layer cake model but a set of soundings is jointly inverted imposing lateral continuity constraints on the layers parameters (e.g. Gyulai and Ormos, 1999; Auken et al., 2005). Nevertheless, because of the model simplicity it was not possible to explore in deep the versatility of this inversion approach. This is the objective of the present study, where we treat the 2D DC-resistivity inverse problem using PSO. In the referred computational performance comparison, we verified that PSO and GA are very robust to changes in the cost function and more computationally efficient than SA. In addition, PSO was comparatively easier to implement than GA, as consequence of the underlying simplicity of the associated equations.

In the following section we summarize the 2D DC-resistivity inverse problem. Then we present both synthetic and field data examples where we show that the interpreter can perform a kind of trial-and-error inversion approach, where he/she performs an inversion

process by phases. The solutions of the initial phases are used in a feedback manner to improve the solutions obtained in posterior phases. In other words, the interpreter uses the initial solutions to choose or design new constraints in different partitions of the interpretation mesh so that he/she drives the inversion process to obtain solutions which are consistent with his/her geological conceptions about the study case.

To show how flexible a PSO-based inversion algorithm can be, we explore several types of constraints: spatial continuity (e.g. Tikhonov and Arsenin, 1977; Constable et al., 1987) both in the  $\ell_1$  and  $\ell_2$  norms, including the particular case of constraining the physical property to vary just in the horizontal direction; total variation (e.g. Rudin et al., 1992; Portnaguine and Zhdanov, 1999); sparsity (e.g. Loris et al., 2007; Jafarpour et al., 2009; Simons et al., 2011; Charl  ty et al., 2013) using both discrete cosine transform and Daubechies bases of order 4 (Mallat, 2008); and minimum moment of inertia (e.g. Guillen and Menichetti, 1984; Ajo-Franklin et al., 2007) constraints, including the particular case of using the Earth surface as the target axis (Barbosa et al., 1999). In order to make reading easy for explorationist geophysicists, that might be interested just in the interpretation approach, almost all technical details of the inverse problem, including the mathematical formulation of the constraints and the description of the PSO algorithm, are shifted to appendices.

## 2D DC-RESISTIVITY INVERSE PROBLEM

Suppose that an electrical resistivity tomography (ERT) experiment is done along a direction  $x$  in the Earth surface, using a given electrode array as, for example, the Schlumberger array. The apparent resistivity measurements can be arranged as the  $N_{obs}$ -size vector  $\mathbf{d}^{obs}$ , where  $N_{obs}$  is the total number of measurements composing the ERT. We assume that the ERT image can be interpreted under the hypothesis that the subsurface resistivity distribu-

tion  $\rho$  varies only with the depth  $z$  and with the profile direction  $x$ , inside a priori specified rectangular region  $\Gamma$ . In this region the function  $\rho(z, x)$  is discretized in a mesh with  $N_z$  cells along  $z$  and  $N_x$  cells along  $x$  (Figure 1). A generic cell and its resistivity value may be identified either by the pair  $(i, j)$  ( $i = 1, 2, \dots, N_z; j = 1, 2, \dots, N_x$ ) or by the cell counting number  $k = i + (j - 1)N_z$  ( $k = 1, 2, \dots, N_x N_z$ ). The subsurface resistivity can then be arranged in the  $N_x N_z$ -size vector  $\mathbf{m} = \mathbf{m}(k)$ .

After solving numerically the Poisson equation describing the DC-resistivity forward modeling problem in the mesh (e.g. Dey and Morrison, 1979), it is possible to obtain the calculated apparent resistivity data  $\mathbf{d}^{cal}(\mathbf{m})$ . This vector might reproduce approximately the observed data vector  $\mathbf{d}^{obs}$ , that is

$$\mathbf{d}^{obs} = \mathbf{d}^{cal}(\mathbf{m}) + \boldsymbol{\eta}, \quad (1)$$

where  $\boldsymbol{\eta}$  is the vector of associated discrepancies. Estimating  $\mathbf{m}$  based just on the criterion of minimizing a norm of  $\boldsymbol{\eta}$  is an ill-posed problem because this solution is unstable to small perturbations in  $\mathbf{d}^{obs}$ . To obtain stable estimates of  $\mathbf{m}$ , we solve the constrained inverse problem of minimizing (in relation to  $\mathbf{m}$ ) the cost function  $\mathcal{L}$  given by

$$\mathcal{L}[\mathbf{d}^{cal}(\mathbf{m}), \mathbf{d}^{obs}; \mathbf{m}] = \Phi_a[\mathbf{d}^{cal}(\mathbf{m}), \mathbf{d}^{obs}] + \mathcal{R}(\mathbf{m}), \quad (2)$$

for  $\mathbf{m} \in \Omega$ , a search-space imposing box constraints for each element of  $\mathbf{m}$ . In the above equation, the first term  $\Phi_a$  of  $\mathcal{L}$  demands that the observed data  $\mathbf{d}^{obs}$  be fitted by the

modeled data  $\mathbf{d}^{cal}(\mathbf{m})$  in the least-squares sense, that is

$$\Phi_a = \frac{1}{N_{obs}\sigma_\eta^2} \left\| \log(\mathbf{d}^{cal}(\mathbf{m})) - \log(\mathbf{d}^{obs}) \right\|_2^2, \quad (3)$$

where  $\sigma_\eta^2$  is an estimate of the variance of the discrepancies between observed and modeled log-apparent resistivities. On the other hand, the second term  $\mathcal{R}(\mathbf{m})$  of  $\mathcal{L}$  (equation 2) imposes constraints on the subsurface resistivities in order to stabilize the inverse problem solution. To take the maximum benefits from using GOMs we use the following general approach: a) the subsurface interpretation region  $\Gamma$  might be divided (Figure 1) into  $P$  non-overlapping partitions  $\Gamma_p$  ( $p = 1, 2, \dots, P$ ); b) in different partitions different constraints might be employed, and finally c) in a partition  $\Gamma_p$  more than one constraint might be applied. As a result  $\mathcal{R}(\mathbf{m})$  has the general form

$$\mathcal{R}(\mathbf{m}) = \mathcal{R}[\mathbf{m}; P, L(p); \mu_{p\ell}] = \sum_{p=1}^P \sum_{\ell=1}^{L(p)} \mu_{p\ell} f_{p\ell} \mathcal{R}_{p\ell}, \quad (4)$$

where  $L(p)$  is the number of constraints used in  $\Gamma_p$ ,  $\mathcal{R}_{p\ell}$  is the  $\ell$ -th constraint in  $\Gamma_p$ , being  $\mu_{p\ell}$  and  $f_{p\ell}$  the associated Lagrange multiplier and normalization factor, respectively. The general form of the normalization factor is

$$f_{p\ell} = \frac{1}{N_{p\ell}\sigma_{\mathcal{R}_{p\ell}}}, \quad (5)$$

where  $N_{p\ell}$  is the number of parcels composing  $\mathcal{R}_{p\ell}$  and  $\sigma_{\mathcal{R}_{p\ell}}$  is an estimate of the discrepancies of these parcels.

In the inversion examples to be presented, using both synthetic and field data, we use several constraints: a) spatial continuity constraints (e.g. Tikhonov and Arsenin, 1977;

Constable et al., 1987) both in the  $\ell_1$  and  $\ell_2$  norms, named as  $\mathcal{R}_1$  and  $\mathcal{R}_2$ , and a particular case of  $\mathcal{R}_1$  that is constraining just the spatial variation along the horizontal  $x$  (named as  $\mathcal{R}_1^x$ ); b) total variation constraint (TV) (e.g. Rudin et al., 1992; Portniaguine and Zhdanov, 1999), named as  $\mathcal{R}_{TV}$ ; c) sparsity constraint (e.g. Loris et al., 2007; Jafarpour et al., 2009; Simons et al., 2011; Charléty et al., 2013) using both the Discrete Cosine Transform (DCT) and Daubechies bases of order 4 (Mallat, 2008), which are named as  $\mathcal{R}_{DCT}$  and  $\mathcal{R}_{DWT}$ , respectively; and finally d) minimum moment of inertia constraint (e.g. Guillen and Menichetti, 1984; Ajo-Franklin et al., 2007), named as  $\mathcal{R}_M$ , and a particular case of  $\mathcal{R}_M$  that is using as target axis the Earth surface (Barbosa et al., 1999). For completeness, a summary of the mathematical formulation of all these constraints is presented in Appendix A, besides the detailed expressions for each one of the normalization factors.

We solve the inverse problem defined by equation 2 using the PSO method (e.g. Kennedy and Eberhart, 1995; Shaw and Srivastava, 2007; Martínez et al., 2010; Fernández Martínez et al., 2012; Tronicke et al., 2012). A summary of the PSO algorithm we use is presented in Appendix B. This PSO algorithm is basically the same one described in Barboza et al. (2017). So, for the most part, the text contained in the Appendix B is an adaptation of the text presented in Barboza et al. (2017) to the nomenclature of the present 2D DC-resistivity inverse problem. However, we stress that two key modifications were done, both ones described in detail in Appendix B. These modifications are oriented to perform a better sorting of the starting values of the resistivities in the cells of the mesh, allowing a faster convergence of the optimization process.

## APPLICATION TO SYNTHETIC DATA

Geophysical characterization of shallow karst heterogeneities is a very challenging problem and the choice of adequate geophysical methods remains site related (Carrière et al., 2013). For example, when the overburden is composed by resistive materials, ground penetrating radar (GPR) allow very good imaging of karst structures (e.g. Fernandes et al., 2015). However, in the presence of conductive overburden, ERT is commonly the method of choice (Roth et al., 2002) and has been increasingly used to image complex heterogeneities in karst or similar environments (e.g. Nyquist et al., 2007; Ezersky, 2008; Gutiérrez et al., 2009; Valois et al., 2011; Zhu et al., 2011). Nonetheless, interpreting ERT data in karst environment presents several difficulties as, for example, the fact that the same structure might appear as either resistive or conductive, depending on the water presence (e.g. Smith, 1986; Loke et al., 2013). We use this challenging environment to demonstrate the high flexibility that a PSO-based inversion algorithm can give to the interpreter.

Figure 2 shows a photograph of a cliff in a limestone quarry in Rio Grande do Norte state, Brazil. The limestone is part of the Jandaíra Formation, Potiguar basin (Araripe and Feijó, 1994), which is a carbonate platform formed during a sea-level transgression in the late Cretaceous, associated with the South Atlantic opening after the breakup of Pangea. The cliff wall exposes several karst structures, including dissolution voids along horizontal bedding, which might be filled with unconsolidated sediments. In addition, subvertical fractures might connect the horizontal dissolution voids (Figure 2).

Inspired by the dissolution structures present in the cliff wall of the limestone quarry (Figure 2), we design the two synthetic models shown in Figures 3a and 4a, from now on named as Karst 1 and Karst 2, respectively. Both models present anomalous bodies of

tabular shape, in some cases connected by vertical conduits. In Karst 1 all material filling the structures are admitted to contain water, so that all anomalous bodies are conductive in relation to the surround unaltered rock (Figure 3a). On the other hand, in Karst 2 the water table is 15 m deep, so that the anomalous bodies above it are resistive in relation to the unaltered rock (Figure 4a). Note also in Karst 2 that even the unaltered rock is more resistive above the water table. To complete the set of synthetic models, we add the Dike model shown in Figure 5a, which contains a dipping dike and composes also a very difficulty situation for ERT interpretation.

To calculate the Schlumberger array soundings curves for the shown synthetic models, we use the the finite-difference approach of Dey and Morrison (1979). The useful part of the modeling mesh (Figure 1) is composed of 80 cells in the  $x$  direction by 15 cells in the  $z$  direction. The mesh is uniform along  $x$ , with mesh size equal to 5 m, but is nonuniform along  $z$ , being the available depths equal to 0, 1, 2, 4, 7, 10, 15, 20, 30, 40, 50, 60, 80, 100, 120, and 160 m. Besides the useful portion, the mesh contains additional regions to simulate infinitely distant boundaries. The calculated apparent resistivity data is arranged in the vector  $\mathbf{d}^{cal}(\mathbf{m})$ . Figures 3b, 4b, and 5b show the apparent resistivity soundings, resulting in the apparent resistivity sections shown in Figures 3c, 4c, and 5c for the Karst 1, Karst 2, and Dike models, respectively. Note that in all models there is a thin soil of varying resistivity. In each case, it were generated 21 equally spaced resistivity soundings. To verify the stability of the inversion estimates in relation to small discrepancies in the synthetic data, we add to all apparent resistivity data one realization of pseudorandom Gaussian noise with zero mean and standard deviation equal to 2.5% of the modeled value. These noisy data were not altered and we refer to them as observations.

In any of the three models, one can hardly infer the main features of the anomalous bod-

ies based just on the qualitative interpretation of the apparent resistivity sections (Figures 3c, 4c, and 5c). So, a kind of trial-and-error quantitative interpretation would be mandatory. We show that using a PSO algorithm it is possible to perform a quantitative inversion approach where preliminary inversion results might be used to test new constraints in a feedback manner. In all cases we admit that the interpreter has a very good knowledge of the geologic environment so that he/she can drive the quantitative inversion phases to investigate his/her a priori conceptions about the anomalous bodies by using different constraints. The mesh used in all inversion examples (including the field data examples) has the same available depths, above described for the forward modeling mesh, but has mesh-size along  $x$  equal to 10 m. As a result, there are 560 cells in the interpretation model.

### **Karst 1 model**

Let us begin with the Karst 1 model. Figures 6a and 6b show estimates obtained with the spatial continuity constraints (equation 6), named as SC- $\ell_1$  and SC- $\ell_2$ , using the  $\ell_1$  and  $\ell_2$  norms, respectively (for mathematical details about the constraints, please see Appendix A). Although representing a tremendous advance as compared to the apparent resistivity section (Figure 3c), the classic smoothness constraint produces just a very blurred image of the anomalous bodies (Figure 6b). On the other hand, the SC- $\ell_1$  image appears to better focus the shape of the bodies (Figure 6a). However, it is not clear yet where are the top and bottom boundaries of the bodies and also, if the dissolution along the horizontal bedding around 30-35 m depth is continuous or not.

To investigate these open questions, the interpreter might test constraints favoring more sharp discontinuities as, for example, total variation (TV) (equation 12) and sparsity con-

straints (equation 14) based on discrete cosine transform (DCT) or discrete wavelet transform (DWT). Figures 6c, 6d, and 6e show estimates obtained with TV, DCT, and DWT (Daubechies bases of order 4) constraints, respectively. With these last three estimates, in particular with the DWT one (Figure 6e), the above described open questions about the anomalous bodies might be considered as answered questions, maybe with the exception of the doubt concerning the lateral continuity of the horizontal dissolution around 30-35 m depth.

To obtain a conclusive answer to this question, the interpreter might test constraints producing even more sharp discontinuities as, for example, by imposing that the moment of inertia of the conductive distributions around certain axes be minimized (MMI constraint given by equation 16). Now the interpreter must define a partition to the mesh (Figure 6f) where seven different subregions are specified, accordingly to the target axes associated with the MMI constraints. The target axes A, B, and C to concentrate the conductive material are inferred from Figures 6d and 6e. Note that the B axis is vertical thus favoring the existence of a vertical conduit connecting the shallow and deep horizontal dissolutions. We stress that the shown three axes are just starting guess and that the positions of these axes are updated during the optimization process. So, we choose intentionally A, B, and C axes not coinciding with the best spatial positions.

The final estimates are shown in Figures 6g and 6h where DCT and DWT constraints were respectively combined (or jointly applied) with MMI in the different partitions ( $\Gamma_2$  to  $\Gamma_7$ ) to concentrate conductive materials around axes A, B, and C. Note that both DCT and DWT constraints are used in the whole mesh, except in  $\Gamma_1$  (soil) where no constraint is applied. There are two reasons to use no constraints in  $\Gamma_1$ : 1) the soil resistivity varies a lot (Figure 3b) and 2) to allow a better data fitting. As a result, seven different set

of constraints are employed. From the image shown in Figure 6g all questions posed by the interpreter are answered; indeed this figure reproduces the main features of the true resistivity distribution (Figure 3a).

Each image shown in Figure 6 is a best PSO solution. In addition, for each one, the stopping criteria of the PSO algorithm (for details please see Appendix B) provides also a set of 200 suboptimal quasi-solutions, from which an uncertainty analysis can be performed. We estimate the confidence region around the best solution in the following manner. For each inversion case, the best value for the log-resistivity of a cell is taken as the reference, in relation to which the respective set of 200 quasi-optimal estimates can be expressed as percentage discrepancies. The statistics over the whole mesh are then be grouped as a single pair of mean percentage discrepancy and its associated standard deviation, as shown in Figure 7a. From the analysis of this figure, we conclude that all the seven solutions are stable because each mean percentage discrepancy is approximately zero with standard deviation smaller than 1.5%. In addition, all the seven solutions shown in Figure 6 honor the log-apparent resistivity observations because 90% of these observations are reproduced with an error up to 3% (Figure 7b). In this latter figure note that the best data fitting is provided by the solution combining DCT and MMI constraints (Figure 6g). Thus, from the interpreter view point, this is the best solution because, besides providing the best data fitting, it incorporates his/her a priori conceptions about the geologic environment.

## **Karst 2 model**

Now we treat the Karst 2 model (Figure 4). In the following results, it is admitted that the interpreter knows the water table depth. We begin again with the  $SC-\ell_1$  (Figure 8a) and

SC- $\ell_2$  (Figure 8b) estimates. Both estimates produce quite surprising good images of the resistive anomalous bodies above the water table. However, for the conductive anomalous bodies beneath the water table, both images are quite different from the true model (Figure 4a). The main reason is the fact that the portions of the deeper conductive bodies which are located below the shallow resistive bodies are not well detected. For example, by analysing Figures 8a and 8b one might conclude that the horizontal dissolution around 30-35 m depth has no continuity around both positions 140 m and 380 m. Note that the latter conclusion would be right but that the first one would be wrong. In addition, as well as in Karst 1 model, it is not clear yet where are the top and bottom boundaries of the deep conductive bodies. Let us then admit that the interpreter is not satisfied with these preliminary inversion results, in particular with the first impression that the deep horizontal dissolution has no continuity around position 140 m. He/she decided then to investigate carefully these open questions.

Similarly to Karst 1 model, the interpreter decides to test constraints favoring more sharp discontinuities, thus obtaining the estimates shown in Figures 8c, 8d, and 8e by using TV, DCT, and DWT constraints, respectively. With the two latter estimates, the above described open questions about the anomalous bodies might be considered as answered questions, except for the doubt concerning the lateral continuity of the deep horizontal dissolution around position 140 m that clearly remains open.

To obtain a conclusive answer to this question, the interpreter might test constraints imposing MMI around certain axes. The target axes A and B are inferred from Figures 8d and 8e. Then, the interpreter might divide the mesh into the two partitions shown in Figure 8f. However, in a contrasting manner to the Karst 1 case, the interpreter must impose now concentration of resistive material above the water table. So the target axes A

and B are used to concentrate resistive and conductive materials in  $\Gamma_1$  and  $\Gamma_2$ , respectively. Also in contrast with the Karst 1 case, no vertical target axis was employed, thus avoiding to favour the existence of a conduit connecting the shallow and deep horizontal dissolutions, as a manner of minimizing the bias toward favouring the existence of the deep horizontal dissolution around position 140 m.

The final estimates are shown in Figures 8g and 8h where respectively DCT and DWT constraints are used in the whole mesh whereas MMI is employed separately in  $\Gamma_1$  and  $\Gamma_2$ , according to the target axes and concentration criteria above described. After these two images, the interpreter might be now more confident about the limits and continuity of the dissolution structures. Indeed, both estimates reproduce quite well the true resistivity distribution (Figure 4a). Also as in Karst 1 case, all the seven solutions are stable (Figure 9a) and honor the observations (Figure 9b). Again, the best data fitting is provided by the solution combining DCT and MMI constraints (Figure 8g) and, similarly to the Karst 1 case, it provides the best solution from the interpreter view point.

## Dike model

We begin with the SC- $\ell_1$  (Figure 10a), TV (Figure 10b), DCT (Figure 10c), and DWT (Figure 10d) constraints. In this case, the solution obtained with the SC- $\ell_2$  constraint (not shown) is an even more blurred image than Figure 10a. Analysing the four images (Figures 10a - 10d), the interpreter might infer: 1) that the anomalous body presents asymmetry in relation to the vertical line around position 200 m and 2) perhaps it has a continuity below 60 m depth, the latter hypothesis being derived particularly from Figure 10d. In addition, let us admit that the interpreter has the a priori geological information that in the studied

region dipping dikes might occur. He/she decides then to investigate this possibility. To this end, the target axes A (Figure 10d) is proposed to concentrate conductive materials. We stress that both the position and dip of axis A do not coincide with the respective true values (Figure 5a).

Figure 10e shows the obtained inversion result using just the MMI constraint in the whole mesh. The hypothesis of a dipping dike is now very reasonable. In addition, the interpreter verified that this solution is as stable as any of the first four solutions (Figure 10a) and offers similar or even better data fitting (Figure 10b). So, he/she decides to make a step further, dividing the mesh into three partitions and redefining the target axis (Figure 10f), in the latter case using the image 10e. The final estimates are shown in Figures 10g and 10h where  $SC-\ell_1$  (just in  $x$  direction) and DCT constraints are respectively employed in the whole mesh, except in  $\Gamma_1$ , besides the MMI constraint in  $\Gamma_3$  to concentrate conductive material around axis B (please see the Appendix B to understand in detail the reason of the image improvement obtained in Figures 10g and 10h in relation to the Figure 10e; basically, the search space  $\Omega$  used in the PSO algorithm is refined). In  $\Gamma_1$  (soil) no constraint is applied for the same reasons as in Karst 1 model. The two final solutions are also stable (Figure 11a) and honor the observations (Figure 11c). As in Karst 1 and 2 models, the best data fitting is provided by the solution combining DCT and MMI constraints (Figure 10h). As a result, this solution is again the best solution for the interpreter because it provides the best data fitting and incorporates his/her a priori conceptions about the geologic environment.

## APPLICATION TO FIELD DATA

In a large region of semi-arid climate in Northeast Brazil occur crystalline rocks. As a result, low rainfall rate and unfavorable groundwater storage are combined, turning water

supply for humans and animals into a severe problem, particularly in rural areas. In general, the hydrogeologic targets to locate boreholes are narrow zones containing rocks which are intensively fractured and/or altered by weathering. These zones are usually associated with faults (or major fractures) that might control structurally the course of small intermittent creeks, thus offering relatively better conditions to groundwater storage and recharge. Usually the boreholes are located using just surface geology criteria. However, quite contrasting pumping rates might result from boreholes located in similar surface geologic conditions. To investigate if geophysics could add discriminating criteria in this situation, a DC-resistivity study was done in a rural area in Bahia state, NE Brazil, where contrasting pumping results from boreholes were obtained (Medeiros, 1987; Medeiros and Lima, 1990). The survey area is composed mainly by gneiss.

In this context, it were obtained the two apparent resistivity datasets shown in Figures 12 and 13 using the Schlumberger array. From now we refer to them as Field 1 and Field 2 cases, respectively. Each dataset was measured along a traverse composed by 21 equally spaced stations, with distance between stations equal to 20 m, and in each station, five apparent resistivity values were measured ( $AB/2 = 5, 10, 20, 50, \text{ and } 100 \text{ m}$ ), resulting in 105 observations. The two traverses cross the course of the same creek in two different places: around positions 220 m and 240 m in Figures 12b and 13b, respectively, in each case being the traverse direction perpendicular to the local creek direction. The pre-existent boreholes were located just near the creek margins in both traverses. The borehole in the Field 1 traverse was drilled up to the depth of 40 m and gives a pumping rate of  $23.29 \text{ m}^3/h$ . On the other hand, the borehole in the Field 2 traverse was drilled up to the depth of 48 m but produces just  $2.16 \text{ m}^3/h$ . 2D modeling and inversion is a suitable approach for the shown datasets because of the fault control of the favorable zones and the fact

that the survey area has flat topography. An interpretation of these datasets based on a trial-and-error forward modeling approach is presented in Medeiros and Lima (1990).

The favorable zones might appear in apparent resistivity sections as relatively large and deep conductive anomalies, like the anomaly seen between positions 200 m and 300 m in Figure 12b. From the viewpoint of quantitative interpretation, estimating the fresh rock depth and discriminating the fractured and/or weathered rock from the shallow conductive materials (like clay-soil) are the main objectives. Note that both objectives might constitute difficult tasks because the contacts might be transitionals in both cases.

The inversion results obtained in Field 1 case using  $SC-\ell_1$ ,  $SC-\ell_2$ , TV, DCT, and DWT constraints are shown in Figures 14a to 14e, respectively. In each case, the constraint is used in the whole mesh. The fact that the  $SC-\ell_2$  image (Figure 14b) is very similar to the other four images ( $SC-\ell_1$ , TV, DCT, and DWT), all of them favoring more sharp discontinuities, is a clear indication that the contacts are indeed transitionals. In particular, when  $SC-\ell_1$  and  $SC-\ell_2$  inversion results almost coincide, the interpreter can infer that no abrupt discontinuity exist (Barboza et al., 2017). Nonetheless the transitional nature, note however that the area associated to the union of cells presenting resistivity estimates around 100 Ohm.m (from light blue to green colors in the images) is large; the value of 100 Ohm.m is a good indication that the rock is intensively fractured and/or altered by weathering. Thus, we can conclude that, along the traverse, the most favorable location for a borehole is near the positions 210 - 220 m, that is, as close as possible to the creek margin. Note that a fault border (near position 200 m) appear to control the creek course, so the borehole location was very lucky in this case. A small shift to the left of just 5 - 10 m along the  $x$  direction would make this location a failure.

Let us investigate how deep is the fresh rock along the traverse, particularly around the borehole position. First we impose the Earth surface to be the target axis to concentrate conductive material, as a manner of obtaining an estimate where the fresh rock be as shallow as possible. To this end we combine the SC- $\ell_1$  (just in  $x$  direction) and MMI constraints in the whole mesh, obtaining the results shown in Figure 14f. Using a conservative threshold value around 180 Ohm.m to the transition from weathered to fresh rock (log-resistivity around 2.25, corresponding the transition from yellow to red in the image), we infer from Figure 14f that the depth to the fresh rock is at least 50 m around positions 210 - 220 m. On the other hand, to favour estimates where the fresh rock be as deep as possible, we divide the mesh into the three partitions shown in Figure 14g and obtain estimates using the axes A and B to concentrate conductive materials in  $\Gamma_2$  and  $\Gamma_3$ , respectively, besides the DCT constraint in the whole mesh. The inversion results are shown in Figure 14h, from which we can infer that the depth to the fresh rock is at most 80 m around positions 210 - 220 m, using the same criteria above described. Given the range 50 - 80 m to the depth of the fresh rock, the borehole should have been drilled to a greater depth than 40 m, in order to obtain a greater pumping rate.

In a similar way to the synthetic models, all inversion results of Field 1 case are stable (Figure 15a), presenting standard deviation around 1.5%. As expected, however, the data fitting is worst than in the synthetic cases. Now typically 90% of the observations are reproduced with an error up to 15% (Figure 15b) instead of the 3% limit obtained with synthetic data (Figures 7b, 9b, and 11b). The best data fitting is provided by the solution using just the DCT constraint (Figure 14d), whereas the worst data fitting was obtained with the SC- $\ell_1$  (Figure 14a) constraint. Note that the solution imposing MMI constraints along vertical axes (Figure 14h) offers intermediate data fitting and can not be ruled out based on

this criteria. From an interpretative viewpoint, we take the two solutions favouring either shallower (Figure 14f) or deepest (Figure 14h) fresh rock interfaces as the best solutions because they both honor the observations and constitute the end members of the solution family compatible with the a priori geological conceptions.

The inversion results obtained in Field 2 case using SC- $\ell_1$ , SC- $\ell_2$ , TV, DCT, and DWT constraints are shown in Figures 14a to 14e, respectively. In each case, the constraint is used in the whole mesh. As in Field 1 case, the SC- $\ell_2$  image (Figure 16b) is very similar to the other four images. Thus, we infer again that the contacts are mainly transitional. Note however that in the interval 200 - 300 m the area associated to the union of cells presenting light blue to green colors in the images (around 100 Ohm.m) is clearly small than in Field 1 case in the same position interval. Thus, the Field 2 traverse is clearly worst than the Field 1 traverse to locate a borehole, an inference compatible with the two contrasting pumping rates above described.

Let us try an inversion test favouring the occurrence of deep conductive cells in the interval 200 - 300 m. Then, we divide the mesh into six partitions (Figure 16f), and define the axes A and B to concentrate conductive materials using the MMI constraints in  $\Gamma_1$ ,  $\Gamma_2$ ,  $\Gamma_3$ , and  $\Gamma_5$ , accordingly to the target axes present in each of these partitions. In addition, we use the DCT or the DWT constraint in the whole mesh. The inversion results are shown in Figures 16g and 16h for DCT and DWT constraints, respectively. The results are very similar to the previously ones, so that it is confirmed that Field 2 traverse is worst than the Field 1 one to locate a borehole.

Similarly to the Field 1 case, all Field 2 inversion results are stable (Figure 17a) and honor the observations (Figure 17b) under the same criteria (around 90% of the observations

are reproduced with an error up to 15%). The best and worst data fitting are provided by the solutions using the SC- $\ell_2$  (Figure 16b) and SC- $\ell_1$  (Figure 16a) constraints, respectively. Note that the solution imposing MMI constraints along vertical axes (Figures 16g and 16h) offers intermediate data fitting and can not be ruled out based on this criteria. From an interpretative viewpoint, we chose the SC- $\ell_2$  (Figure 16b) because it is compatible with the a priori geological conceptions and offers the best data fitting.

## DISCUSSION

The key point to highlight is the fact that, once the PSO algorithm (or any other GOM) is implemented for the 2D model, cost function modifications, either on changing constraints or data fitting criteria, can be performed very easily (Barboza et al., 2017). In addition, different constraints might be combined for different partitions of the interpretation mesh. As a result, the interpreter has to his/her disposal a very flexible tool to test hypothesis, in a similar manner he/she has when using a friendly forward modeling algorithm to perform a trial-and-error modeling approach. If the inversion algorithm is coupled with a modeling module, the interpreter might even alternate phases of automatic inversion with phases of trial-and-error forward modeling. For example, in the Karst 2 case, after obtaining the inversion results shown in Figures 8g and 8h, the interpreter might perform an analyses of detectability in the apparent resistivity data of the deep conductive horizontal dissolution around position 140 m, as manner of ascertaining that it is not an artefact of the inversion bias with null effects in the observations. The interpreter has then freedom to perform a quantitative interpretation based on a combined trial-and-error modeling and inversion approach.

In this work, we explore just one data fitting criterium (classic least-squares) and eight

types of constraints:  $SC-\ell_1$ ,  $SC-\ell_2$ ,  $SC-\ell_1^x$ , TV, DCT, DWT, MMI in relation to a generic axis, and MMI in relation to the Earth surface, besides a few combinations of them, in particular DCT + MMI, DWT + MMI, and  $SC-\ell_1^x$  + MMI. However, the plethora of constraints available from the literature might be implemented in a GOM for automatic inversion. In addition, all the synthetic and field examples we treat are limited to cases where the MMI constraint is expected to be adequate. So, in general, we begin the interpretation process with generic constraints, that give the first images, from which target axes are proposed to appraise MMI constraints. Off course, in cases where the MMI constraint is not adequate, the final phases of the interpretation process might be obtained with other constraints, which are more compatible with the interpreter conception about the geologic environment.

We stress that any constrained solution of an inverse problem is a biased solution. So the key question is: where is going the solution in the parameter space? If the solution is going toward a point that is compatible with the available information about the study area, this is a good thing (Silva et al., 2001b). In the contrary, this is a bad thing, no matter how sophisticated or simple the constraint is. We defend then that the interpreter must to take the control of the bias in the interpretation process, instead of using black box inversion softwares. In testing several constraints for a given case, the interpreter has at least one monitoring tool: the data fitting. If a constrained inversion solution impacts severely the data fitting, the employed constraint is certainly not adequate to the case (e.g. Santana et al., 2012). In the contrary situation, there is no reason to rule out the solution and its acceptance or rejection depends just on the interpreter appraisal that is always based on his/her a priori conception about the study area.

From the technical point of view, two improvements are very important to the successful

implementation of the PSO algorithm for the 2D DC-resistivity inversion problem. The first one is the normalization introduced in equations 3 and 5, which have a strong role in the robustness of the algorithm to changes in the cost function, particularly in the invariance of the Lagrange multipliers. In this sense, whenever a new constraint is introduced in the cost function, adequate normalization must be sought. For details about the normalization factors, please see the Appendix A and Table 1. The second improvement is the couple of modifications introduced in the sorting process of the starting particles of the PSO swarm; for details please see the Appendix B.

An important by-product of the stopping criteria of the PSO algorithm (or any other GOM) is the cluster of suboptimal quasi-solutions that allows to perform an uncertainty analysis around the best solution (e.g. Alvarez et al., 2008; Fernández-Martínez et al., 2014; Pallero et al., 2015). The size of the confidence region depend on the employed constraints. In this sense, it is important to emphasize the need of requiring convergence on each isolated term of the cost function, otherwise it would be possible to obtain premature solutions in which the constraints are not properly incorporated (Silva et al., 2001a; Barboza et al., 2017).

## CONCLUSIONS

In solving the 2D DC-resistivity inversion problem, a PSO algorithm (or any other GOM) offer high flexibility to modify the cost function, allowing the interpreter to change easily either the data fitting criteria or the employed constraints. Equally important, the interpretation mesh might be divided into partitions, where different constraints might be combined. As a result, the interpreter has freedom to perform a quantitative interpretation process based on a trial-and-error inversion approach, possibly combined with phases of

trial-and-error forward modeling. In addition, from the stopping criteria of the PSO algorithm results not only the best solution but also a cluster of suboptimal quasi-solutions from which uncertainty analyses can be performed.

To obtain such flexibility, two technical improvements in the PSO algorithm are necessary. The first one is normalizing each term of the cost function in order to allow robustness of the algorithm to changes in the cost function terms. The second improvement is to modify the sorting process of the starting particles of the PSO swarm to better deal with parameters that can change easily over three orders of magnitude.

The main limitation of the presented inversion approach is computer time because each cost function evaluation requires a forward modeling. So its application is still limited to geophysical inverse problems where forward modeling is computationally inexpensive. For example, the presented inversion approach can be nowadays extended to 2D/3D grav & mag and 2D electromagnetic inverse problems but not to seismic inverse problems. Note however that due to the constant advancement of computing power, this obstacle tends to be increasingly smaller.

## ACKNOWLEDGMENTS

The brazilian agency CNPq is thanked for the PhD scholarship to FMB, the research fellowship and associated grant (Proc. 304301/2011-6) to WEM, and the financial support to purchase the computational infrastructure used in this study.

## APPENDIX A

### Mathematical Expressions of the Constraints

In this appendix we present a summary of the mathematical expressions of the employed constraints to stabilize the solutions of the inverse problems. A particular constraint  $\mathcal{R}_{p\ell}$  (equation 4) might be employed in the whole mesh or just in a partition  $\Gamma_p$  of the mesh (Figure 1). In addition, in a certain partition  $\Gamma_p$  more than one constraint might be applied. As a result, the Lagrange multipliers  $\mu_{p\ell}$  (equation 4) and the normalization factors  $f_{p\ell}$  (equation 5) must be in general defined for each pair  $(p, \ell)$  of partition-constraint.

The denominators in the normalization factors  $f_{p\ell}$  (equation 5) are chosen in order that the product  $f_{p\ell}\mathcal{R}_{p\ell}$  be dimensionless and around 1. These normalizations are of great importance because, after them, the task of assigning values to the Lagrange multipliers  $\mu_{p\ell}$  is facilitated because we may now consider these values as percentages. More importantly, these normalizations promote robustness to the PSO algorithm (Barboza et al., 2017). We verified with preliminary tests that values of  $\mu_{p\ell}$  around 0.03 are sufficient to stabilize all estimates when the constraints are normalized. The variances contained in the particular definitions of  $f_{p\ell}$  given below might be specified by the interpreter based on his/her experience or they can be estimated using preliminary gross inversion estimates. To obtain this kind of estimates we run preliminary inversion tests using typically  $\mu_{p\ell}$  around 0.01 and  $f_{p\ell} = 1$ . To allow reproduction of the inversion results, in Table 1 we list all values of  $\mu_{p\ell}$  and  $f_{p\ell}$  that were used in the inversion examples.

### Spatial continuity constraint (SC- $\ell_1$ and SC- $\ell_2$ )

This classical constraint (e.g. Tikhonov and Arsenin, 1977; Constable et al., 1987) imposes that the spatial variation of the physical property is minimized. We use the log-resistivity ( $\log \rho_{i,j}$ ) as the physical property and we measure the discrepancy between a pair of neighbouring values of the mesh with either the  $\ell_1$  or  $\ell_2$  norm (generically,  $\ell_q$  norm). The  $\ell_1$  norm favours more blockly structures (e.g. Loke et al., 2003; Sun and Li, 2014) allowing that possible localized regions of discrepancy in the resistivity might appear in the inversion results. On the other hand, the  $\ell_2$  norm smears out the spatial variations so that blurred images are obtained. The notation  $\mathcal{R}_1$  and  $\mathcal{R}_2$  (or SC- $\ell_1$  and SC- $\ell_2$ ) are used for the particular cases of  $\ell_1$  and  $\ell_2$  norms, respectively.

The mathematical expression for  $\mathcal{R}_q$  is

$$\mathcal{R}_q = \left[ \sum_{ij} D_{ij}^x + \sum_{ij} D_{ij}^z \right]. \quad (6)$$

In the above equation  $\sum_{ij}$  stands generically for the summation over all of pairs of neighbouring cells contained in the partition  $\Gamma_p$  where the constraint is applied. In addition,  $D_{ij}^x$  and  $D_{ij}^z$  are the norms of the first-order log-resistivity finite-differences in the directions  $x$  and  $z$  (Figure 1), respectively, given in the  $\ell_q$  norm by

$$D_{ij}^x = \left( \frac{|\log(\rho_{i,j+1}) - \log(\rho_{i,j})|}{\Delta x_j} \right)^q, \quad (7)$$

$$D_{ij}^z = \left( \frac{|\log(\rho_{i+1,j}) - \log(\rho_{i,j})|}{\Delta z_i} \right)^q. \quad (8)$$

The normalization factor  $f_q$  (equation 5) is given by

$$f_q = \frac{1}{N_p^{xz} |\sigma_{xz}^2|^{q/2}}, \quad (9)$$

where  $N_p^{xz}$  is the number of pairs of neighbouring cells and  $\sigma_{xz}^2$  is the variance of the discrepancies between pairs of adjacent log-resistivities, both quantities calculated in the partition  $\Gamma_p$ .

A particular case of equation 6 is to restrain just the horizontal variation of the log-resistivity, so that the constraint is given by

$$\mathcal{R}_q^x = \sum_{ij} D_{ij}^x. \quad (10)$$

The normalization factor is then equal to

$$f_q^x = \frac{1}{N_p^x |\sigma_x^2|^{q/2}}, \quad (11)$$

where  $N_p^x$  and  $\sigma_x^2$  are similar quantities to those ones defined in equation 9 but now using just the direction  $x$ .

### **Total variation constraint (TV)**

This constraint is defined as (Rudin et al., 1992):

$$\mathcal{R}_{TV} = \sum_{ij} \sqrt{(D_{ij}^x)^2 + (D_{ij}^z)^2}, \quad (12)$$

where  $D_{ij}^x$  and  $D_{ij}^z$  are given in equations 7 and 8. The total variation is essentially the  $\ell_1$  norm of the gradient (Portniaguine and Zhdanov, 1999). It minimizes the support of the region where the gradient of the physical property may vary; thus it can be considered alternatively as a sparsity constraint in the gradient of the physical property (Lustig et al., 2007). As a result, it also favours more blocky structures in a similar way to the spatial continuity constraint using the  $\ell_1$  norm.

The normalization factor  $f_{TV}$  (equation 5) is given by

$$f_{TV} = \frac{1}{N_p^{xz} |\sigma_{xz}^2|^{1/2}}, \quad (13)$$

where  $N_p^{xz}$  and  $\sigma_{xz}^2$  are the same quantities defined for equation 9.

### Sparsity constraint (DCT and DWT)

Inspired by the compressed sensing theory (Mallat, 2008; Donoho, 2006; Candès et al., 2006), using the  $\ell_1$  norm in association with a basis transformation has received considerable attention in geophysics (e.g. Loris et al., 2007; Jafarpour et al., 2009; Simons et al., 2011; Charléty et al., 2013). Defining  $N_p$  is the number of cells of the partition  $\Gamma_p$  and  $\mathbf{m}_p$  is the  $N_p$ -size vector containing just the elements of  $\mathbf{m}$  located in  $\Gamma_p$ , the sparsity constraint has the form

$$\mathcal{R}_B = \|\mathbf{B}^T \mathbf{m}_p\|_1 = \|\mathbf{s}_p\|_1, \quad (14)$$

where  $\mathbf{B}$  is a matrix of basis transformation (Mallat, 2008). As a result, it is imposed that  $\mathbf{s}_p$  have very few non-zero elements, being then a sparse representation of  $\mathbf{m}_p$ . To make easier the basis transformations,  $\mathbf{B}$  is selected as a wavelet basis so that  $\mathbf{B}^T = \mathbf{B}^{-1}$ . We use

two cases of wavelet basis: the Discrete Cosine Transform (DCT) and the Daubechies bases of order 4 (Mallat, 2008), whose associated constraints are named as  $\mathcal{R}_{DCT}$  and  $\mathcal{R}_{DWT}$ , respectively.

The normalization factor  $f_B$  (equation 5) is given by

$$f_B = \frac{1}{N_B |\sigma_B^2|^{1/2}}, \quad (15)$$

where  $N_B$  is the typical number of non-zero elements of  $\mathbf{s}_p$  and  $\sigma_B^2$  is an estimate of the variance of these non-zero elements.

### **Minimum moment of inertia constraint (MMI)**

This ingenious constraint was proposed by Guillen and Menichetti (1984) to express into mathematical terms the idea that an anomalous density distribution is concentrated around an axis. The constraint is to minimize the minimum moment of inertia of the anomalous mass in relation to the given axis. This constraint has been generalized to other physical properties, as for example, to magnetic susceptibility, already in the original paper of Guillen and Menichetti (1984), and to slowness by Ajo-Franklin et al. (2007). We apply it here in two cases. In the first case, there is an anomalous concentration of conductive material around an axis and surrounded by a medium of higher resistivity. In the second case the contrary occurs. Thus, conductive and resistive materials are respectively concentrated in the first and second cases. The vector of physical property is then generically denoted is  $\mathbf{g}$ . We stress that for this constraint we use resistivity (or conductivity) and not log-resistivity.

Given a target axis to the physical property distribution with mass center at the point  $(z, x) = (\beta, \alpha)$  and dip angle equal to  $\theta$ , the minimum moment of inertia constraint  $\mathcal{R}_M$  is

defined (Guillen and Menichetti, 1984) as:

$$\mathcal{R}_M = \left\| \mathbf{W}^{1/2} \mathbf{g}_p \right\|_2^2, \quad (16)$$

where  $\mathbf{g}_p$  is the  $N_p$ -size vector containing just the elements of  $\mathbf{g}$  located in  $\Gamma_p$  and the diagonal weight matrix  $\mathbf{W}$  has elements given by

$$w_k = \frac{\Delta x_k \Delta z_k (\gamma_k^2 + d_k^2)}{|g_k| + \delta}. \quad (17)$$

In the above equation  $k$  refers to the cells contained in the partition  $\Gamma_p$  where the constraint is applied. In addition,  $d_k^2$  given by

$$d_k^2 = (x_k - \alpha)^2 \sin^2 \theta + (z_k - \beta)^2 \cos^2 \theta - (x_k - \alpha)(z_k - \beta) \sin^2 \theta \quad (18)$$

is the square distance from the center of the  $k$ -th cell to the axis, and  $\gamma_k^2$  given by

$$\gamma_k^2 = \frac{1}{4} \left( \frac{\Delta z_k^2}{3} \cos^2 \theta - \frac{\Delta x_k \Delta z_k}{4} \sin^2 \theta + \frac{\Delta x_k^2}{3} \sin^2 \theta \right) \quad (19)$$

is a quantity depending on the cell shape, in this case assumed to be a rectangle. Finally,  $\delta$  in equation 17 is a small number whose role is just to avoid a singularity in the case  $g_k$  approaches to zero. In the version we implement the axis dip  $\theta$  is a priori fixed but the mass center position  $(\beta, \alpha)$  is updated along the optimization process. By this way we try to conform to the most common case where the target axis dip is known from geological information but its position is unknown.

The normalization factor  $f_M$  (equation 5) is given by

$$f_M = \frac{1}{N_p \sigma_{\mathcal{R}_M}^2}, \quad (20)$$

where  $N_p$  is the number of cells contained in the partition  $\Gamma_p$  and  $\sigma_{\mathcal{R}_M}^2$  is an estimate of the variance of  $\mathcal{R}_M$  (equation 16).

A particular case of equation 16 is to use the Earth surface as the target axis (Barbosa et al., 1999). In this case  $d_k^2 = z_k^2$  and  $\gamma_k^2 = \Delta z_k^2/12$ .

## APPENDIX B

### Particle Swarm Optimization (PSO)

PSO simulates the social behavior of a swarm of individuals of the same species, like birds, in the search for food (Kennedy et al., 2001). The key idea is that while searching for food, the particles (birds) are either scattered or go together, but always sharing all information; eventually when a very good place is found by any of the particles, the entire swarm flocks to this place.

The swarm is formed by  $N_S$  particles. We use  $N_S \approx 5N_{par}$ , where  $N_{par} = N_x N_z$  is the number of cells in the interpretation mesh (Figure 1). Each particle  $n$  of the swarm may occupy different positions  $\mathbf{m}_n^\tau$  of the search space  $\Omega$  at the time (iteration)  $\tau$ .  $\mathbf{m}_n^\tau$  are then trial solutions to the cost function  $\mathcal{L}$  (equation 2), being the initial positions randomly chosen in  $\Omega$ .

Commonly the initial positions of the particles are sorted accordingly to a uniform probability density function (pdf) (Figure 18). We followed this approach in Barboza et al. (2017) for the 1.5D DC-resistivity inverse problem, where the parameters to be estimated are resistivity and thickness values of a layer-cake model. However, the 2D DC-resistivity inverse problem treated here falls into the category of high-dimensional search space optimization, where the use of an uniform pdf may result in poor performances for PSO (Helwig and Wanka, 2007). Now choosing bounds for the cell resistivities is not a simple task because these values might easily vary over three orders of magnitude. Indeed we verified that using an uniform pdf to randomly sort resistivity values has led to a very slow convergence because the sorted starting values, for most of the cells, are too far from the expected values. To overcome this situation we perform two modifications: the first is sorting directly in the

log-scale, that is, sorting log-resistivity values (and not resistivity values), and the second modification is to use a triangular pdf instead of an uniform one (Figure 18). After several inversion tests, we select the following pdf  $\varphi(r)$  (where  $r$  is log-resistivity):

$$\varphi(r) = \begin{cases} \frac{2(r-a)}{(b-a)(c-a)} & \text{for } a \leq r \leq c \\ \frac{2(b-r)}{(b-a)(b-c)} & \text{for } c \leq r \leq b \\ 0 & \text{for any other case} \end{cases} \quad (21)$$

where  $a$ ,  $b$ , and  $c$  are the minimum, maximum, and most probable values for the log-resistivity of each cell contained in the partition  $\Gamma_p$  (Figure 18). Note that  $a$ ,  $b$ , and  $c$  might be function of position  $x$  and depth  $z$ . To estimate these parameters we use two different approaches. The first one is used for the initial phases of the quantitative interpretation process (as, for example, for the estimates results shown in Figures 14a to 14e), when the interpreter has not yet conceived a target model to the inversion results. In this case,  $a$ ,  $b$ , and  $c$  are obtained using just the soundings: a single pair of values  $a$  and  $b$  is chosen for the whole mesh so that the defined interval is large enough to contain all possible values for the cell resistivities; in addition,  $c$  is estimated using a gross empirical rule relating electrode spacing with investigation depth (we use  $z = AB/2$  for the Schlumberger array) and  $c(z_i, x_j)$  is obtained by interpolating the log-apparent resistivity values in the mesh. On the other hand, the second approach is used for the final phases of the quantitative interpretation process, when the interpreter has already conceived a target model to the inversion results. In this case,  $c(z_i, x_j)$  is composed with the estimated values obtained in one of the initial inversion results; for example, the inversion results shown in Figure 16d compose the  $c(z_i, x_j)$  values for the estimates shown in Figure 16h. In addition, we define  $a(z_i, x_j) = 0.3c(z_i, x_j)$  and  $b(z_i, x_j) = 1.5c(z_i, x_j)$  so that all pdf parameters are now

function of  $x$  and  $z$ .

Once the initial positions of the swarm particles has been sorted, the optimization process is started. At iteration  $\tau$  the positions  $\mathbf{m}_n^\tau$  of all particles  $n$  ( $n = 1, \dots, N_S$ ) are updated using the equation

$$\mathbf{m}_n^\tau = \mathbf{m}_n^{\tau-1} + v_n^\tau, \quad (22)$$

where the step  $v_n^\tau$  results from a compromise of three trends: the previous step  $v_n^{\tau-1}$  ( $v_n^0 = 0$ ), the best position already occupied by the particle itself  $\mathbf{m}_n^B$ , and the best position already occupied by a particle of the swarm  $\mathbf{m}^{BB}$ , accordingly to the equation

$$v_n^\tau = \omega.v_n^{\tau-1} + c_1.r_1(\mathbf{m}_n^B - \mathbf{m}_n^{\tau-1}) + c_2.r_2(\mathbf{m}^{BB} - \mathbf{m}_n^{\tau-1}). \quad (23)$$

In the above equation,  $\omega$ ,  $c_1$  and  $c_2$  are the control parameters named as inertia weight, cognitive parameter, and social parameter, respectively. Good convergence of the solutions were obtained by using  $\omega = 0.73$  and  $c_1 = c_2 = 1.50$ , which are values compatible with those ones reported in the literature (e.g. Clerc and Kennedy, 2002; Trelea, 2003; Fernández-Martínez and García-Gonzalo, 2008). On the other hand,  $r_1$  and  $r_2$  (equation 23) are pseudorandom numbers uniformly distributed in the range 0 to 1 (Haupt and Haupt, 2004). The iterations continue until stopping criteria are attained, when the global minimum is associated with the resulting best position  $\mathbf{m}^{BB}$  (Kennedy et al., 2001).

The employed stopping criteria are the same defined in Barboza et al. (2017). For completeness they are below reproduced just adapting the nomenclature to the inverse problem treated here. We refer as stage for one complete sweep of the swarm. A Cauchy type convergence criterion (e.g. Bartle, 1964) is used to each parcel of the cost function  $\mathcal{L}$

(equation 2), that is, we impose isolated convergence criteria for  $\Phi_a$  (equation 3) and for each one of the employed constraints  $\mathcal{R}_{pl}$  (equation 4). Testing individually the convergence of each parcel of  $\mathcal{L}$  ensures not only that the observations are fitted but also that each constraint is effectively incorporated (Silva et al., 2001a). Designating  $\Phi_a$  or  $\mathcal{R}_{pl}$  generically by  $G$ , convergence is assumed when, for  $N_C$  consecutive times, the relative variation of  $G$  in two successive stages ( $s - 1$  and  $s$ ) is stagnated below a threshold  $\delta_G$ , that is:

$$\chi_s^G = \left\| \frac{G(\mathbf{m}_s^{\mathbf{BB}}) - G(\mathbf{m}_{s-1}^{\mathbf{BB}})}{G(\mathbf{m}_s^{\mathbf{BB}})} \right\| \leq \delta_G, \text{ for } N_C \text{ consecutive times,} \quad (24)$$

where  $\mathbf{m}_s^{\mathbf{BB}}$  and  $\mathbf{m}_{s-1}^{\mathbf{BB}}$  are the best solutions in stages  $s$  and  $s - 1$ , respectively. We use  $N_C = 200$  and a stagnation threshold equal to  $10^{-6}$  for all cost function terms. Note that using a single threshold for all terms is only possible because of the normalizations imposed in equation 3, for the misfit term, and of the normalization factors defined in equation 9 and similar ones.

As examples, Figures 19 and 20 show evolution curves of the cost function and its parcel for the Karst 1 and Field 1 cases, respectively. From the joint analysis of these figures, we stress the following facts: a) convergence curves for both field and synthetic data present the same behavior, b) the normalization approach performed quite well in all cases, a good evidence of this affirmation being the fact that evolution curves of very different constraints can be plotted together using the same scale, c) for a particular inversion example, convergence criteria are attained at different stages for different constraints, d) for a particular constraint set, convergence criteria are attained at different stages for different inversion examples, and e) even for a fixed pair of inversion example - constraint set, convergence criteria are attained at different stages for the misfit and constraint parcels of the cost

function. Jointly the last three facts justify the use of isolated convergence criteria for each parcel of the cost function (Silva et al., 2001a).

At the end of the convergence process, the interpreter has not only the best solution but also a set of suboptimal quasi-solutions, which can be used to perform an uncertainty analysis (e.g. Alvarez et al., 2008; Fernández-Martínez et al., 2014; Pallero et al., 2015). The best solution and the set of quasi-solutions compose a cluster from which the variability of the solution can be estimated using, for example, simple statistics as mean and standard deviation of the model parameters, as we show in Figures 7a, 9a, and 11a for synthetic data and in Figures 15a and 17a for field data. Due to the convergence criteria (equation 24), we obtain clusters with 201 points.

## REFERENCES

- Ajo-Franklin, J. B., B. J. Minsley, and T. M. Daley, 2007, Applying compactness constraints to differential travelttime tomography: *Geophysics*, **72**, no. 4, R67–R75.
- Alvarez, J. F., J. F. Martínez, and C. M. Pérez, 2008, Feasibility analysis of the use of binary genetic algorithms as importance samplers application to a 1-D DC resistivity inverse problem: *Mathematical Geosciences*, **40**, 375–408.
- Araripe, P. D. T., and F. Feijó, 1994, Potiguar basin: *Boletim de Geociências da PETROBRAS*, **8**, 127–141.
- Attwa, M., I. Akca, A. T. Basokur, and T. Günther, 2014, Structure-based geoelectrical models derived from genetic algorithms: a case study for hydrogeological investigations along Elbe River coastal area, Germany: *Journal of Applied Geophysics*, **103**, 57–70.
- Auken, E., A. V. Christiansen, B. H. Jacobsen, N. Foged, and K. I. Sørensen, 2005, Piecewise 1D laterally constrained inversion of resistivity data: *Geophysical Prospecting*, **53**, no. 4, 497–506.
- Barbosa, V. C., J. B. Silva, and W. E. Medeiros, 1999, Stable inversion of gravity anomalies of sedimentary basins with nonsmooth basement reliefs and arbitrary density contrast variations: *Geophysics*, **64**, 754–764.
- Barboza, F. M., W. E. Medeiros, and J. M. Santana, 2017, Customizing constraint incorporation in DC-resistivity inverse problems: a comparison among three global optimization methods: *Geophysics*, in revision process.
- Bartle, R. G., 1964, *The elements of real analysis*: Wiley New York, **2**.
- Başokur, A. T., I. Akca, and N. W. Siyam, 2007, Hybrid genetic algorithms in view of the evolution theories with application for the electrical sounding method: *Geophysical Prospecting*, **55**, 393–406.

- Biswas, A., and S. Sharma, 2014, Optimization of self-potential interpretation of 2-D inclined sheet-type structures based on very fast simulated annealing and analysis of ambiguity: *Journal of Applied Geophysics*, **105**, 235–247.
- Candès, E. J., J. Romberg, and T. Tao, 2006, Robust uncertainty principles: Exact signal reconstruction from highly incomplete frequency information: *IEEE Transactions on Information Theory*, **52**, 489–509.
- Carrière, S. D., K. Chalikakis, G. Sénéchal, C. Danquigny, and C. Emblanch, 2013, Combining electrical resistivity tomography and ground penetrating radar to study geological structuring of karst unsaturated zone: *Journal of Applied Geophysics*, **94**, 31–41.
- Charléty, J., S. Voronin, G. Nolet, I. Loris, F. J. Simons, K. Sigloch, and I. C. Daubechies, 2013, Global seismic tomography with sparsity constraints: Comparison with smoothing and damping regularization: *Journal of Geophysical Research: Solid Earth*, **118**, 4887–4899.
- Clerc, M., and J. Kennedy, 2002, The particle swarm-explosion, stability, and convergence in a multidimensional complex space: *IEEE transactions on Evolutionary Computation*, **6**, 58–73.
- Constable, S. C., R. L. Parker, and C. G. Constable, 1987, Occam's inversion: A practical algorithm for generating smooth models from electromagnetic sounding data: *Geophysics*, **52**, 289–300.
- Dey, A., and H. Morrison, 1979, Resistivity modelling for arbitrarily shaped two-dimensional structures: *Geophysical Prospecting*, **27**, 106–136.
- Donoho, D. L., 2006, Compressed sensing: *IEEE Transactions on Information Theory*, **52**, 1289–1306.
- Ezersky, M., 2008, Geoelectric structure of the Ein Gedi sinkhole occurrence site at the

- Dead Sea shore in Israel: *Journal of Applied Geophysics*, **64**, 56–69.
- Fernandes, A. L., W. E. Medeiros, F. H. Bezerra, J. G. Oliveira, and C. L. Cazarin, 2015, GPR investigation of karst guided by comparison with outcrop and unmanned aerial vehicle imagery: *Journal of Applied Geophysics*, **112**, 268–278.
- Fernández-Martínez, J., and E. García-Gonzalo, 2008, The generalized PSO: a new door to PSO evolution: *Journal of Artificial Evolution and Applications*, **2008**, 1–15.
- Fernández Martínez, J. L., T. Mukerji, E. García Gonzalo, and A. Suman, 2012, Reservoir characterization and inversion uncertainty via a family of particle swarm optimizers: *Geophysics*, **77**, no. 1, M1–M16.
- Fernández-Martínez, J. L., J. Pallero, Z. Fernández-Muñiz, and L. M. Pedruelo-González, 2014, The effect of noise and Tikhonov’s regularization in inverse problems. Part II: The nonlinear case: *Journal of Applied Geophysics*, **108**, 186–193.
- Gill, P. E., W. Murray, and M. H. Wright, 1981, *Practical optimization*.
- Goldberg, D., 1989, *Genetic algorithms in search, optimization and machine learning reading*: Addison-Wisley.
- Guillen, A., and V. Menichetti, 1984, Gravity and magnetic inversion with minimization of a specific functional: *Geophysics*, **49**, 1354–1360.
- Gutiérrez, F., J. Galve, P. Lucha, J. Bonachea, L. Jordá, and R. Jordá, 2009, Investigation of a large collapse sinkhole affecting a multi-storey building by means of geophysics and the trenching technique (Zaragoza city, NE Spain): *Environmental Geology*, **58**, 1107–1122.
- Gyulai, Á., and T. Ormos, 1999, A new procedure for the interpretation of VES data: 1.5-D simultaneous inversion method: *Journal of Applied Geophysics*, **41**, 1–17.
- Haupt, R. L., and S. E. Haupt, 2004, *Practical genetic algorithms*: John Wiley & Sons.
- Helwig, S., and R. Wanka, 2007, Particle swarm optimization in high-dimensional bounded

- search spaces: Swarm Intelligence Symposium - SIS 2007. IEEE, 198–205.
- Jafarpour, B., V. K. Goyal, D. B. McLaughlin, and W. T. Freeman, 2009, Transform-domain sparsity regularization for inverse problems in geosciences: *Geophysics*, **74**, no. 5, R69–R83.
- Jha, M. K., S. Kumar, and A. Chowdhury, 2008, Vertical electrical sounding survey and resistivity inversion using genetic algorithm optimization technique: *Journal of Hydrology*, **359**, 71–87.
- Kennedy, J., and R. Eberhart, 1995, Particle swarm optimization: Presented at the Proc. IEEE International Conf. on Neural Networks (Perth, Australia), IEEE Service Center, Perth, Australia.
- Kennedy, J., R. Eberhart, and Y. Shi, 2001, *Swarm Intelligence*, Morgan Kaufmann Publishers: Inc., San Francisco, CA.
- Kirkpatrick, S., C. D. Gelatt, M. P. Vecchi, et al., 1983, Optimization by simulated annealing: *Science*, **220**, no. 4598, 671–680.
- Loke, M., J. Chambers, D. Rucker, O. Kuras, and P. Wilkinson, 2013, Recent developments in the direct-current geoelectrical imaging method: *Journal of Applied Geophysics*, **95**, 135–156.
- Loke, M. H., I. Acworth, and T. Dahlin, 2003, A comparison of smooth and blocky inversion methods in 2D electrical imaging surveys: *Exploration Geophysics*, **34**, 182–187.
- Loris, I., G. Nolet, I. Daubechies, and F. Dahlen, 2007, Tomographic inversion using l1-norm regularization of wavelet coefficients: *Geophysical Journal International*, **170**, 359–370.
- Lustig, M., D. Donoho, and J. M. Pauly, 2007, Sparse MRI: The application of compressed sensing for rapid MR imaging: *Magnetic Resonance in Medicine*, **58**, 1182–1195.
- Mallat, S., 2008, *A wavelet tour of signal processing: the sparse way*: Academic press.

- Martínez, J. L. F., E. G. Gonzalo, J. P. F. Álvarez, H. A. Kuzma, and C. O. M. Pérez, 2010, PSO: A powerful algorithm to solve geophysical inverse problems: application to a 1D-DC resistivity case: *Journal of Applied Geophysics*, **71**, 13–25.
- Medeiros, W. E., 1987, The resistivity method applied to the hydrogeology of crystalline terrains: A problem of two-dimensional modelling: Master's thesis, Universidade Federal da Bahia, Brazil (in Portuguese).
- Medeiros, W. E., and O. A. Lima, 1990, A geoelectrical investigation for ground water in crystalline terrains of Central Bahia, Brazil: *Ground Water*, **28**, 518–523.
- Morgan, E. C., M. Vanneste, I. Lecomte, L. G. Baise, O. Longva, and B. McAdoo, 2012, Estimation of free gas saturation from seismic reflection surveys by the genetic algorithm inversion of a P-wave attenuation model: *Geophysics*, **77**, no. 4, R175–R187.
- Nyquist, J. E., J. S. Peake, and M. J. Roth, 2007, Comparison of an optimized resistivity array with dipole-dipole soundings in karst terrain: *Geophysics*, **72**, F139–F144.
- Pallero, J., J. L. Fernández-Martínez, S. Bonvalot, and O. Fudym, 2015, Gravity inversion and uncertainty assessment of basement relief via particle swarm optimization: *Journal of Applied Geophysics*, **116**, 180–191.
- Pei, D., J. N. Louie, and S. K. Pullammanappallil, 2007, Application of simulated annealing inversion on high-frequency fundamental-mode rayleigh wave dispersion curves: *Geophysics*, **72**, no. 5, R77–R85.
- Portniaguine, O., and M. S. Zhdanov, 1999, Focusing geophysical inversion images: *Geophysics*, **64**, 874–887.
- Roth, M., J. Mackey, C. Mackey, and J. Nyquist, 2002, A case study of the reliability of multielectrode earth resistivity testing for geotechnical investigations in karst terrains: *Engineering Geology*, **65**, 225–232.

- Rucker, D. F., and T. P. Ferré, 2005, Automated water content reconstruction of zero-offset borehole ground penetrating radar data using simulated annealing: *Journal of Hydrology*, **309**, 1–16.
- Rudin, L. I., S. Osher, and E. Fatemi, 1992, Nonlinear total variation based noise removal algorithms: *Physica D: Nonlinear Phenomena*, **60**, 259–268.
- Santana, F. L., W. E. Medeiros, A. F. do Nascimento, and F. H. Bezerra, 2012, Hypocentral relocation using clustering-along-planes constraints: implications for fault geometry: *Geophysical Journal International*, **190**, 1077–1090.
- Santos, F. M., S. Sultan, P. Represas, and A. El Sorady, 2006, Joint inversion of gravity and geoelectrical data for groundwater and structural investigation: application to the northwestern part of Sinai, Egypt: *Geophysical Journal International*, **165**, 705–718.
- Sen, M. K., and P. L. Stoffa, 1995, *Global optimization methods in geophysical inversion*: Elsevier.
- Shaw, R., and S. Srivastava, 2007, Particle swarm optimization: A new tool to invert geophysical data: *Geophysics*, **72**, no. 2, F75–F83.
- Silva, J. B., W. E. Medeiros, and V. C. Barbosa, 2001a, Pitfalls in nonlinear inversion: *Pure and Applied Geophysics*, **158**, 945–964.
- , 2001b, Potential-field inversion: Choosing the appropriate technique to solve a geologic problem: *Geophysics*, **66**, 511–520.
- Simons, F. J., I. Loris, G. Nolet, I. C. Daubechies, S. Voronin, J. Judd, P. A. Vetter, J. Charléty, and C. Vonesch, 2011, Solving or resolving global tomographic models with spherical wavelets, and the scale and sparsity of seismic heterogeneity: *Geophysical Journal International*, **187**, 969–988.
- Smith, D. L., 1986, Application of the pole-dipole resistivity technique to the detection of

- solution cavities beneath highways: *Geophysics*, **51**, 833–837.
- Sun, J., and Y. Li, 2014, Adaptive Lp inversion for simultaneous recovery of both blocky and smooth features in a geophysical model: *Geophysical Journal International*, **197**, 882–899.
- Tikhonov, A. N., and V. Y. Arsenin, 1977, *Solutions of ill-posed problems*: Winston.
- Trelea, I. C., 2003, The particle swarm optimization algorithm: convergence analysis and parameter selection: *Information Processing Letters*, **85**, 317–325.
- Tronicke, J., H. Paasche, and U. Böniger, 2012, Crosshole travelttime tomography using particle swarm optimization: A near-surface field example: *Geophysics*, **77**, no. 1, R19–R32.
- Valois, R., C. Camerlynck, A. Dhemaied, R. Guerin, G. Hovhannissian, V. Plagnes, F. Rejiba, and H. Robain, 2011, Assessment of doline geometry using geophysics on the Quercy plateau karst (South France): *Earth Surface Processes and Landforms*, **36**, 1183–1192.
- Wang, R., C. Yin, M. Wang, and G. Wang, 2012, Simulated annealing for controlled-source audio-frequency magnetotelluric data inversion: *Geophysics*, **77**, no. 2, E127–E133.
- Xavier Neto, P., 2006, *Processamento e interpretação de dados 2D e 3D de GPR: aplicações no imageamento de feições kársticas e estruturas de dissolução no campo de petróleo de Fazenda Belém-CE*: PhD thesis, Universidade Federal do Rio Grande do Norte, Brasil (in Portuguese).
- Zhu, J., J. C. Currens, and J. S. Dinger, 2011, Challenges of using electrical resistivity method to locate karst conduits—a field case in the inner Bluegrass Region, Kentucky: *Journal of Applied Geophysics*, **75**, 523–530.

## LIST OF FIGURES

**Figure 1.** Scheme of the mesh covering the subsurface interpretation region  $\Gamma$  used for the 2D DC-resistivity modeling and inversion problems. The mesh has  $N_x$  by  $N_z$  cells along distance  $x$  and depth  $z$ , respectively. The mesh size  $\Delta_{x_j}$  along  $x$  is uniform but the mesh size  $\Delta_{z_i}$  along  $z$  typically increases with depth. Any cell might be identified by the pair  $(i, j)$  ( $i = 1, 2, \dots, N_z; j = 1, 2, \dots, N_x$ ) or by the cell counting number  $k = i + (j - 1)N_z$  ( $k = 1, 2, \dots, N_x N_z$ ). The interpretation region  $\Gamma$  might be divided into  $P$  non-overlapping partitions  $\Gamma_p$  ( $p = 1, 2, \dots, P$ ) (in the figure  $P = 3$ ), where different constraints for the inverse problem might be employed.

**Figure 2.** Photograph of a cliff in a limestone quarry (Jandaíra Formation, Potiguar basin, Brazil) exposing karst structures. Zooms of the cliff walls (A and B) exhibit dissolution voids along horizontal bedding, which might be filled with unconsolidated sediments. Subvertical fractures might connect horizontal dissolution voids as in zoom A. Photograph source: Xavier Neto (2006).

**Figure 3.** Synthetic data - Karst 1: a) Subsurface resistivity distribution. b) Modeled Schlumberger soundings (21 curves); the soundings are equally spaced (20 m apart) being the first and last centers located at positions 0 m and 400 m, respectively. (c) Apparent resistivity section. The water table (not shown) is assumed to be very shallow so that all karst structures in (a) are conductive in relation to the unaltered rock.

**Figure 4.** Synthetic data - Karst 2: a) Subsurface resistivity distribution. b) Modeled Schlumberger soundings (21 curves); the soundings are equally spaced (20 m apart) being the first and last centers located at positions 0 m and 400 m, respectively. (c) Apparent resistivity section. The water table in (a) is 15 m deep, so that the karst structures respectively above and beneath the water table are conductive and resistive in relation to the

unaltered rock. Note that the resistivity of the unaltered rock also varies according to its position in relation to the water table.

**Figure 5.** Synthetic data - Dike: a) Subsurface resistivity distribution. b) Modeled Schlumberger soundings (21 curves); the soundings are equally spaced (20 m apart) being the first and last centers located at positions 0 m and 400 m, respectively. (c) Apparent resistivity section.

**Figure 6.** Synthetic data - Karst 1: Estimates obtained with SC- $\ell_1$  (a), SC- $\ell_2$  (b), TV (c), DCT (d), and DWT (e) constraints. From (a) to (e) each constraint is applied in the whole mesh. A partition is defined for the mesh (f), being the starting axes A, B, and C inferred from (d) and (e). Finally, (g) and (h) show estimates using respectively DCT and DWT constraints on the whole mesh, except in  $\Gamma_1$ , besides MMI in  $\Gamma_2$  to  $\Gamma_7$  to concentrate conductive material, accordingly to the axes contained in each partition. In  $\Gamma_1$  (soil) no constraint is applied.

**Figure 7.** Synthetic data - Karst 1: (a) confidence interval (mean  $\pm$  one standard deviation) for the log-resistivity estimates of the mesh cells. To obtain this figure, each quasi-solution for the log-resistivity of a cell (resulting from stopping criteria of the PSO algorithm) is expressed as percentage discrepancy in relation to the respective best PSO solution and all statistics are grouped as a single pair of mean percentage discrepancy and its associated standard deviation. (b) Cumulative distribution for the percentage discrepancy between modeled and observed apparent resistivity data. Correspondence of constraint and figure number showing the estimates:  $\mathcal{R}_1$  (6a),  $\mathcal{R}_2$  (6b),  $\mathcal{R}_{TV}$  (6c),  $\mathcal{R}_{DCT}$  (6d),  $\mathcal{R}_{DWT}$  (6e),  $\mathcal{R}_M + \mathcal{R}_{DCT}$  (6g), and  $\mathcal{R}_M + \mathcal{R}_{DWT}$  (6h).

**Figure 8.** Synthetic data - Karst 2: Estimates obtained with SC- $\ell_1$  (a), SC- $\ell_2$  (b), TV (c), DCT (d), and DWT (e) constraints. From (a) to (e) each constraint is applied in

the whole mesh. A partition is defined for the mesh (f), being the starting axes A and B inferred from (d) and (e). Finally, (g) and (h) show estimates using respectively DCT and DWT constraints on the whole mesh, besides MMI in  $\Gamma_1$  and  $\Gamma_2$  to concentrate resistive and conductive materials around axes A and B, respectively.

**Figure 9.** Synthetic data - Karst 2: (a) confidence interval (mean  $\pm$  one standard deviation) for the log-resistivity estimates of the mesh cells, obtained in the same manner as in Figure 7a. (b) Cumulative distribution for the percentage discrepancy between modeled and observed apparent resistivity data. Correspondence of constraint and figure number showing the estimates:  $\mathcal{R}_1$  (8a),  $\mathcal{R}_2$  (8b),  $\mathcal{R}_{TV}$  (8c),  $\mathcal{R}_{DCT}$  (8d),  $\mathcal{R}_{DWT}$  (8e),  $\mathcal{R}_M + \mathcal{R}_{DCT}$  (8g), and  $\mathcal{R}_M + \mathcal{R}_{DWT}$  (8h).

**Figure 10.** Synthetic data - Dike: Estimates obtained with SC- $\ell_1$  (a), TV (b), DCT (c), and DWT (d) constraints. From (d) a starting dipping axis A is proposed resulting in the estimates shown in (e) using MMI to concentrate conductive material around axis A. From (a) to (e) each constraint is applied in the whole mesh. From (e) a refinement to the starting axis is proposed, besides a partition for the mesh (f). Finally, (g) and (h) show estimates using respectively SC- $\ell_1$  (just in  $x$  direction) and DCT constraints on the whole mesh, except in  $\Gamma_1$ , besides MMI in  $\Gamma_3$  to concentrate conductive material around axis B. In  $\Gamma_1$  (soil) no constraint is applied.

**Figure 11.** Synthetic data - Dike: (a) confidence interval (mean  $\pm$  one standard deviation) for the log-resistivity estimates of the mesh cells, obtained in the same manner as in Figure 7a. (b) Cumulative distribution for the percentage discrepancy between modeled and observed apparent resistivity data. Correspondence of constraint and figure number showing the estimates:  $\mathcal{R}_1$  (10a),  $\mathcal{R}_{TV}$  (10b),  $\mathcal{R}_{DCT}$  (10c),  $\mathcal{R}_{DWT}$  (10d),  $\mathcal{R}_M$  (10e),  $\mathcal{R}_M + \mathcal{R}_1^x$  (10g), and  $\mathcal{R}_M + \mathcal{R}_{DCT}$  (8h).

**Figure 12.** Field 1 case: a) Schlumberger soundings (21 curves); the soundings are equally spaced (20 m apart) being the first and last centers located at positions 0 m and 400 m, respectively. (c) Apparent resistivity section.

**Figure 13.** Field 2 case: a) Schlumberger soundings (21 curves); the soundings are equally spaced (20 m apart) being the first and last centers located at positions 0 m and 400 m, respectively. (c) Apparent resistivity section.

**Figure 14.** Field 1 case: Estimates obtained with SC- $\ell_1$  (a), SC- $\ell_2$  (b), TV (c), DCT (d), and DWT (e) constraints. Two constraints are used in (f): SC- $\ell_1$  (just in  $x$  direction) and MMI concentrating conductive material around the Earth surface. From (a) to (f) each constraint is applied in the whole mesh. From (d) two starting subvertical axes are proposed to investigate how deep might be the fracture zone, besides a partition for the mesh (g). Finally, (h) shows estimates using DCT constraints on the whole mesh, besides MMI in  $\Gamma_2$  and  $\Gamma_3$  to concentrate conductive material, accordingly to the axis contained in each partition.

**Figure 15.** Field 1 case: (a) confidence interval (mean  $\pm$  one standard deviation) for the log-resistivity estimates of the mesh cells, obtained in the same manner as in Figure 7a. (b) Cumulative distribution for the percentage discrepancy between modeled and observed apparent resistivity data. Correspondence of constraint and figure number showing the estimates:  $\mathcal{R}_1$  (14a),  $\mathcal{R}_2$  (14b),  $\mathcal{R}_{TV}$ (14c),  $\mathcal{R}_{DCT}$ (14d),  $\mathcal{R}_{DWT}$ (14e),  $\mathcal{R}_M$  (14e),  $\mathcal{R}_M + \mathcal{R}_1^x$  (14f), and  $\mathcal{R}_M + \mathcal{R}_{DCT}$  (14h).

**Figure 16.** Field 2 case: Estimates obtained with SC- $\ell_1$  (a), SC- $\ell_2$  (b), TV (c), DCT (d), and DWT (e) constraints. From (a) to (e) each constraint is applied in the whole mesh. A partition is defined for the mesh (f), being the starting axes A and B inferred from (d) and (e). Finally, (g) and (h) show estimates using respectively DCT and DWT constraints

on the whole mesh, besides MMI in  $\Gamma_1$ ,  $\Gamma_2$ ,  $\Gamma_3$ , and  $\Gamma_5$  to concentrate conductive materials, accordingly to the axes contained in each partition.

**Figure 17.** Field 2 case: (a) confidence interval (mean  $\pm$  one standard deviation) for the log-resistivity estimates of the mesh cells, obtained in the same manner as in Figure 7a. (b) Cumulative distribution for the percentage discrepancy between modeled and observed apparent resistivity data. Correspondence of constraint and figure number showing the estimates:  $\mathcal{R}_1$  (16a),  $\mathcal{R}_2$  (16b),  $\mathcal{R}_{TV}$ (16c),  $\mathcal{R}_{DCT}$ (16d),  $\mathcal{R}_{DWT}$ (16e),  $\mathcal{R}_M + \mathcal{R}_{DCT}$  (16g), and  $\mathcal{R}_M + \mathcal{R}_{DWT}$  (16h).

**Figure 18.** Uniform (thin line) and triangular (heavy line) forms for the probability density function (pdf) employed to sort the initial positions of the particles composing the swarm in the PSO algorithm. Parameters  $a$ ,  $b$ , and  $c$  are the minimum, maximum, and most probable values for the log-resistivity of each cell  $k$  contained in the partition  $\Gamma_p$  (Figure 1). Equation 21 define the triangular pdf.

**Figure 19.** Synthetic data - Karst 1: Evolution of the cost function value (a) (equation 2) and its parcel associated with data fitting (b) (equation 3) and constraints (c) (equation 6 and similar ones in Appendix A) of the momentarily best solution along the stages of the PSO algorithm. Correspondence of constraint and figure number showing the estimates:  $\mathcal{R}_1$  (6a),  $\mathcal{R}_2$  (6b),  $\mathcal{R}_{TV}$ (6c),  $\mathcal{R}_{DCT}$  (6d),  $\mathcal{R}_{DWT}$  (6e),  $\mathcal{R}_M + \mathcal{R}_{DCT}$  (6g), and  $\mathcal{R}_M + \mathcal{R}_{DWT}$  (6h).

**Figure 20.** Field 1 case: Evolution of the cost function value (a) (equation 2) and its parcel associated with data fitting (b) (equation 3) and constraints (c) (equation 6 and similar ones in Appendix A) of the momentarily best solution along the stages of the PSO algorithm. Correspondence of constraint and figure number showing the estimates:  $\mathcal{R}_1$  (14a),  $\mathcal{R}_2$  (14b),  $\mathcal{R}_{TV}$ (14c),  $\mathcal{R}_{DCT}$ (14d),  $\mathcal{R}_{DWT}$ (14e),  $\mathcal{R}_M$  (14e),  $\mathcal{R}_M + \mathcal{R}_1^x$  (14g), and

$$\mathcal{R}_M + \mathcal{R}_{DCT} \text{ (14h).}$$

## LIST OF TABLES

**Table 1.** Values of the Lagrange multipliers  $\mu$  and normalization factors  $f$  employed in all inversion examples. Each constraint  $\mathcal{R}$  is identified by its main equation of definition. In addition, each pair of inversion example - constraint set is identified by the figure label showing the inversion results. To specify precisely the MMI constraints, we add to both  $\mu$  and  $f$  an index identifying the target axis as, for example,  $\mu_{M_A}$  and  $f_{M_A}$  for the MMI constraint around axis A in the inversion example shown in Figure 6g.



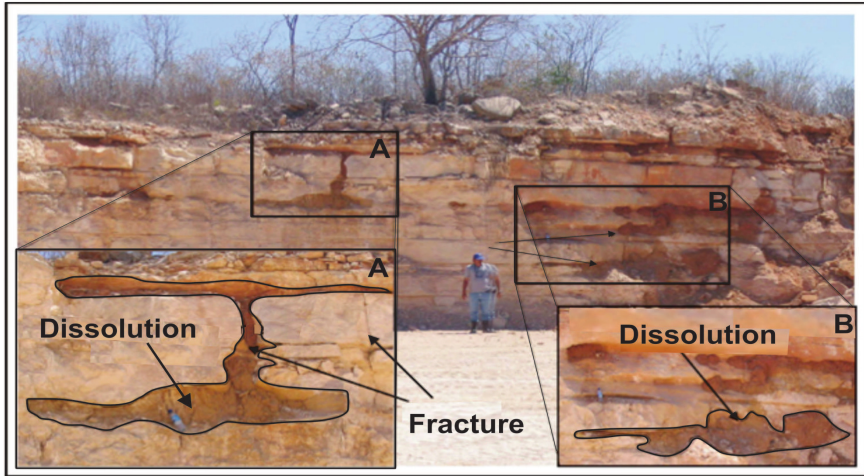


Figure 2

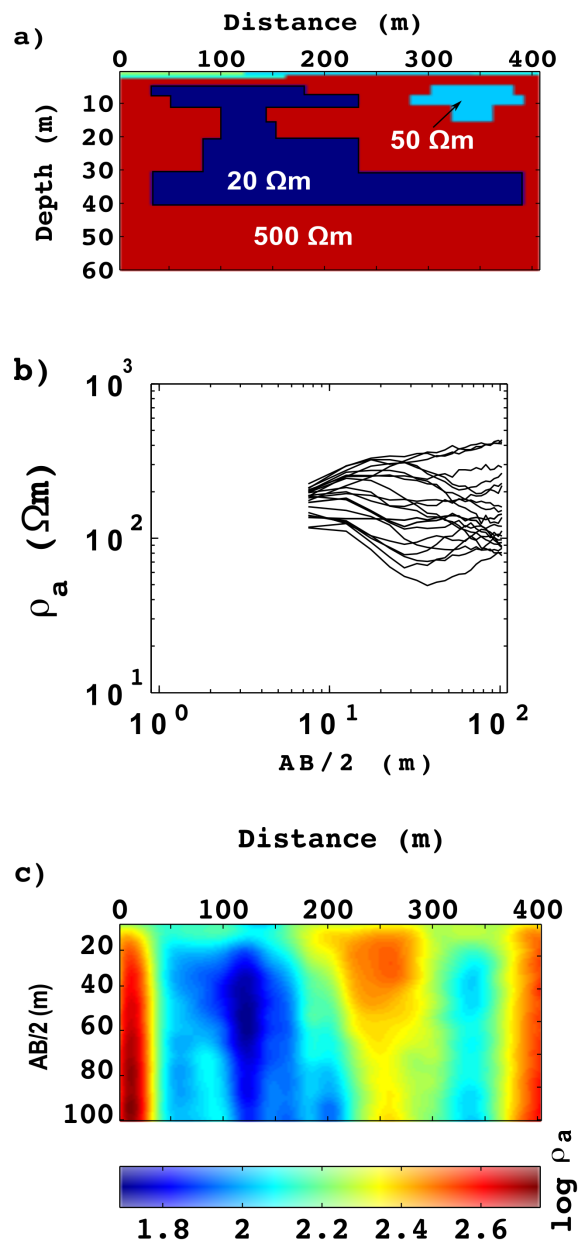


Figure 3

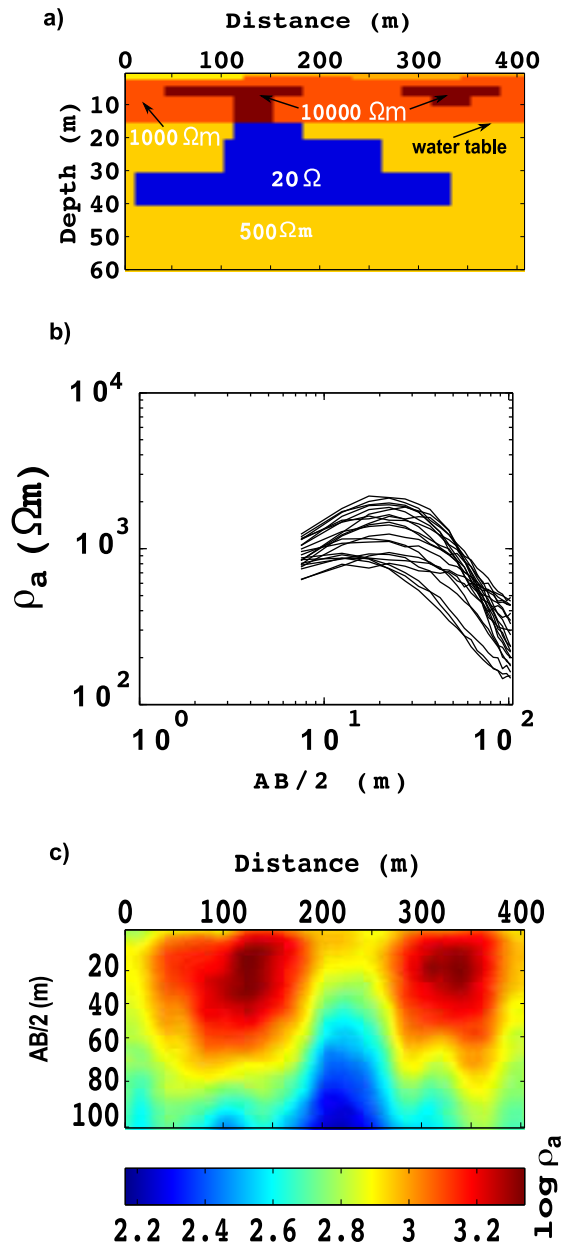


Figure 4

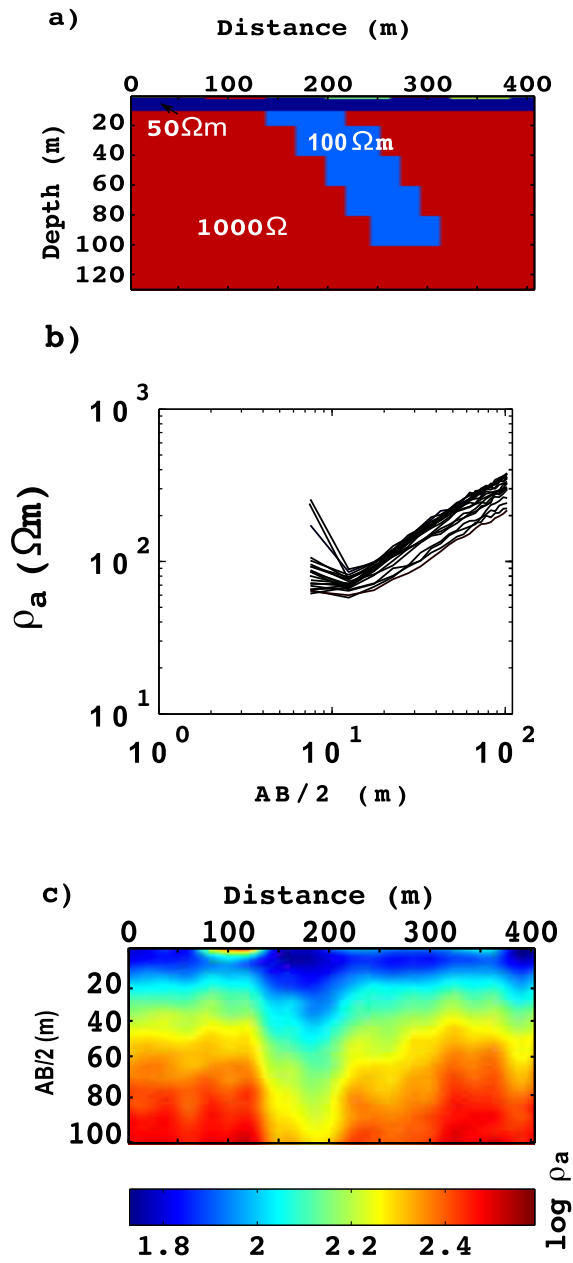


Figure 5

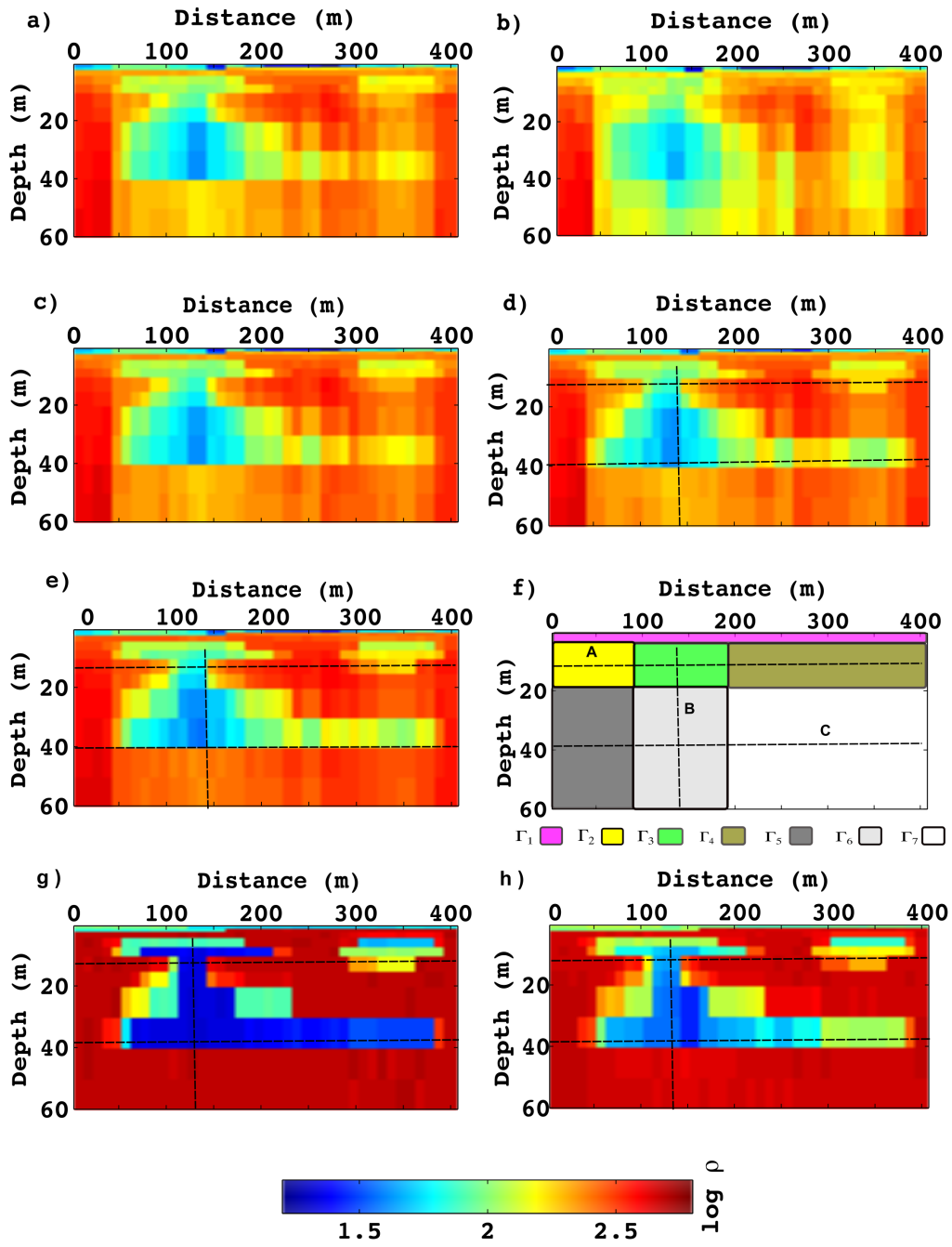


Figure 6

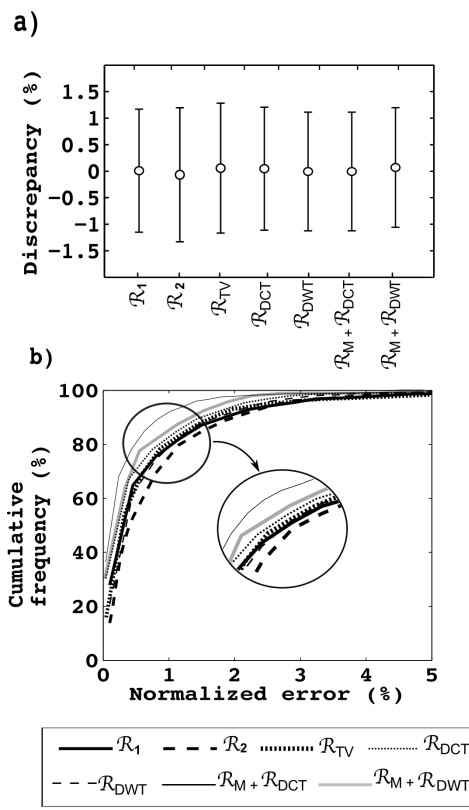


Figure 7

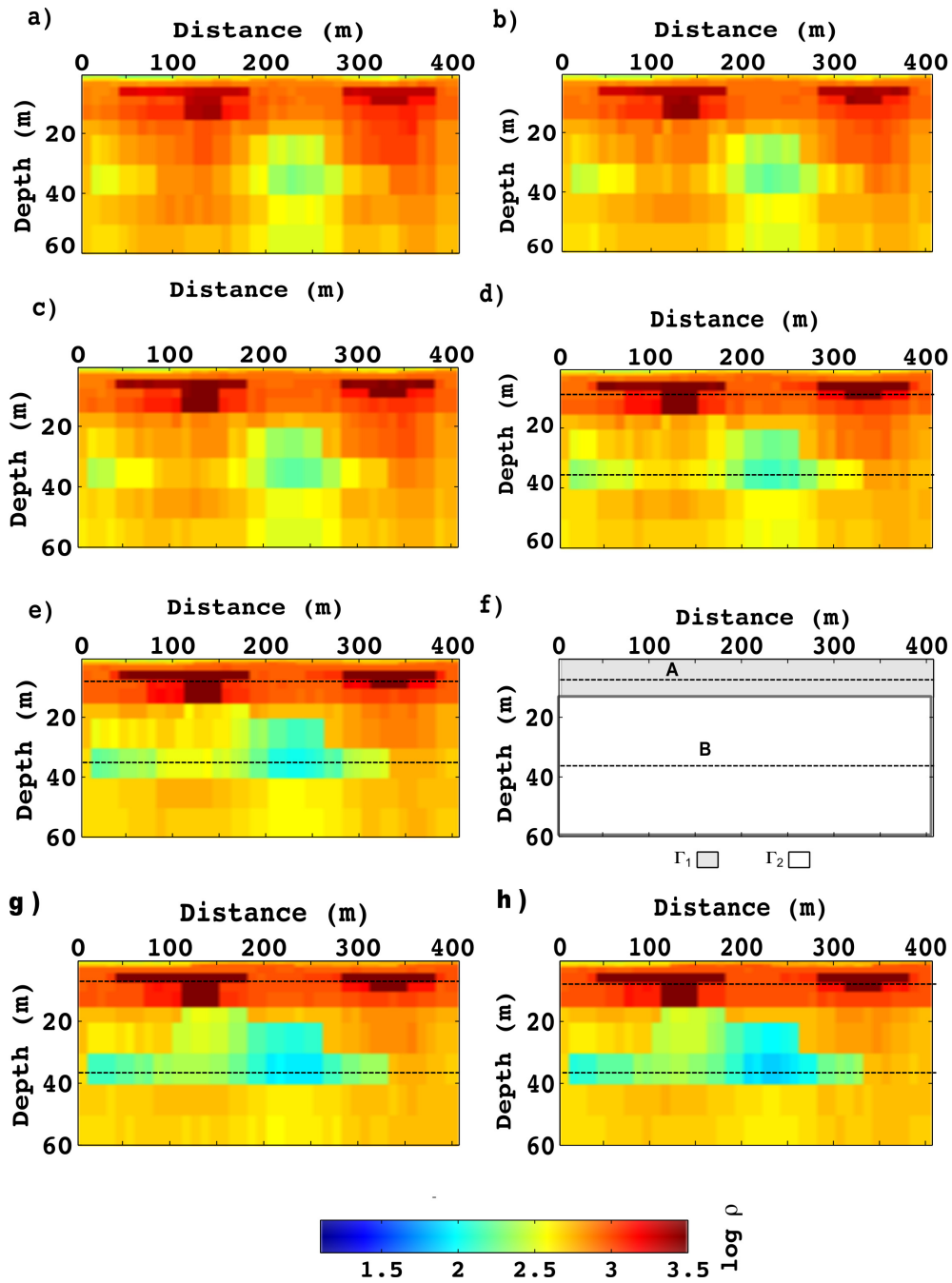


Figure 8

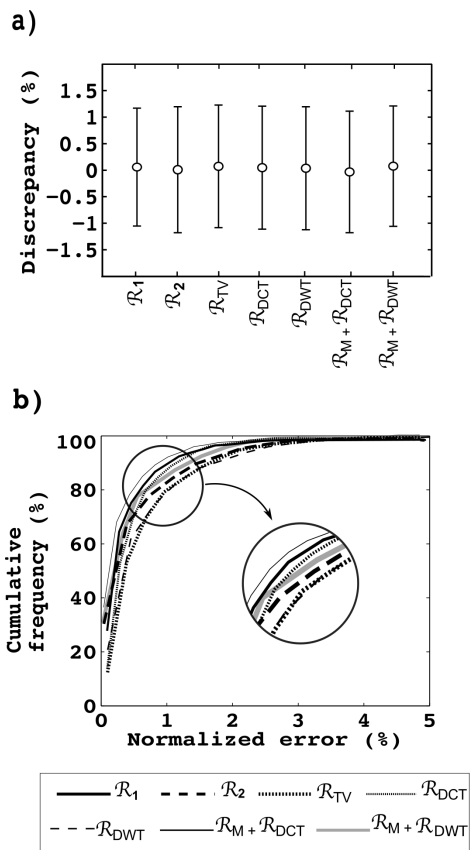


Figure 9

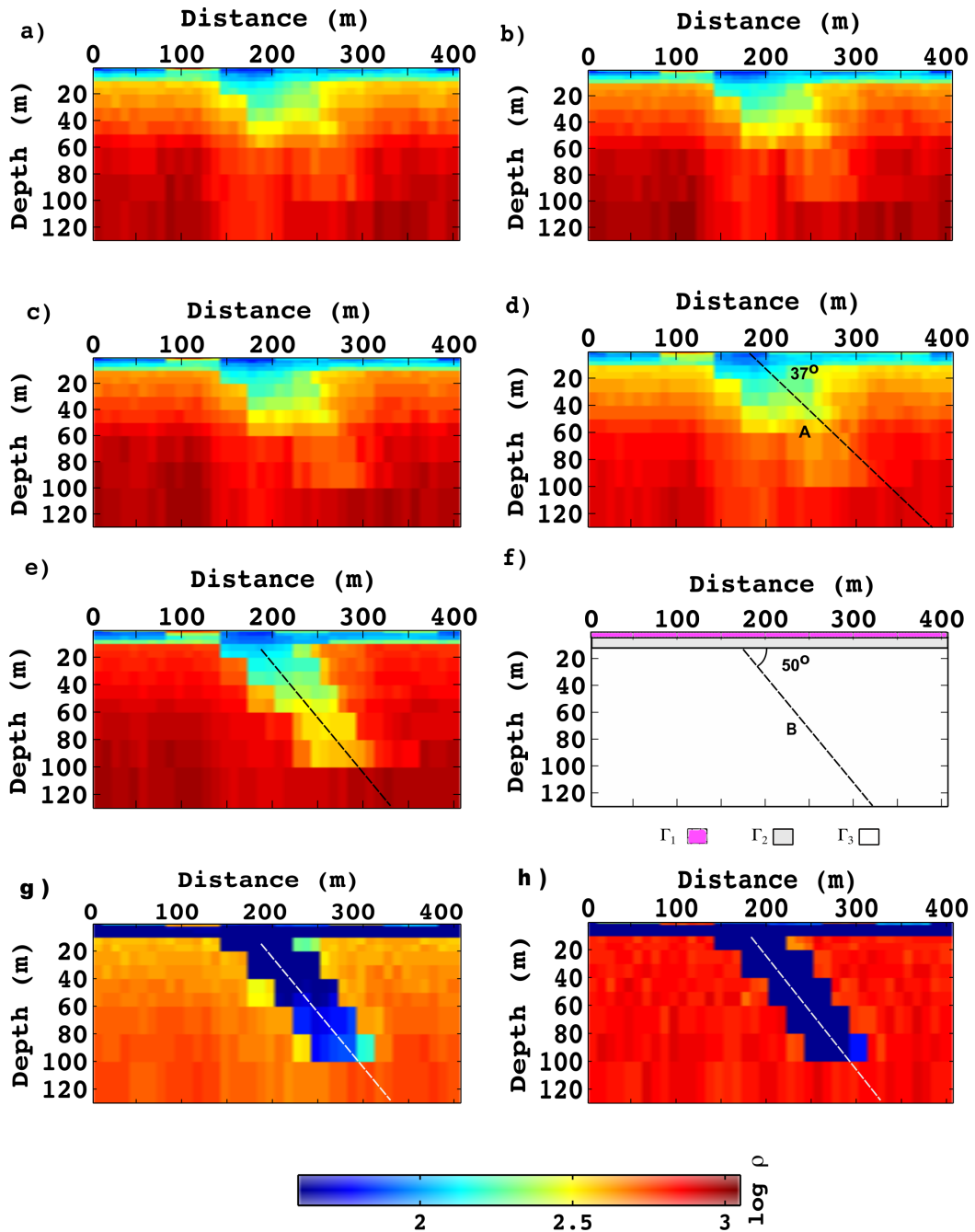


Figure 10

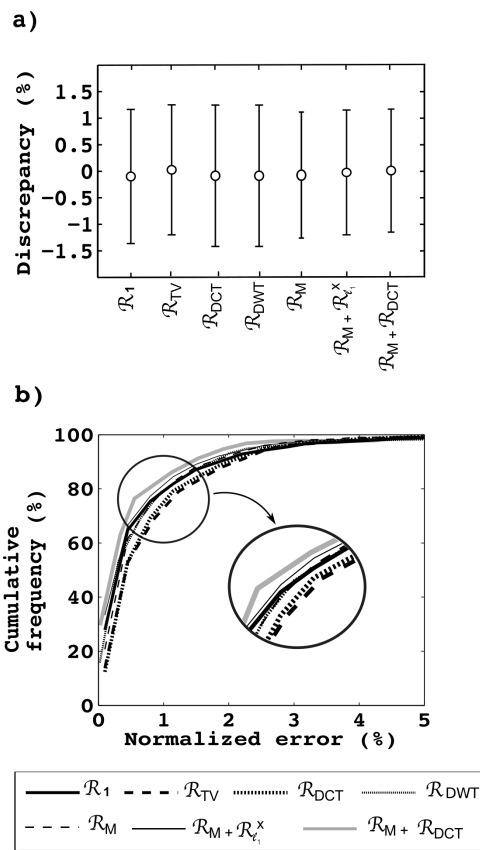


Figure 11

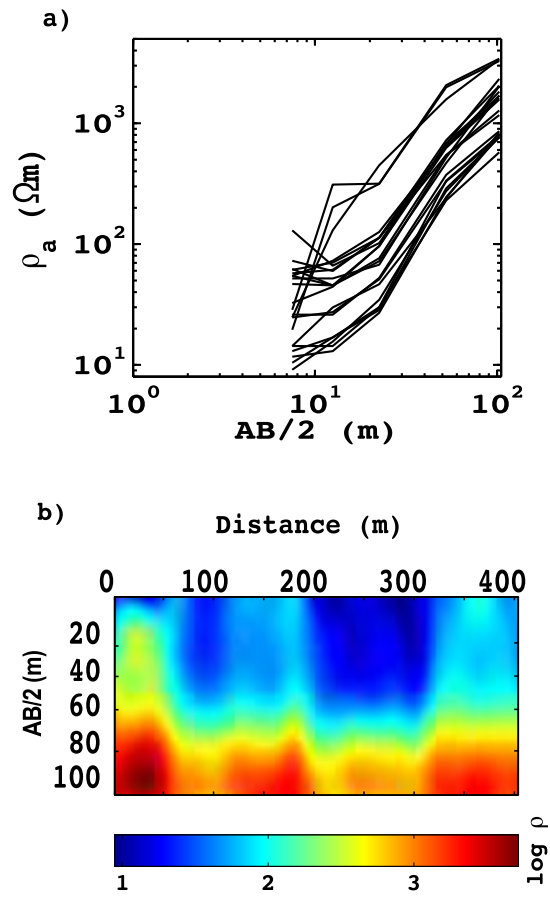


Figure 12

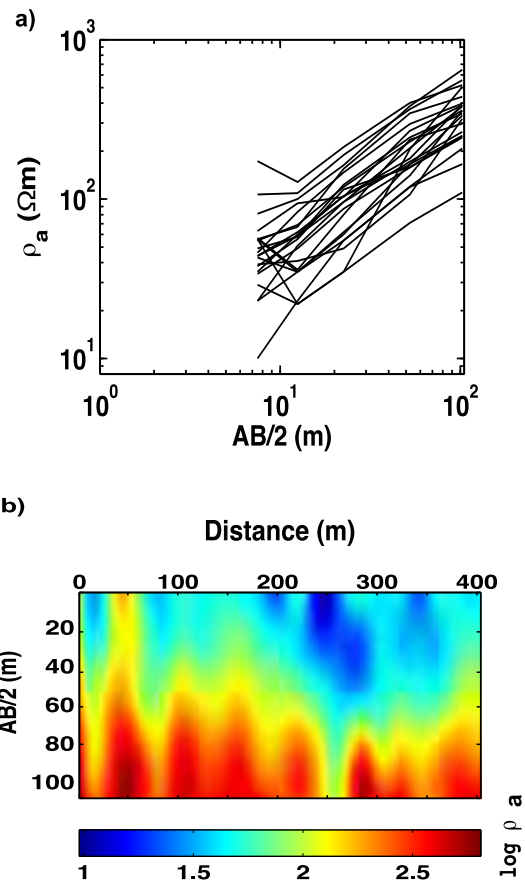


Figure 13

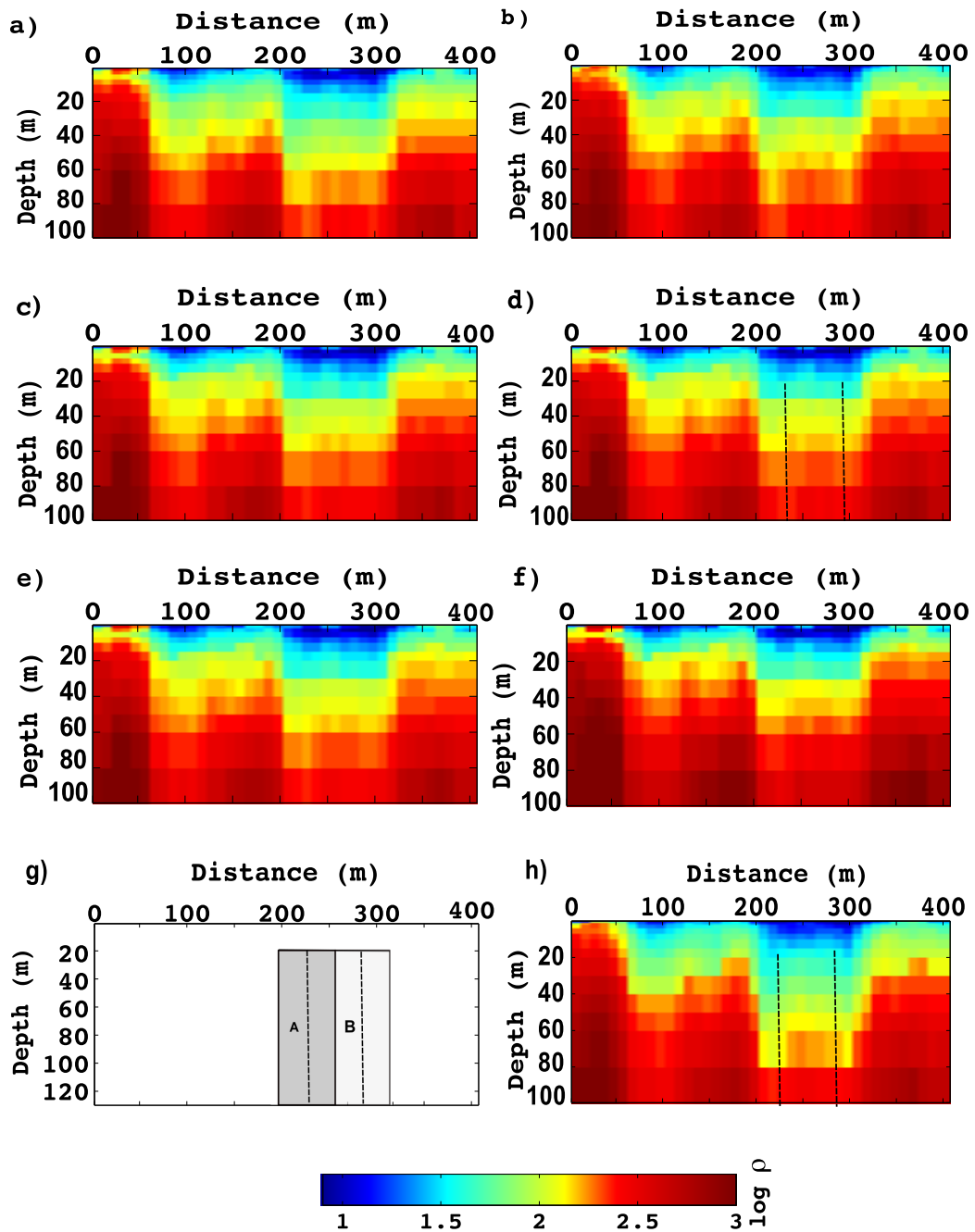
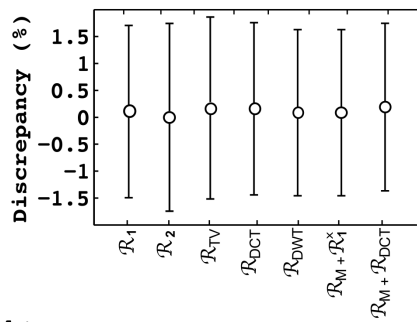


Figure 14

a)



b)

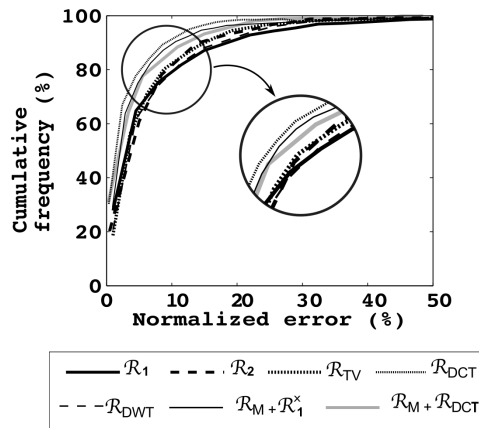


Figure 15

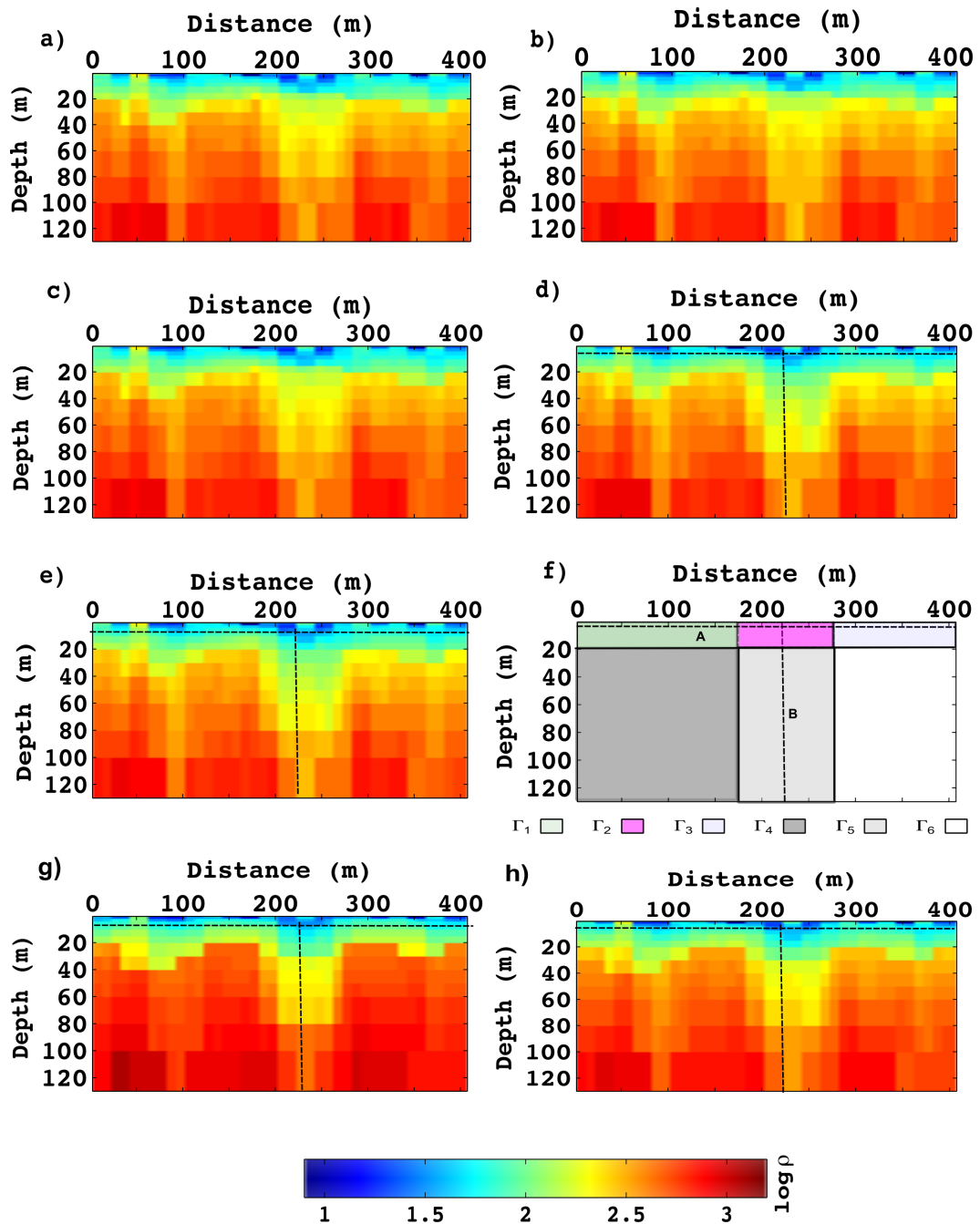
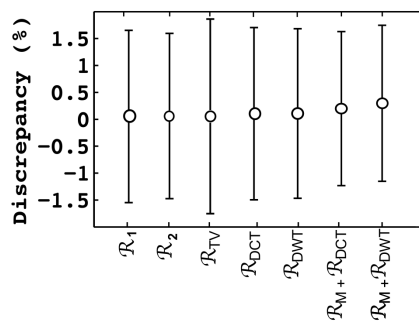


Figure 16

a)



b)

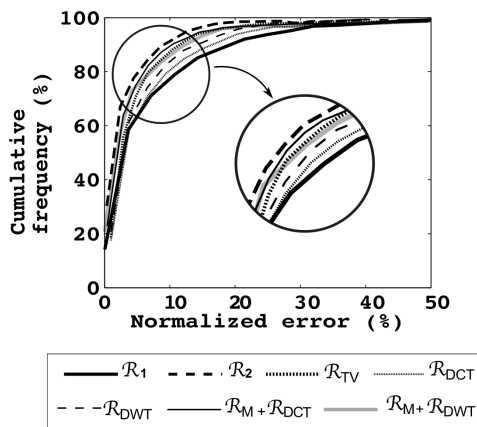


Figure 17

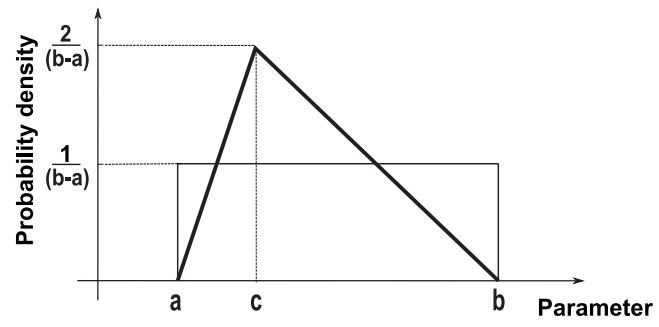


Figure 18

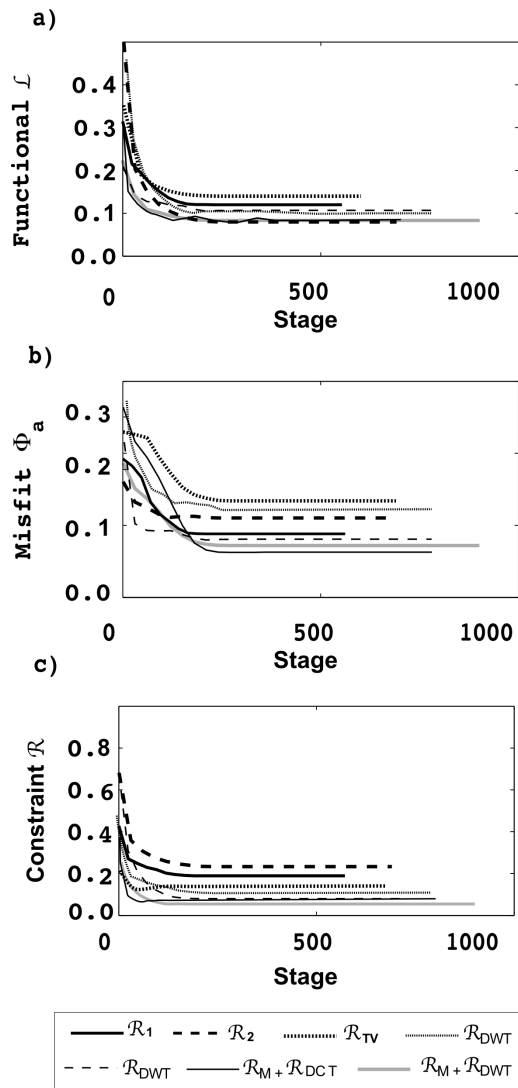


Figure 19

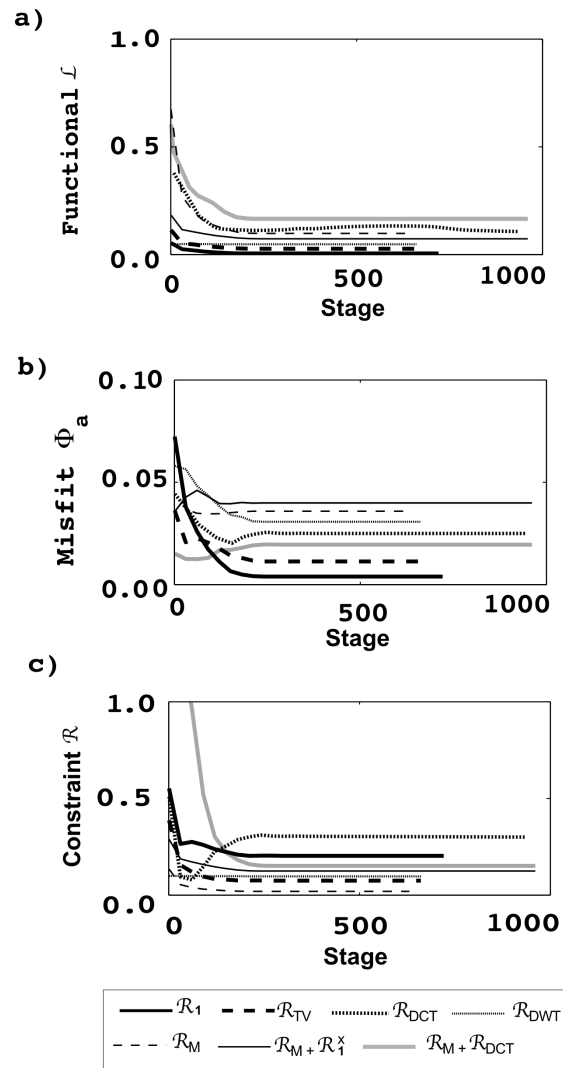


Figure 20

Model	Karst 1	Karst 2	Dike	Field 1	Field 2
$\mathcal{R}_1$ (eq. 6)	Figure 6a $\mu_1 = 0.05$ $f_1 = 3.0$	Figure 8a $\mu_1 = 0.04$ $f_1 = 2.3$	Figure 10a $\mu_1 = 0.02$ $f_1 = 6.7$	Figure 14a $\mu_1 = 0.05$ $f_1 = 1.5$	Figure 16a $\mu_1 = 0.07$ $f_1 = 3.2$
$\mathcal{R}_2$ (eq. 6)	Figure 6b $\mu_2 = 0.05$ $f_2 = 6.5$	Figure 8b $\mu_2 = 0.01$ $f_2 = 5.9$		Figure 14b $\mu_2 = 0.05$ $f_2 = 47.4$	Figure 16b $\mu_2 = 0.05$ $f_2 = 35.6$
$\mathcal{R}_{TV}$ (eq. 12)	Figure 6c $\mu_{TV} = 0.04$ $f_{TV} = 9.8$	Figure 8c $\mu_{TV} = 0.01$ $f_{TV} = 5.9$	Figure 10b $\mu_{TV} = 0.04$ $f_{TV} = 1.76$	Figure 14c $\mu_{TV} = 0.03$ $f_{TV} = 67.9$	Figure 16c $\mu_{TV} = 0.04$ $f_{TV} = 45.3$
$\mathcal{R}_{DCT}$ (eq. 14)	Figure 6d $\mu_{DCT} = 0.01$ $f_{DCT} = 320.0$	Figure 8d $\mu_{DCT} = 0.02$ $f_{DCT} = 86.7$	Figure 10c $\mu_{DCT} = 0.01$ $f_{DCT} = 111.3$	Figure 14d $\mu_{DCT} = 0.06$ $f_{DCT} = 56.7$	Figure 16d $\mu_{DCT} = 0.01$ $f_{DCT} = 76.9$
$\mathcal{R}_{DWT}$ (eq. 14)	Figure 6e $\mu_{DWT} = 0.01$ $f_{DWT} = 145.0$	Figure 8e $\mu_{DWT} = 0.03$ $f_{DWT} = 7.9$	Figure 10d $\mu_{DWT} = 0.04$ $f_{DWT} = 27.1$	Figure 14e $\mu_{DWT} = 0.01$ $f_{DWT} = 67.1$	Figure 16e $\mu_{DWT} = 0.01$ $f_{DWT} = 89.1$
$\mathcal{R}_{DCT} + \mathcal{R}_M$ (eqs 14 and 16)	Figure 6g $\mu_{DCT} = 0.01$ $f_{DCT} = 247.0$ $\mu_{M_A} = 0.01$ $f_{M_A} = 1980.0$ $\mu_{M_B} = 0.01$ $f_{M_B} = 2450.0$ $\mu_{M_C} = 0.01$ $f_{M_C} = 878.0$	Figure 8g $\mu_{DCT} = 0.01$ $f_{DCT} = 34.6$ $\mu_{M_A} = 0.01$ $f_{M_A} = 145.2$ $\mu_{M_B} = 0.02$ $f_{M_B} = 816.3$	Figure 10h $\mu_{DCT} = 0.03$ $f_{DCT} = 125.6$ $\mu_{M_B} = 0.01$ $f_{M_B} = 516.7$	Figure 14h $\mu_{DCT} = 0.01$ $f_{DCT} = 40.0$ $\mu_{M_A} = 0.03$ $f_{M_A} = 234.1$ $\mu_{M_B} = 0.01$ $f_{M_B} = 567.8$	Figure 16g $\mu_{DCT} = 0.01$ $f_{DCT} = 64.7$ $\mu_{M_A} = 0.03$ $f_{M_A} = 789.4$ $\mu_{M_B} = 0.02$ $f_{M_B} = 548.2$
$\mathcal{R}_{DWT} + \mathcal{R}_M$ (eqs 14 and 16)	Figure 6h $\mu_{DWT} = 0.03$ $f_{DWT} = 147.0$ $\mu_{M_A} = 0.02$ $f_{M_A} = 1480.0$ $\mu_{M_B} = 0.01$ $f_{M_B} = 1750.0$ $\mu_{M_C} = 0.01$ $f_{M_C} = 1678.2$	Figure 8h $\mu_{DWT} = 0.01$ $f_{DWT} = 45.7$ $\mu_{M_A} = 0.03$ $f_{M_A} = 417.8$ $\mu_{M_B} = 0.01$ $f_{M_B} = 123.5$			Figure 16h $\mu_{DWT} = 0.05$ $f_{DWT} = 80.1$ $\mu_{M_A} = 0.02$ $f_{M_A} = 916.2$ $\mu_{M_B} = 0.03$ $f_{M_B} = 816.5$
$\mathcal{R}_M$ (eq. 16)			Figure 10e $\mu_{M_A} = 0.06$ $f_{M_A} = 23050$		
$\mathcal{R}_1^x + \mathcal{R}_M$ (eqs 10 and 16)			Figure 10g $\mu_1^x = 0.01$ $f_1^x = 23.6$ $\mu_{M_B} = 0.05$ $f_{M_B} = 348.9$	Figure 14f $\mu_1^x = 0.03$ $f_1^x = 473.6$ $\mu_M = 0.01$ $f_M = 12547.1$	

Table 1

---

## Capítulo 4

# Considerações Finais

---

Para usar GOMs para resolver problemas inversos com flexibilidade na incorporação de vínculos, o método escolhido deve ser robusto para mudanças na função de custo e ser relativamente computacionalmente eficiente. Comparamos os desempenhos dos GOMs mais usados na geofísica aplicada (SA, GA e PSO) para resolver o problema inverso da resistividade DC 1.5D usando dados sintéticos e de campo. Como conclusão geral, o PSO e o GA são muito robustos para mudanças na função de custo e mais computacionalmente eficientes em comparação com a SA. O uso de funcionais normalizados é de importância fundamental para promover a robustez. Além disso, a convergência exige não apenas a adequação de dados, mas também de cada termo do vínculo da função de custo. Critério esse de fundamental importância para estabilizar as soluções.

Um importante subproduto dos GOMs é o conjunto de quasi-soluções a partir dos quais a região de confiança em torno da melhor solução pode ser estimada, permitindo assim ao intérprete avaliar a eficácia das restrições usadas na estabilização das soluções.

Finalmente, enfatizamos que, usando um exemplo simples de inversão de resistividade DC como exemplo, estamos tentando finalmente dar um passo em frente na direção de fornecer aos profissionais na geofísica um ambiente de inversão que permita uma alta flexibilidade no teste de diferentes restrições nos parâmetros do modelo como uma forma de enfrentar casos geológicos complexos, de forma semelhante, ele utilizou a abordagem de interpretação de teste e erro com base em códigos de modelagem flexíveis.

A interpretação torna-se mais legível para geofísicos usando considerações geológicas tanto quanto possível. Além disso, é importante notar que todas as diferentes abordagens fornecem soluções aceitáveis que se ajustam aos dados. Portanto, pode-se pensar que os métodos atuais devem ser usados tanto como ferramentas para evitar a instabilidade matemática devido a incertezas de dados como maneiras específicas de gerenciar a não unicidade (devido a modelos equivalentes).

Ao resolver o problema de inversão de resistividade DC 2D, um algoritmo PSO (ou qualquer outro GOM) oferece alta flexibilidade para modificar a função de custo, permitindo que o intérprete mude facilmente os critérios de ajuste de dados ou as restrições empregadas. Igualmente importante, a malha de interpretação pode ser dividida em partições, onde diferentes restrições podem ser combinadas. Como resultado, o intérprete tem liberdade para executar um processo de interpretação quantitativa com base em uma abordagem de inversão de julgamento e erro, possivelmente combinada com fases de mo-

delagem de tentativa e erro. Além disso, a partir do critério de parada do algoritmo PSO resulta não apenas a melhor solução, mas também um conjunto de quase-soluções subótimas das quais as análises de incerteza podem ser realizadas.

Para obter essa flexibilidade, foi necessário que fizéssemos duas melhorias técnicas no algoritmo PSO. A primeira foi normalizar cada termo da função de custo para permitir a robustez do algoritmo às mudanças nos termos da função de custo. A segunda melhoria foi modificar o processo de inicialização inicial das partículas do enxame do PSO para melhor lidar com parâmetros que podem mudar facilmente em três ordens de grandeza.

A principal limitação da abordagem de inversão apresentada é o tempo computacional porque cada avaliação da função de custo requer uma modelagem avançada. Portanto, sua aplicação ainda está limitada a problemas inversos geofísicos onde a modelagem direta é computacionalmente barata. Por exemplo, a abordagem de inversão apresentada pode ser atualmente estendida a grav 2D / 3D e mag 2D de problemas eletromagnéticos inversos, mas não em problemas inversos sísmicos. Note, no entanto, que devido ao constante avanço do poder de computação, esse obstáculo tende a ser cada vez mais pequeno.

Para trabalhos futuros sugerimos:

- a) Utilização de algoritmos paralelizados;
- b) Utilização de algoritmos politopos;
- c) Utilização de outros vínculos de esparsidade de base curvelet ou base Ridgelet.

---

## Referências Bibliográficas

---

- Ajo-Franklin, J. B., Minsley, B. J. and Daley, T. M. (2007), 'Applying compactness constraints to differential travelttime tomography', *Geophysics* **72**(4), R67–R75.
- Barbosa, V. C. F., Silva, J. B. and Medeiros, W. E. (1997), 'Gravity inversion of basement relief using approximate equality constraints on depths', *Geophysics* **62**(6), 1745–1757.
- Constable, S. C., Parker, R. L. and Constable, C. G. (1987), 'Occam's inversion: A practical algorithm for generating smooth models from electromagnetic sounding data', *Geophysics* **52**, 289–300.
- Dey, A. and Morrison, H. (1979), 'Resistivity modelling for arbitrarily shaped two-dimensional structures', *Geophysical Prospecting* **27**(1), 106–136.
- Ghosh, D. (1971), 'Inverse filter coefficients for the computation of apparent resistivity standard curves for a horizontally stratified earth', *Geophysical Prospecting* **19**, 769–775.
- Ghosh, D. P. (1970), The application of linear filter theory to the direct interpretation of geoelectrical resistivity measurements, PhD thesis, Delft University of Technology(The Netherlands). 1970.
- Goldberg, D. E. (1989), 'Genetic algorithms in search, optimisation, and machine learning', *Seventh Impression, Pearson* .
- Guillen, A. and Menichetti, V. (1984), 'Gravity and magnetic inversion with minimization of a specific functional', *Geophysics* **49**(8), 1354–1360.
- Jafarpour, B., Goyal, V. K., McLaughlin, D. B. and Freeman, W. T. (2009), 'Transform-domain sparsity regularization for inverse problems in geosciences', *Geophysics* **74**(5), R69–R83.
- Koefoed, O. (1979), *Geosounding principle-1*, Elsevier Science Publications Amsterdam, The Netherlands.
- Last, B. and Kubik, K. (1983), 'Compact gravity inversion', *Geophysics* **48**(6), 713–721.
- Madden, T. R. (1971), 'The resolving power of geoelectric measurements for delineating resistive zones within the crust', *The Structure and Physical Properties of the Earth's Crust* pp. 95–105.

- Medeiros, W. E. (1987), The resistivity method applied to the hydrogeology of crystalline terrains: A problem of two-dimensional modelling, Master's thesis, Universidade Federal da Bahia, Brazil (in Portuguese).
- Mufti, I. R. (1976), 'Finite-difference resistivity modeling for arbitrarily shaped two-dimensional structures', *Geophysics* **41**(1), 62–78.
- Park, M.-W. and Kim, Y.-D. (1998), 'A systematic procedure for setting parameters in simulated annealing algorithms', *Computers & Operations Research* **25**(3), 207–217.
- Rudin, L. I., Osher, S. and Fatemi, E. (1992), 'Nonlinear total variation based noise removal algorithms', *Physica D: Nonlinear Phenomena* **60**(1), 259–268.
- Stefanescu, S. (1930), 'en collaboration avec c. et m. schlumberger, sur la distribution électrique potentielle autour d'une prise de terre ponctuelle dans un terrain a couches horizontales homogenes et isotropes', *Journal de Physique et le Radium, Serie VII, Tome I*.
- Suganthan, P. N. (1999), Particle swarm optimiser with neighbourhood operator, in 'Evolutionary Computation, 1999. CEC 99. Proceedings of the 1999 Congress on', Vol. 3, IEEE.
- Tikhonov, A. N. and Arsenin, V. Y. (1977), *Solutions of ill-posed problems*, Winston.
- Youzwishen, C. and Sacchi, M. (2006), 'Edge preserving imaging', *Journal of Seismic Exploration* **15**(1), 45.

---

# Apêndice A

## Modelagem em eletrorresistividade

---

Este apêndice apresenta o embasamento teórico deste trabalho referente à modelagem em eletrorresistividade.

### Modelagem em eletrorresistividade 1D

Métodos DC ou métodos de eletrorresistividade envolve injeção de corrente elétrica na terra por um sistema de eletrodo de corrente e medidas de potencial elétrico com eletrodo receptores. Na prática é tecnicamente mais conveniente o uso de baixa frequência (abaixo de 10 Hz), que propaga dentro da terra praticamente como corrente direta. Levantamentos DC são usados para determinar a resistividade de formações rochosas.

Resistividade é parâmetro físico muito importante que fornece informação sobre o conteúdo mineral e estrutura física das rochas e também sobre fluídos em rochas. Em levantamentos DC os eletrodos de corrente e de potencial são usados para mapear a distribuição espacial da formação de rocha. A principal limitação do método resistivo é que correntes diretas não podem penetrar através de formações resistivas.

Em levantamentos DC são fornecidos dados de resistividade aparente e uma estimativa dos seus erros.

O problema do cálculo da resistividade aparente para um modelo de terra estratificada plana paralela para o arranjo de eletrodos Schlumberger é dado por Stefanescu (1930).

$$V = \frac{\rho I}{2\pi} \left[ \frac{1}{r} + 2 \int_0^{\infty} \theta(\lambda, k, h) J_0(\lambda r) d\lambda \right], \quad (1)$$

$$\rho_{as} = \rho_1 \left[ 1 + 2r^2 \int_0^{\infty} \theta(\lambda, k, h) J_1(\lambda r) d\lambda \right], \quad (2)$$

onde  $I$  é a corrente injetada na terra,  $2r$  é o espaçamento do eletrodo de corrente AB,  $V$  é o eletrodo de potencial em  $r = \left(\frac{AB}{2}\right)$ ,  $\rho_{as}$  é a resistividade aparente Schlumberger,  $\rho_1$  é a resistividade da camada do topo,  $J_0$  e  $J_1$  são funções de Bessel de ordem zero e 1ª ordem, respectivamente,  $\theta(\lambda, k, h)$  é a função Kernel de Stefanescu,  $\lambda$  é a variável de integração,  $k$  é o coeficiente de reflexão de resistividade e  $h$  é a espessura da camada.

O kernel Slichter é definido Koefoed (1979) por

$$K(\lambda, k, h) = [1 + 2\theta(\lambda, k, h)] \quad (3)$$

A transformada de resistividade indicada por  $T(A, k, h)$  é definida (Koefoed, 1979) por

$$T(\lambda, k, h) = \rho_1 K(\lambda, k, h) \quad (4)$$

Tem a dimensão física da resistividade e é uma função dos parâmetros da camada e  $A$  que tem a dimensão do recíproco de comprimento. Está relacionado à resistividade aparente através da transformada de Hankel inversa da equação (2) como

$$T(\lambda, k, h) = \int_0^\infty \frac{\rho_{as}}{\lambda} J_1(\lambda r) dr \quad (5)$$

A relação de recorrência de Pekeris pode ser expressa pela função transformada de resistividade (Koefoed, 1979)

$$T_i = \frac{[T_{i+1} + \rho_i \tanh(\lambda h_i)]}{\left[1 + T_{i+1} \frac{\tanh(\lambda h_i)}{\rho_i}\right]} \quad (6)$$

O problema de resistividade direta usa o método do filtro linear introduzido por Ghosh (1971, 1970). O procedimento é realizado em duas etapas. O primeiro passo é calcular os valores de amostra da transformação de resistividade a partir dos parâmetros da camada. Isto é realizado pela aplicação da relação de recorrência de Pekeris [equação (6)]. Na segunda fase, os valores de amostra da resistividade aparente são determinados a partir daquela da transformação de resistividade pela aplicação de um filtro linear. A equação que define esta operação é dada como

$$\rho_{as}(x_0) = \sum_j f_j T(y_0 - j\Delta y) \quad (7)$$

onde  $x_0$  é a abscissa do ponto da função de saída (a resistividade aparente), e  $y_0$  é a abscissa do primeiro ponto da função de entrada (a transformada de resistividade) com o valor de abscissa  $\geq x_0$  e  $f_j$  são os coeficientes de filtro.

## Modelagem em eletrorresistividade 2D

Nesta sessão será apresentado o cálculo do potencial elétrico 2D pela formulação desenvolvida por Dey and Morrison (1979) utilizando diferenças finitas. Neste caso trabalha-se com a distribuição da propriedade física da resistividade elétrica (ou o inverso, a condutividade elétrica) num semi-plano. Para a discretização é necessário definir uma malha (grid), que é um conjunto finito de pontos no domínio definido (semi-plano). Esses pontos são chamados de nós.

O campo potencial 3-D devido a uma corrente de entrada conhecida está relacionado

à estrutura de condutividade, para condições de contorno apropriadas, conforme descrito na seguinte equação:

$$-\nabla(\sigma(x,y,z)\nabla\phi(x,y,z)) = I\delta(r-r_+)\delta(r-r_-) \quad (8)$$

onde  $\phi$  é o campo potencial,  $I$  é a corrente de entrada de um dipolo e  $s$  é a estrutura de condutividade do meio. Aqui,  $r_+$  e  $r_-$  são as localizações das fontes de corrente positiva e negativa, respectivamente, e  $\delta(r_- - r_+)$  é a função delta de Dirac, centrada na localização da fonte atual. Se assumirmos  $(\partial/\partial y)\sigma(x,y,z) = 0$ , a Eq. (8) pode ser reescrita como

$$-\nabla(\sigma(x,z)\nabla\phi(x,y,z)) = I\delta(r-r_+)\delta(r-r_-) \quad (9)$$

Dey and Morrison (1979) demonstraram que a Eq. (9) podem ser resolvidos eficientemente no domínio de Fourier. As transformadas inversa e direta de Fourier do cosseno são definidas, respectivamente, da seguinte forma:

$$\tilde{f}(x,y,z) = \int_0^\infty f(x,y,z) \cos(k_y y) dk_y \quad (10)$$

e

$$f(x,y,z) = \int_0^\infty \tilde{f}(x,y,z) \cos(k_y y) dk_y, \quad (11)$$

Onde  $k_y$  é o número de onda. Aplicando a transformada direta de Fourier do cosseno para a Eq. (9) obtemos uma solução para o potencial 2D transformado.

$$\nabla(\sigma(x,z)\nabla\tilde{\phi}(x,k_y,z)) - k_y^2\sigma(x,z)\tilde{\phi}(x,k_y,z) = -\frac{1}{2}\delta(r-r_+)\delta(r-r_-) \quad (12)$$

Onde  $\tilde{\phi}$  é o potencial de Fourier e  $k_y$  é o número de onda e  $\rho(x,z) = 1/\sigma(x,z)$ , onde  $\rho(x,z)$  e  $\sigma(x,z)$  são a resistividade e a condutividade respectivamente.

Para obter um campo de resistividade aparente ( $\rho_a$ ) do perfil de resistividade 2D dos eletrodos na superfície da Terra a partir de uma estrutura de resistividade conhecida. Usamos soluções de diferenças finitas da equação de Poisson para vários número de ondas  $k_y$  (12) (e.g Dey and Morrison, 1979, Madden, 1971, Mufti, 1976).

Depois de discretizar a Terra em um número finito de elementos ou um sistema de malha e manipular as condições de fronteira apropriadas, chegamos à seguinte equação do sistema linear Dey and Morrison (1979):

$$[K][\phi] = [s] \quad (13)$$

onde  $[\phi]$  é o vetor coluna de potencial desconhecido em cada nó,  $[K]$  é a matriz de capacitância e  $[s]$  é o vetor de origem. A matriz  $[K]$  é simétrica, esparsa, bandada e tridiagonal.

Na formulação matricial as equações de diferenças aplicadas a todos os nós  $(i,j)$ ,  $i = 1, 2, \dots, N$  e  $j = 1, 2, \dots, M$ , podem ser resolvidos simultaneamente com a solução do sistema linear (13). A matriz que carrega as informações da geometria da malha e da distribuição de condutividade é chamada de matriz resistência ou capacitância  $[K]$ . A matriz  $K$  é uma

matriz  $MN \times MN$  e é uma função da geometria e da distribuição da condutividade na malha  $(\sigma_{i,j})$ .

Usamos uma malha retangular irregular e uma condição de fronteira mista Dey and Morrison (1979). A equação do sistema (13) é resolvida pelo método de decomposição de Cholesky Dey and Morrison (1979). Usando esse algoritmo, podemos minimizar os requisitos de memória e reduzir o tempo de computação.

A modelagem DC 2D tem como objetivo obter as soluções numéricas para a equação (12) sujeita a condições de contorno apropriadas. As condições de contorno são:

1. O potencial  $\phi(x,y,z)$  deve ser contínuo através de cada fronteira da distribuição de condutividade  $\sigma(x,z)$  e

2. A componente normal  $\bar{J}(\equiv \frac{\partial\phi}{\eta})$  deve ser também contínua através de cada fronteira.

Tais condições de contorno são formuladas via diferenças finitas para os nós localizados na superfície e para as bordas esquerda, direita e inferior. As equações de diferenças para esses nós, com as condições fronteira mistas, com base no comportamento assintótico de potenciais podem ser encontradas em Dey and Morrison (1979).

A solução de  $\tilde{\phi}(x, k_y, z)$  é obtida derivando a equação (12), pela discretização adequada do espaço  $(x, k_y, z)$  sobre o qual o problema deve ser resolvido.

O código de modelagem DC 2D usado neste trabalho encontra-se em Medeiros (1987).

---

# Apêndice B

## Pseudo-códigos do SA, GA e PSO

---

### Pseudo code of the SA algorithm

```
Input:  
Geophysical:  $\mathbf{d}^{obs}$ ,  $\Omega$ ,  $\mu_p$ ,  $\mu_h$ ,  $p$ ,  $q$ ,  $r$ .  
Control parameters: size of epoch  $L$ , initial temperature  $T_0$ , cooling factor  $\alpha$ ,  
maximum number of iterations ( $n_i$ ), convergence threshold  $\delta$ .  
Output: best solution  $\mathbf{X}^*$   
1 Generate starting solution  $\mathbf{X}_i$   
2  $\mathbf{X}^* \leftarrow \mathbf{X}_i$   
3  $T \leftarrow T_0$   
4 while termination condition not reached do  
5     for  $l=1:L$  do  
6         Compute  $\mathbf{X}_u \in N(\mathbf{X}^*)$  (a neighborhood of the current solution) using  
           
$$\mathbf{X}_u = \mathbf{X}^* + \sqrt{T} \cdot \text{randn}(\text{size}(\mathbf{X}^*)) \cdot \frac{\mathbf{X}^*}{\|\mathbf{X}^*\|}$$
  
7         Compute  $\Delta = [F(\mathbf{X}_u) - F(\mathbf{X}^*)]$  and generate  $v$  (a uniform random variable)  
8         if  $(\Delta < 0)$  or  $\exp^{-\Delta/T} > v$  then  
9              $\mathbf{X}^* \leftarrow \mathbf{X}_u$   
10        end  
11    end  
12    Reduce  $T$   
13 end
```

**Algorithm 1:** Pseudo code of the SA algorithm, adapted from Park and Kim (1998)

## Pseudo code of the Genetic algorithm

```

Input:
Geophysical :  $\mathbf{d}^{obs}$ ,  $\mu_1$ ,  $\mu_2$ , search space, type of  $\ell_p$  norm.
Control parameters: population size ( $p_s$ ), crossover rate ( $p_c$ ), mutation rate ( $p_m$ )
number of iterations ( $n_i$ ), convergence threshold ( $\delta$ ).
Output: best solution  $\mathbf{X}$ 
1 Pop := a population of n randomly-generated individuals;
2 while Termination condition not reached do
3   for  $i=1: (n_i)$  do
4     number of crossover  $n_c = (p_s/2)$ 
5     for  $j = 1 : n_c$  do
6       randomly select two solutions  $\mathbf{X}_A$  e  $\mathbf{X}_B$  from Pop using roulette wheel;
7       gerate  $\mathbf{X}_C$  and  $\mathbf{X}_D$  by uniform crossover to  $\mathbf{X}_A$  and  $\mathbf{X}_B$  ;
8       save  $\mathbf{X}_C$  and  $\mathbf{X}_D$  to Pop1 ;
9     end
10    for  $j=1: n_c$  do
11      select a solution  $\mathbf{X}_j$  from Pop1 ;
12      mutate each bit of  $\mathbf{X}_j$  under the rate  $p_m$  and gerate a new solution  $\mathbf{X}'_j$ ;
13      update  $\mathbf{X}_j$  with  $\mathbf{X}'_j$  in Pop1 ;
14    end
15    update Pop = Pop1 ;
16  end
17  return the best solution  $\mathbf{X}$  in Pop
18 end

```

**Algorithm 2:** Pseudo code of the Genetic algorithm, adapted from Goldberg (1989)

## Pseudo code of the PSO algorithm

```

Input:
Geophysical :  $\mathbf{d}^{obs}$ ,  $\mu_1$ ,  $\mu_2$ , search space, type of  $\ell_p$  norm.
Control parameters: population size ( $p_s$ ), inertia factor ( $\omega$ ), cognitive attraction ( $c_1$ );
social attraction ( $c_2$ ), number of iterations ( $n_i$ ), convergence threshold ( $\delta$ ).
Output: : best solution  $\mathbf{X}$ 
1 Generate random population  $\mathbf{P}$  of particles with random values positions and velocities
2 Evaluate fitness  $F(\mathbf{X})$  for each particle in  $\mathbf{P}$ .
3 foreach particle  $\mathbf{X}_i$  in  $\mathbf{P}$  do
4 |  $F_{pbest}^i = F(\mathbf{X}_i)$  and  $\mathbf{X}_i^B = \mathbf{X}_i$ 
5 end
6  $\mathbf{X}^{BB} = \text{best}\mathbf{X}_i$  in  $\mathbf{P}$ 
7  $k=1$ 
8 while Termination condition not reached do
9 | foreach particle  $\mathbf{X}_i$  do
10 | | Update velocity using  $v_i^k = \omega.v_i^{k-1} + c_1.r_1(\mathbf{X}_i^B - \mathbf{X}_i^{k-1}) + c_2.r_2(\mathbf{X}^{BB} - \mathbf{X}_i^{k-1})$ ,
11 | | Update the position of the particle using  $\mathbf{X}_i^k = \mathbf{X}_i^{k-1} + v_i^k$ 
12 | | Evaluate fitness  $F(\mathbf{X}_i)$ 
13 | | if  $F(\mathbf{X}_i^k) < F_{pbest}^i$  then
14 | | |  $F_{pbest}^i = F(\mathbf{X}_i^k)$  and  $\mathbf{X}_i^B = \mathbf{X}_i^k$ 
15 | | end
16 | | if  $\min F(\mathbf{X}_i^k) < F_{gbest}$  then
17 | | |  $F_{gbest} = \min F(\mathbf{X}_i^k)$  and  $\mathbf{X}^{BB} = \mathbf{X}_g$  where  $F(\mathbf{X}_g) = F_{gbest}$ 
18 | | end
19 | |  $k=k+1$ 
20 | end
21 | return the best solution  $\mathbf{X} = \mathbf{X}^{BB}$ .
22 end

```

**Algorithm 3:** Pseudo code of the PSO algorithm, adapted from Suganthan (1999)

## Pseudo code of the PSO algorithm - case 2D

```

Input:
Geophysical :  $\mathbf{d}^{obs}$ , search space in the log,  $\mathcal{R}(\mathbf{m})$ .
Control parameters: population size ( $p_s$ ), inertia factor ( $\omega$ ), cognitive attraction ( $c_1$ );
social attraction ( $c_2$ ), number of iterations ( $n_i$ ), convergence threshold ( $\delta$ ).
Output: : best solution  $\mathbf{m}$ 
1 Using triangular distribution generate random population  $\mathbf{P}$  of particles with random
   values positions and velocities
2 Evaluate fitness  $\mathcal{L}(\mathbf{m})$  for each particle in  $\mathbf{P}$ .
3 foreach particle  $\mathbf{m}_n$  in  $\mathbf{P}$  do
4   |  $\mathcal{L}_{pbest}^n = \mathcal{L}(\mathbf{m}_n)$  and  $\mathbf{m}_n^B = \mathbf{m}_n$ 
5 end
6  $\mathbf{m}_{BB} = \text{best}\mathbf{m}_n$  in  $\mathbf{P}$ 
7  $\tau = 1$ 
8 while Termination condition not reached do
9   | foreach particle  $\mathbf{m}_n$  do
10    | Update velocity using  $v_n^\tau = \omega \cdot v_n^{\tau-1} + c_1 \cdot r_1 (\mathbf{m}_n^B - \mathbf{m}_n^{\tau-1}) + c_2 \cdot r_2 (\mathbf{m}_{BB} - \mathbf{m}_n^{\tau-1})$ 
11    | Update the position of the particle using  $\mathbf{m}_n^\tau = \mathbf{m}_n^{\tau-1} + v_n^\tau$ 
12    | Evaluate fitness  $\mathcal{L}(\mathbf{m}_n)$ 
13    | if  $\mathcal{L}(\mathbf{m}_n^\tau) < \mathcal{L}_{pbest}^n$  then
14    |   |  $\mathcal{L}_{pbest}^n = \mathcal{L}(\mathbf{m}_n^\tau)$  and  $\mathbf{m}_n^B = \mathbf{m}_n^\tau$ 
15    |   end
16    | if  $\min \mathcal{L}(\mathbf{m}_n^\tau) < \mathcal{L}_{gbest}$  then
17    |   |  $\mathcal{L}_{gbest} = \min \mathcal{L}(\mathbf{m}_n^\tau)$  and  $\mathbf{m}_{BB} = \mathbf{m}_g$  where  $\mathcal{L}(\mathbf{m}_g) = \mathcal{L}_{gbest}$ 
18    |   end
19    |  $\tau = \tau + 1$ 
20 end
21 return the best solution  $\mathbf{m} = \mathbf{m}^{BB}$ .
22 end

```

**Algorithm 4:** Pseudo code of the PSO algorithm, adapted from Suganthan (1999)